Evaluating the Shear Behaviour of FRP-Reinforced Concrete Beams Using the Shear Crack Propagation Theory

Morvarid Fattahi

Thesis submitted to the University of Ottawa
in partial Fulfilment of the requirements for the
Degree of Master of Applied Science

Department of Civil Engineering

Faculty of Engineering

University of Ottawa

Abstract

Most infrastructures in the world are made with reinforced concrete (RC), and one of the crucial concerns in North America is corrosion of steel reinforcement in RC structures. Corrosion can lead to severe degradation which can affect the serviceability and ultimate limit state, and cause failure. One solution for overcoming this phenomenon is the use of corrosion-resistant fibre-reinforced polymer (FRP) reinforcement. In addition to corrosion resistance, FRPs also present other advantages such as high strength and light weight compared to steel reinforcing bars. Their mechanical properties differ from those of steel; therefore, the flexural and shear behaviour of FRP-RC members requires investigation.

In general, predictions from flexural design equations are close to results from experimental data. However, shear strength predictions based on different modelling approaches can vary greatly. Thus, in the last century, one of the main controversies in the field of structural engineering attracting continuous attention is the shear behaviour of RC members. In previous studies, factors such as concrete strength, reinforcement ratio, beam depth, beam width, size effect, aggregate size, fracture energy and shear slenderness have been investigated in an effort to solve the riddle of shear in beams. Recently, a new rational theory named “Shear Crack Propagation Theory” (SCPT) was introduced that combines crack kinematics with constitutive material behaviour to predict shear behaviour over the entire loading process, rather than only focusing on the point of failure.

To date, the SCPT has only been used to predict the shear behaviour of RC beams containing steel reinforcement. The present study is the first to apply the SCPT to RC beams with non-metallic reinforcement. The numerical analysis using SCPT on RC members was validated against published test data and examines the role of important parameters such as reinforcement modulus of elasticity, reinforcement ratio, bond condition, and dowel resistance.

Acknowledgements

First and foremost, I wish to express my profound gratitude to my esteemed supervisor, Dr. Martin Noël. His guidance, support, and patience during my research project at the University of Ottawa were crucial to my success in completing my master's studies. Dr. Noël consistently stood by me during the most challenging phases of this research project, offering not only expert assistance but also uplifting encouragement. I have had the privilege of learning from him, not only in academic matters but also on a personal level, which has enriched my overall experience.

Additionally, I extend my heartfelt appreciation to the members of the thesis defense committee, Professor Beatriz Martin-Perez from the University of Ottawa, and Professor Christian Viau from Carleton University. Their valuable advice and constructive comments on this research have significantly contributed to its overall quality and depth.

I must also acknowledge Maximilian Schmidt and the dedicated team at RWTH University who contributed to the development of the methodology employed in this study. Their unwavering commitment to this theoretical framework has played an indispensable role in charting a viable path toward realizing the core subject matter of my thesis.

My gratitude further extends to my fellow classmates, whose assistance and collaborative spirit enriched my academic journey. I offer special thanks to Amin Iranpour and Ehsan Nazari from the University of Ottawa, as well as Sepideh Mirshekar from Carleton University, for their invaluable support and contributions to this project. I would also like to express my appreciation to my friend, Parisa Azari, for her crucial role in initiating this endeavor.

Finally, I wish to convey my profound appreciation to my cherished friends and family. Their compassionate support throughout my academic pursuits has been immeasurable. I extend my deepest appreciation to my husband, Ali, my greatest source of joy. His love, patience, and support have carried me through the ups and downs of the past few years, providing me with a perspective on life's most important priorities.

I dedicate this work to my parents, Mohammad and Nasrin, my sister, Negin, my husband, Ali, and individuals to whom I turned countless times for guidance and assistance during my academic journey. Without them, it would not have been possible to achieve what I have and to become the person I am today.

Table of Contents

List of Figures

List of Tables

Notation

a length of the shear span

a_g specified nominal maximum size of coarse aggregate

A_v area of the transverse shear reinforcement within a distance s

A_s area of longitudinal reinforcement on the flexural tension side of the member

A_c cross sectional area of concrete

b_w beam width

b_{tens} beam width in tensile

b_n concrete net width activated in tension

$b_{v,eff}$ effective shear width

b_v shear width

b width

d effective depth

d_v effective shear depth of the member (which is assumed to be the depth from compression face to the center of longitudinal tension reinforcement)

d_{ag} maximum aggregate size of the concrete and should not be larger than 32 mm

E_f FRP modulus of elasticity

E_s reinforcement modulus of elasticity

E_c Young's Modulus of concrete

f_c' concrete cylinder compressive strength

f_{ct} concrete tensile strength

f_{ck} characteristic concrete compressive strength

f_y yield strength of reinforcement steel

G_f concrete fracture energy

$h_{f,tens}$ flanges depth in tensile

h_f flange height

h height

k_{ag} coefficient for influence of aggregate size

k_λ shear slenderness factor

k size effect factor of EC2

k_d size effect factor according to elastic-plastic fracture mechanics

K_T shape factor

M moment

M_f factored moment at interior support resisted by elements above and below the slab

N_f factored axial load normal to the cross-section occurring simultaneously with V_f, including effects of tension due to creep and shrinkage (taken as positive for tension and negative for compression)

n_s number of reinforcement

n total number of transverse bars crossing the critical diagonal crack

s_z crack spacing parameter dependent on crack control characteristics of longitudinal reinforcement

s_{ze} equivalent value of s_z that allows for influence of aggregate size

V_p component in the direction of the applied shear of the effective prestressing force factored by ϕ_p

V_s contribution of shear reinforcement

V_C contribution of concrete

V_f factored horizontal shear in a storey

$V_{da,0}$ shear contribution of dowel action

V shear force

V_{si} shear force in the ith transverse bar

x_0 depth of the compression zone

α ratio value of the upper to lower crack branch

α_{cw} parameter in EC2

α_e ratio of the Young's moduli of reinforcement and prestressing steel

δ_k is the vertical shear deformation at the level of flexural reinforcement

ε_x longitudinal strain at mid-depth of the member due to factored loads (positive when tensile)

ε_s average reinforcement strain

θ strut angle

θ angle of inclination of the concrete principle diagonal compressive stress

λ shear slenderness

ξ relative compression zone depth

σ_{cp} concrete stress from prestressing

v_c dimensionless shear capacity of beams without shear reinforcement

v_w dimensionless values of shear transfer actions across web cracks

v_l dimensionless values of shear transfer actions for longitudinal reinforcement

v_s dimensionless values of shear transfer actions for transverse reinforcement

ρ geometric reinforcement ratio

ρ_w geometric shear reinforcement ratio

ϕ_c resistance factor for concrete

ϕ_s maximum aggregate size diameter

ψ coefficient accounting for aggregate fracture

Chapter 1

Introduction

1.1 General

In Canada, the widespread use of de-icing salts on concrete infrastructure creates an aggressive environment for steel reinforcement that leads to deterioration caused by corrosion. In general, corrosion can occur when carbon dioxide (CO_2) or chloride penetrate the concrete through its pores and/or surface cracks and reach the level of the steel reinforcement (Bentur et al., 1997) which can influence the serviceability and ultimate strength of a structure by reducing the steel cross section and bond performance. The corrosion process consists of two stages: first, in the initiation stage, chlorides from various sources such as de-icing salts concentrate on the steel surface and destroy the steel protective layer in a process known as depassivation; second, corrosion damage propagates as the effective area of the steel is reduced through oxidation and rust products accumulate at the interface of steel-concrete as depicted in Figure 1-1 (Darmawan, 2010). This process reduces both the reinforcement cross-sectional area and compromises the bond with the surrounding concrete (Berto et al., 2008).

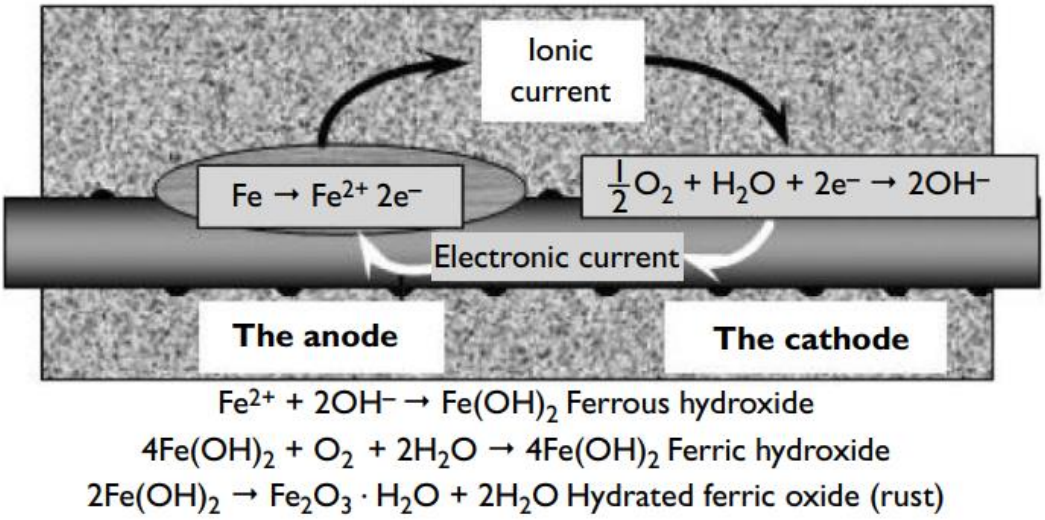

Figure 1-1 The steel corrosion process (Broomfield, 2007)

Many reinforced concrete (RC) infrastructures such as bridges need to be replaced or repaired due to the effects of corrosion. Although rehabilitation imposes a heavy cost for the government and taxpayers, this is not always an effective solution. A previous research study found that 20% of rehabilitated infrastructures failed after only 5 years and only 10% remained safe for more than 25 years, while the longest reported service life after rehabilitation was 52 years (Tilly, 2007).

The application of alternative reinforcement that resists corrosion such as fibre-reinforced polymers (FRPs) can mitigate this issue while also presenting advantageous properties that include high strength and light weight (Berto et al., 2008). FRPs are suitable for not only RC structures, but also for prestressed ones, and can increase the service life compared to steel-reinforced structures (NSERC, 2010).

However, FRP materials also present some disadvantages such as their low modulus of elasticity which leads to a decrease in dowel action and aggregate interlock, increases crack width, and finally reduces shear capacity (Dhahir, 2017). The shear behaviour of FRP-RC members is the main concern of this research which will be investigated in this thesis.

Various approaches have been adopted to predict and analyse the shear behaviour of FRP-RC members, including the Modified Compression Field Theory (MCFT) which is the basis of Canadian design standards (CSA A23.3:19) (Bernard, 2013; Roshan, 2017; Vecchio & Collins, 1986). However, recently, an innovative mechanical theory, known as the “Shear Crack Propagation Theory” (SCPT), was developed that combines concepts of crack kinematics with constitutive material models to predict shear crack behaviour at all stages of loading until failure occurs in RC members (Classen, 2020). In the past, engineers mainly relied on empirical approaches to estimate the ultimate shear strength of RC members, which has resulted in unsafe designs and structural failures. This has led to increased research efforts to understand the "mechanical behaviour" of shear transfer actions in diagonally cracked members. Based on the SCPT model, seven primary factors can explain the shear behaviour of members in the absence of shear reinforcement: the crack location in the fracture process zone (FPZ), crack propagation by loading increase, cantilever action, the transfer of shear within the section of concrete that has not experienced cracking (compression zone), dowel action, aggregate interlock, and crack bridging action (Schmidt et al., 2021). Unlike other methods, the SCPT is not limited only to evaluating the failure strength but can also predict the progress of crack growth at all stages of loading. Although the SCPT was originally developed and evaluated for steel-RC members, there is no fundamental limitation that precludes its application to concrete members with non-metallic reinforcement. This research will analyze the behaviour of FRP-RC members in shear using SCPT for the first time.

1.2 Objectives and Scope of Research

Although many efforts have been made to obtain the ultimate shear strength of RC beams with FRP reinforcement based on previous empirical and mechanical approaches, there are few, if any, research studies which have analyzed the shear crack behaviour for the entire loading stage up to

failure. In the past, due to the complexity of shear behaviour and its dependence on multiple parameters, simple empirical models have been formulated using experimental test results that were generally based on laboratory-produced beams with different scales, loading, and boundary conditions than real structural members. To account for the high degree of uncertainty associated with shear behaviour, large safety factors were traditionally required for design. However, new mechanically based models have managed to overcome this challenge by combining crack kinematics with constitutive behaviour models to develop a deeper understanding of the role of different shear transfer mechanisms at all stages of the loading process. The SCPT method is a rational approach that brings together recent advances in understanding of shear behaviour as a unified theory that enables a detailed evaluation of the importance of key parameters and cause of failure in shear-critical members.

In this research, the SCPT method will be extended to beams reinforced with FRP bars, which are increasingly used as a corrosion-resistant alternative to steel reinforcement to design longer lasting structures. The use of FRP reinforcement is known to significantly influence shear behaviour of RC beams because of their lower elastic moduli, dowel capacity, and different bond characteristics compared to steel bars (Noël, 2013).

By introducing appropriate material constitutive models and bond characteristics, the SCPT approach will be used to account for these changes and predict the shear crack propagation for FRP-RC structures. This will enable researchers and engineers to improve the accuracy and safety of new designs and evaluation of existing structures.

By analyzing the propagation and the behaviour of shear cracks, civil engineers can improve the condition of infrastructures, save more financial resources for individuals and governments, and enhance sustainability by increasing service life or reducing maintenance time.

The specific objectives of this thesis are summarized as follows:

1- Compiling a comprehensive literature review and historical overview of shear behaviour models.
2- Expanding the SCPT to account for the different properties of FRP bar reinforcement.
3- Validating the SCPT method with experimental data for FRP-RC beams.

1.3 Thesis Organization

This thesis contains 5 chapters, including:

- Chapter 2 presents a literature review of different shear strength models for RC beams without shear reinforcement (in particular the SCPT) as well as the use of FRP reinforcement for RC structures.
- Chapter 3 modifies the SCPT approach for FRP-RC beams by investigating the role of longitudinal reinforcement stiffness as well as modifying the dowel action effect and accounting for tension stiffening.
- Chapter 4 focuses on a validation of the SCPT with experimental data reported in the literature on the shear performance of FRP-RC beams.
- Chapter 5 summarizes the main results from the analytical investigations and provides some suggestions for future studies.

Chapter 2

Literature Review

2.1 Introduction

In Canada, there are a significant number of infrastructures such as bridges which are exposed to harsh weather and experience deterioration, thus needing to be replaced or repaired. To facilitate traffic conditions in snowy weather, de-icing salts are considered as one of the solutions to improve road safety. However, a serious consequence of this practice occurs in the form of steel reinforcement corrosion following the penetration of chloride-laden water into the concrete substrate through a network of pores and small cracks. From a mechanical point of view, serviceability and ultimate strength are two important limit states affected by corrosion which can also lead to the eventual failure of reinforced concrete (RC) structures. To mitigate this condition and increase the bridge's service life, fibre-reinforced polymer (FRP) materials are considered as a corrosion-resistant option to conventional steel reinforcement for concrete structures (Noël, 2013).

In recent years, new mechanics-based theories have been developed for the prediction of the shear behaviour of RC members from first cracking until failure. One such theory, known as the Shear Crack Propagation Theory (SCPT), has shown significant promise in terms of its accuracy and

ability to rationally predict the contribution of all key mechanisms affecting shear behaviour (Classen 2020, Schmidt et al. 2021). To date, this theory has only been applied to conventional steel-RC beams. In this thesis, the SCPT is extended to FRP-RC beams for the first time.

2.2 Shear Failure Modes

One challenging issue which has attracted continuous attention in the last century is the shear behaviour of RC members (Yoo, 2022). Predicting shear behaviour for RC is complex due to the coinciding complicated effects of several parameters such as the shape of a member, strength of concrete, strength and details of stirrups, and the tensile and shear reinforcement ratio (Wu & Hu, 2017). The prediction of failure regions and their ultimate strength is also complicated because the shear failure of RC beams occurs through several damage mechanisms that include diagonal cracks, crushing of concrete struts, bond failure between main reinforcement and concrete, and failure and yielding of shear reinforcement (Rombach et al., 2011).

Whereas a sectional analysis, such as the one illustrated in Figure 2-1, can provide an intuitive and accurate result for pure flexure, which occurs between the two-point loads, there is no region experiencing pure shear and the critical crack corresponding to the final failure path generally has a complex geometry.

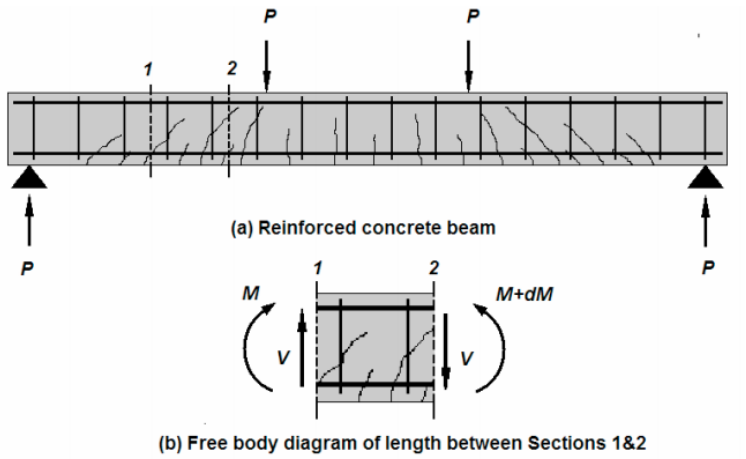

Figure 2-1 A simply supported reinforced concrete beam (Esfandiari, 1997)

Another issue that can further complicate the analysis is the non-uniformity of transverse reinforcement strain over the beam depth (Esfandiari, 1997).

Although the exact definition for various kinds of shear failure can be complicated, some of them will be addressed in this section. The possible shear failure modes are defined as follows (Fig. 2-2) (Herbrand, 2017):

a) Web shear failure: when a rupture failure occurs in the web due to the principal tensile stress exceeding the tensile strength of the concrete.
b) Flexural shear failure: these are shear cracks which start from a flexural crack and create a distinct horizontal crack branch.
c) Diagonal tension failure: similar to the flexural shear failure, except that the initial major flexural crack occurs adjacent to the support and leads to shear failure.
d) Shear-tension failure: when splitting cracks form along the longitudinal reinforcement due to the loss of bond or inappropriate concrete cover.
e) Shear-compression failure: it occurs in the compression zone for shorter beams with more longitudinal reinforcement which is a brittle failure.
f) Arch rib failure: it occurs when the residual tensile capacity of concrete is reduced by heavy utilization of the compressive strength and leads to a brittle rupture.
g) Stirrup rupture: can occur in beams with transverse reinforcement.
h) Concrete crushing: occurs before yielding of transverse reinforcement when there is a high number of stirrups.

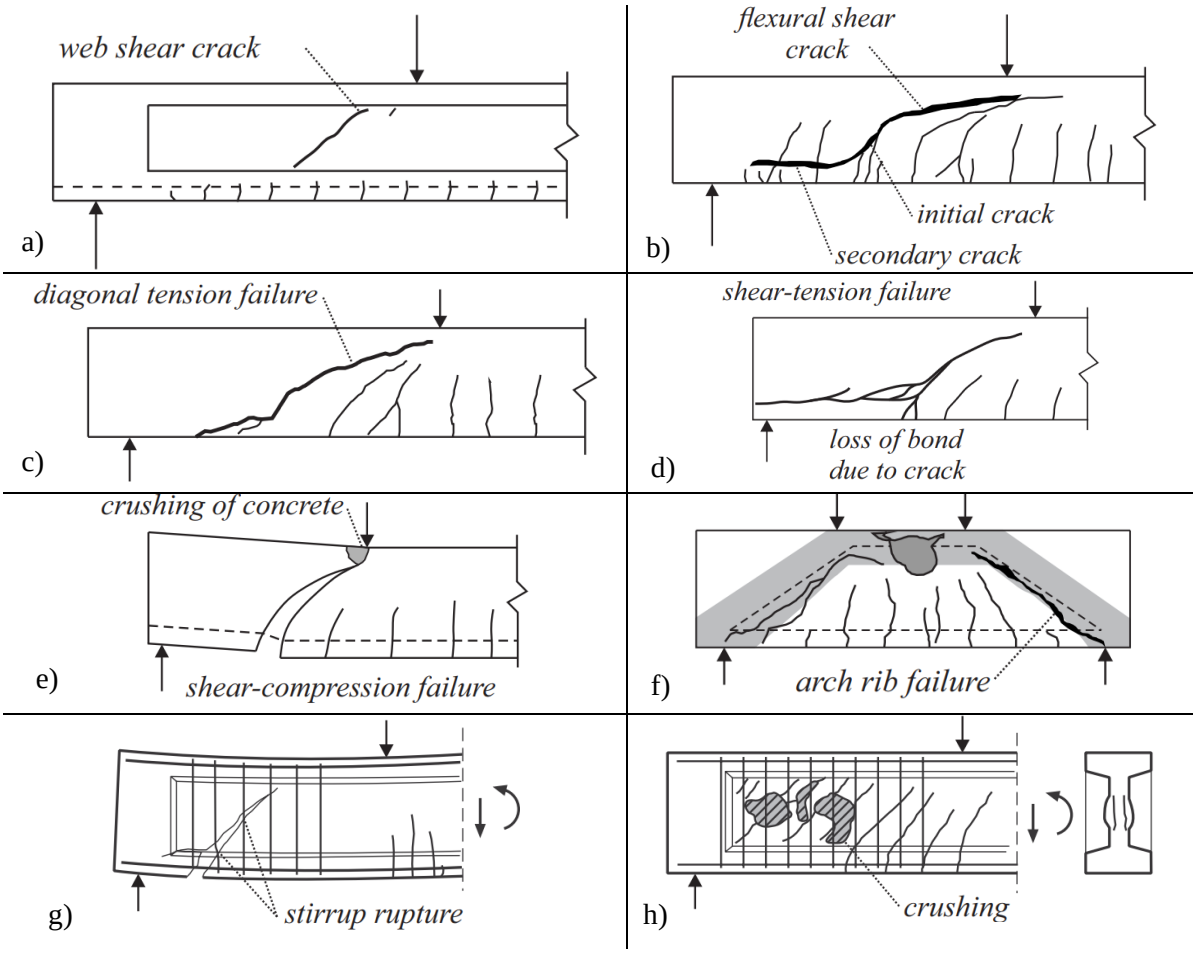

Figure 2-2 Various types of shear failure (Herbrand, 2017)

2.3 Influencing Parameters

In this section, some of the parameters which have an impact on shear strength will be discussed, including concrete properties, compression zone, size effect, shear slenderness, loading conditions, and cross-section geometry (Herbrand, 2017). Parameters which apply specifically to FRP-RC beams will be addressed in Section 2.5.

2.3.1. Influence of concrete properties

One of the main parameters which has a significant impact on shear strength is the aggregate size (Bentz et al., 2006; Muttoni & Ruiz, 2008). Both the width of flexural crack and the crack slip as a function of crack friction and aggregate interlock are important for shear strength and are

influenced by the aggregate size and type, although the grading curve is more significant than the maximum aggregate size. Thus, concentrating solely on the maximum aggregate size while neglecting the consideration of the aggregate type and grading falls short of encompassing all the essential factors that influence shear capacity (Walraven & Reinhardt, 1981).

Another important concrete property which is related to shear strength is concrete tensile strength. In higher strength concrete, aggregates are the weakest constituent and shear cracks can appear through them. Thus, the effect of aggregate interlock will be reduced. In Equation 2-2, ψ is a reduction factor that is related to concrete strength. Following Herband's research, shear strength models should incorporate aggregate size, aggregate type, grading curves, and aggregate fracture by adding a new factor (k_{ag}) to other factors (k_λ and k_d are shear slenderness and size effect factors, respectively) to the concrete shear strength (Eq. 2-1) (Herbrand, 2017).

$$V_c = \frac{2}{3} k_{ag} k_\lambda k_d \xi b_w d\, f_{ct} \qquad \text{Eq. 2- 1}$$

$$k_{ag} = 1 + 0.45\psi \sqrt{\frac{d_{ag}}{32}} \qquad \text{Eq. 2- 2}$$

$$\psi = 1 \; for \; f_{ck} \leq 60 \qquad \text{Eq. 2- 3}$$

$$\psi = 1 - \sqrt{\frac{f_{ck} - 60}{30}} \; for \; 60 < f_{ck} < 80 \qquad \text{Eq. 2- 4}$$

$$\psi = 0.18 \; for \; f_{ck} \geq 80 \qquad \text{Eq. 2- 5}$$

Where ξ is the relative compression zone depth, b_w is the beam width, d is the effective depth, f_{ct} is the concrete tensile strength, f_{ck} is the characteristic concrete compressive strength, and d_{ag} is the maximum aggregate size.

2.3.2. Influence of the Compression Zone

For RC beams, failure modes are often categorized as flexural failure or shear failure; the first is typically associated with yielding or tensile rupture of the reinforcing bars, while the latter is associated with several different mechanisms including aggregate interlock, dowel action, or shear transfer across the compression zone that has not experienced cracking (Herbrand, 2017). Shear compression failure occurs when the crack tip extends into the flexural compression zone (Placas et al., 1971). Based on Rombach and Kohl's research, the compression zone height, which is influenced by the ratio of longitudinal reinforcement, is the dominating mechanism in a shear failure (Rombach & Kohl, 2016a). In accordance with Frosch's methodology, the ratio of longitudinal reinforcement is a significant parameter influencing the expansion of the compression zone. Elevating the proportion of longitudinal reinforcement directly results in increasing the compression depth which has the potential to enhance shear strength (Tureyen & Frosch, 2002).

2.3.3. Size Effect

Based on fracture mechanics, size effect is an important phenomenon affecting shear capacity of RC beams. Before the 1980s, empirical shear design equations were based only on the results of relatively small-scale laboratory specimens (Herbrand, 2017). However, in 1984, Bazant focused on large specimens and claimed that the energy released from these specimens for propagating the cracks can have effect on the failure. In brittle failure of concrete structures, the size effect can be analyzed by considering this assumption that the potential energy release is influenced by both the length of the crack and the area of the crack zone. Size effect refers to the phenomenon that the structural behaviour of beams subjected to shear forces, including failure mode and stiffness, changes as the size of the beam increases (Bazant & Chen, 1997).

As the depth of the beam increases, the spacing and length of the diagonal shear crack also increases. Larger beams also often have a higher probability of containing material variability (such as voids or weaker areas within the concrete), which can affect their shear strength. By increasing the crack spacing in larger beams, the width of the cracks also increases which directly affects the aggregate interlock shear transfer mechanism. With wider cracks, the aggregates are unable to interlock effectively, thereby diminishing their ability to contribute to shear strength. Thus, the shear strength varies among beams of different dimensions when accounting for the size effect (Bazant & Kazemi, 1991).

The impact of size effect is also considered in CSA standards by applying the parameters β and s_{xe} in shear resistance formula for beams without shear reinforcement (CSA A23.3:19, 2019):

$$V_c = \phi_c \lambda \beta \sqrt{f_c'} b_w d_v, which \begin{cases} \beta > 0.05 \\ \sqrt{f_c'} < 8MPa \end{cases} \quad \text{Eq. 2- 6}$$

$$\beta = \frac{0.40}{(1 + 1500\varepsilon_x)} . \frac{1300}{(1000 + s_{xe})} \quad \text{Eq. 2- 7}$$

Where s_{xe} varies based on beam depth, vertical longitudinal reinforcement layers' spacing, and maximum aggregate size.

2.3.4. Influence of Shear Slenderness

Shear slenderness is the shear span to beam depth ratio (a/d) for point-loaded single-span beams. It is obvious that the shear span (a) increase leads to the increase in the maximum moment, and larger crack widths lead to a reduction in the effect of aggregate interlock and appearance of the tensile stress at the tip of crack. By increasing the shear span parameter (a), some other cracks will appear between the critical shear crack and the supports. In fact, the shear should be tolerated by several parameters such as crack friction, dowel action at the longitudinal reinforcement, and tensile forces at the tip of crack, of which the first parameter can be decreased because of larger

crack widths (Herbrand, 2017). On the other hand, Collins et al. showed that longitudinal reinforcement ratio and shear slenderness have a strong interaction with each other (Collins et al., 2008). Besides, it is indicated that the shear slenderness is associated with the $M/(V \cdot d)$ ratio for continuous beams, and failure will occur near the load in which the shear forces and moments are larger (larger $M/(V \cdot d)$) (Herbrand, 2017).

2.3.5. Influence of Loading Conditions

One of the other important parameters for shear strength is loading conditions for single span or continuous beams under concentrated or uniformly distributed loads (UDL). Under UDL, failure of a single span occurs near the supports where there are larger shear forces and smaller flexural moments (smaller $M/(V \cdot d)$), with the critical control section occurring at a location d away from the support (Herbrand, 2017). Under concentrated loads, the probability of failure is greater in proximity to the loading point, where the M/V ratio is higher.

2.3.6. Influence of Cross-Section Geometry

The cross-section effect refers to the influence of the shape and dimensions of a structural element's cross-sectional geometry on its mechanical behaviour and performance. CSA A.23.3-19 code (CSA A23.3:19, 2019) assumes that in ‘I’ and ‘T’ sections, the entire shear force is supported by the web, and it assigns the contribution of the compression flange to the web (Sagaseta & Vollum, 2011). Segaseta et al. investigated how different shapes and sizes of beam cross-sections influence their ability to resist shear forces. Beam cross-sections can vary widely, ranging from rectangular to T-shaped. Their study evaluated how the geometry of these cross-sections interacts with shear forces and how different shapes might affect shear strength. The findings indicate that, the shear strength for ‘I’ and ‘T’ sections receives an increment of up to 20% due to the involvement of the

compression flange. However, it is noteworthy that in accordance with code assumptions, the entirety of shear force is attributed to the web component (Sagaseta & Vollum, 2011).

2.4 Modeling Approaches

2.4.1. Empirical Models

Empirical models encompass theories that derive from experimental analysis or direct observation. Although differentiating between empirical and mechanical models is sometimes challenging, some of the empirical models reported in literature will be presented in this section. Despite some drawbacks of this approach, it has had an impact on some of the formulas used in various codes.

In previous years, there was a belief that the shear strength of concrete beams solely relied on the strength of concrete. However, in 1907 and 1908, Talbot conducted a significant experimental study with 106 beam tests without any shear reinforcement. Their findings challenged the previous notion and demonstrated that the nominal shearing stress was influenced by several other parameters. These included the longitudinal reinforcement ratio, the relative beam length, and other parameters that affected the beam stiffness (Fig. 2-3) (Talbot, 1909).

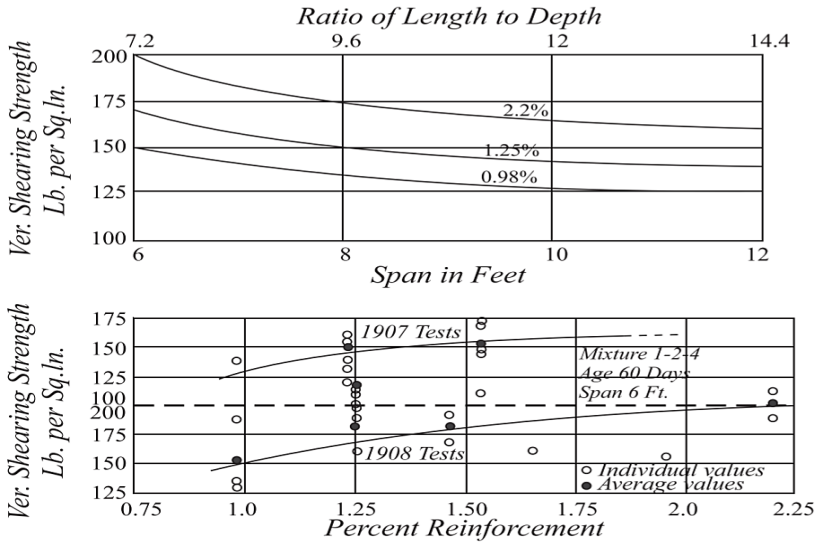

Figure 2-3 The effect of slenderness and amount of longitudinal reinforcement versus shearing strength (Talbot, 1909)

Moreover, Talbot's research indicated that the quality and strength of the concrete played a crucial role in establishing the shear strength. As a result, it became evident that relying solely on the concrete's strength to estimate shear resistance was not sufficient (Talbot, 1909).

In 1945, Moretto examined the longitudinal reinforcement ratio effect on 44 beams and presented an equation to demonstrate this effect on shear strength (Eq. 2-8) (Moretto, 1945).

$$V_c = (0.088f_c' + 30.4\rho)b_w d \qquad \text{Eq. 2- 8}$$

Then, in 1951, Clark investigated the longitudinal reinforcement ratio effect, concrete compressive strength, and the ratio of shear span to depth. Although a formula was derived from the tests (Eq. 2-9), it was asserted that it may not be applicable to all beams beyond the tested range (Clark, 1951).

$$V_c = (48.3\rho + 0.12f_c'\frac{d}{a})b_w d \qquad \text{Eq. 2- 9}$$

Considering the ratio of a/d posed a limitation due to its dependence on single-span beams subjected to point-loads. Moody et al. addressed this issue through a series of tests and proposed a new ratio called the M/V ratio, where M and V represent the maximum moment and shear force, respectively (Moody et al., 1954). Furthermore, other researchers asserted that shear strength is linked to the square root of concrete strength, rather than concrete strength itself (Morrow & Viest, 1957). These investigations formed the basis for ACI 318-19 Building Code design provisions (Eq. 2-10) (ACI318-19, 2019).

$$V_c = (0.158\sqrt{f_c'} + 17.2\rho\frac{Vd}{M})b_w d \leq 0.29\sqrt{f_c'}b_w d \qquad \text{Eq. 2- 10}$$

Another important factor investigated in the following years was size effect. Zsutty and other researchers claimed that the shear strength depends on concrete compressive strength to the power

of 1/3, longitudinal reinforcement ratio, the ratio of a/d (shear slenderness), size effect (cross section depth and geometry), and loading conditions (Herbrand, 2017; Zsutty, 1968).

This has formed the basis of the Model Code 1990 provisions (Eq. 2-11).

$$V_c = 0.15(3d/a_v)^{1/3}\xi(100\rho f_c')^{1/3}b_w d \qquad \text{Eq. 2- 11}$$

Where:

$$\xi = 1 + \sqrt{200/d}$$

In summary, experimental analysis reveals that the shear strength of RC beams that are not reinforced in shear is influenced by multiple parameters: concrete strength (f_c), longitudinal reinforcement ratio (ρ), effective depth (d), shear span to effective depth ratio (a/d), and loading conditions. It was found that shear strength tends to increase with higher concrete compressive strength, especially when considering both slender and short RC beams. Additionally, the shear strength is enhanced by greater longitudinal reinforcement ratios (Nouri et al., 2021).

For a/d ratios greater than 2.5, an increase in this ratio yields a reduction in shear strength, while the opposite holds true for a/d values less than 2.5. Furthermore, an increase in the effective depth results in a shear strength decrease (Nouri et al., 2021).

The shear strength exhibits variability based on the loading conditions, which could involve point loads or distributed loads (Nouri et al., 2021).

However, there are additional mechanisms at play that contribute to shear strength and are not easily or fully assessable through experimental analysis. Furthermore, researchers hold differing opinions, largely due to variations in their experimental conditions. Thus, mechanical models can be helpful to complement the empirical approach that can increase understanding and be applied to a wider range of applications.

2.4.2. Mechanical Models

In contrast to empirical analyses, which are exclusively rooted in experimental data, various mechanical models have been investigated with the aim of comprehending the underlying physical behaviour and mechanics of the materials and components involved. This section will examine several of these mechanical models.

2.4.2.1 Tooth or comb models

Although in the 1950s and 1960s, some factors such as longitudinal reinforcement, concrete strength, and shear slenderness were investigated to compute the RC members capacity without shear reinforcement, shear failures were not well-understood (Herbrand, 2017). Kani was one of the pioneers aiming to answer the biggest question about shear failure and published a paper named "The riddle of shear failure and its solution" in 1964 that reviewed flexural failure, shear failure, diagonal failure, and the influence of bond on flexural failure (Kani, 1964).

Kani noted that when the longitudinal steel yields, the width and length of a flexural crack will increase which leads to the compression zone decrease. The flexural crack pattern has the appearance of a comb (Fig. 2-4), in which the compression zone forms the backbone, and the tensile zone can be considered the teeth of the comb. By increasing the bending in the structure, the stress in the compression zone increases which leads to destruction in this zone and consequently the flexural failure of the beam (Kani, 1964).

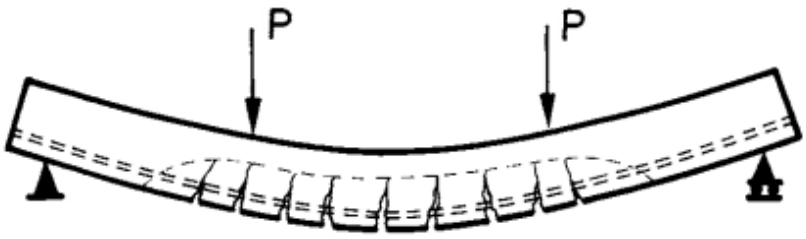

Figure 2-4 Comb-like structure for beams in bending (Kani, 1964)

Kani also examined a series of beams with cracks located outside the central section of the beam. Since the maximum bending moment takes place at the midspan, the reason of those failures cannot be the maximum bending moment. Thus, shear stress can be considered as the reason for those failures, and the definition of "shear failure" was chosen (Kani, 1964). He proposed a model with tooth-elements and shear forces associated with friction in cracks (V_f), dowel forces (V_d), and a shear force component in the compression chord (V_c). This has formed the basis of several mechanical models, such as that shown in Figure 2-5 (Reineck, 1991).

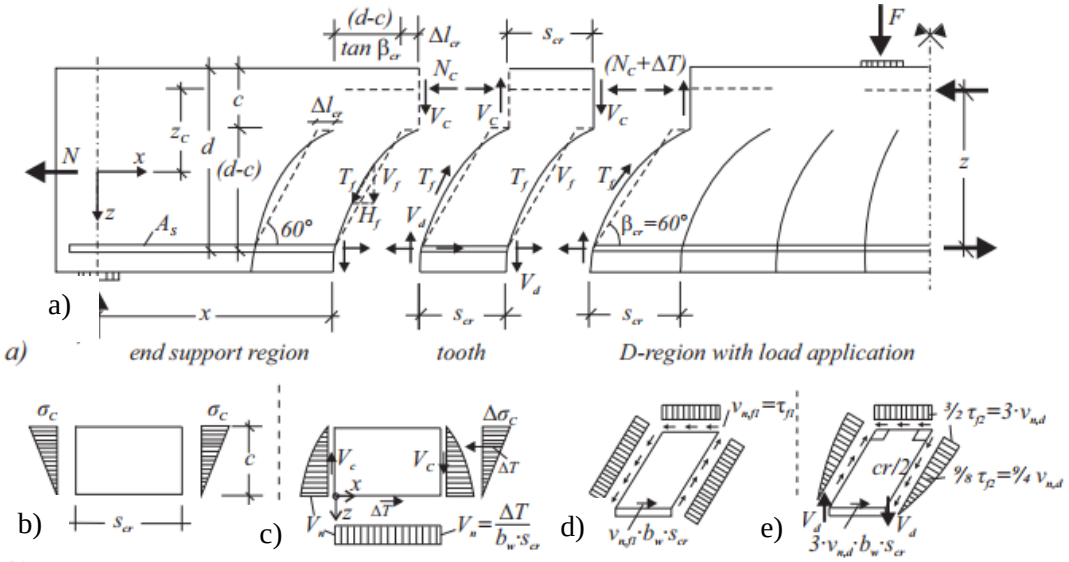

Figure 2-5 a) Tooth-element model and the forces in B region, b) constant σ_c, c) equilibrium for $\Delta\sigma_c$,, d) constant friction, e) friction connected dowel effect shear forces (Reineck, 1991)

In diagonal failure, there is an assumption that the central section should be stronger than the end sections under pure bending. By illustrating the free body diagram, the hypothetical diagonal line will be created which can be the basis of the "diagonal failure" definition (Fig. 2-6) (Kani, 1964).

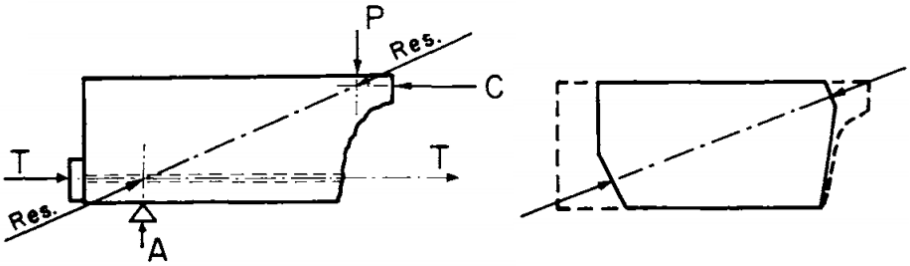

Figure 2-6 Free-body diagram of a reinforced concrete (Kani, 1964)

The influence of the reinforcement and concrete bond was observed in the spacing of the cracks. Closely spaced cracks can be seen when there is a strong bond. However, few or no cracks can be seen in poorly bonded or unbonded structures. The consequence of the tests which Kani examined was interesting. He showed that the structure with poor bond has a higher capacity than those with good bond due to the arching action that develops (Kani, 1964).

In Kani's model, every concrete tooth is considered as a cantilever arm loaded by ΔT which is the tensile force of the reinforcing bars (Fig. 2-7). According to this approach, the Euler–Bernoulli beam theory is not applicable, and plane cross sections will not remain plane since every tooth will be bent under horizontal ΔT forces which leads to a curved axis line. Thus, the existence of ΔT can create a distinction between RC beams with and without bond (Kani, 1964).

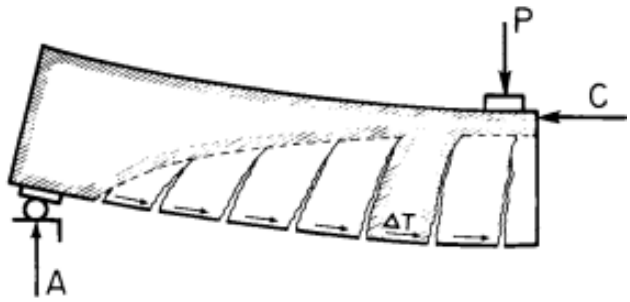

Figure 2-7 The function of concrete teeth under tensile force of ΔT (Kani, 1964)

Then, in 2016, Tue et al. developed a model for beams cracked in bending. They found that the distribution of forces and the pattern of flexural cracking significantly influence the shear behaviour. Their model was restricted to slender members, in which $a/d \geq 2.5$. They considered a single-span beam that was simply supported at both ends and was subjected to two concentrated loads which first leads to perpendicular (flexural) cracks and then cracks deviated from the perpendicular direction with increasing shear forces. The flexural cracks were not as deep as the tension zone depth. In a cracked section, the only parameter that changes, with increasing bending moment, is the stress within the flexural reinforcement.

Based on their results, it was shown that shear resistance is mainly due to the interlocking action of the aggregate within the tension zone. The opening of additional wider cracks near the flexural reinforcement is compensated by dowel action. The surface crack growth is dependent on several parameters such as the strain and the ratio of the flexural reinforcement. They also indicated that the shear failure will occur adjacent to the section that has not experienced cracking and in a shear band which the tips of the flexural cracks tend to connect (the location where the bending moment is smallest in the cracked region and when the shear resistance is surpassed along a certain length S_{rm}) (Fig. 2-8) (Tung & Tue, 2016).

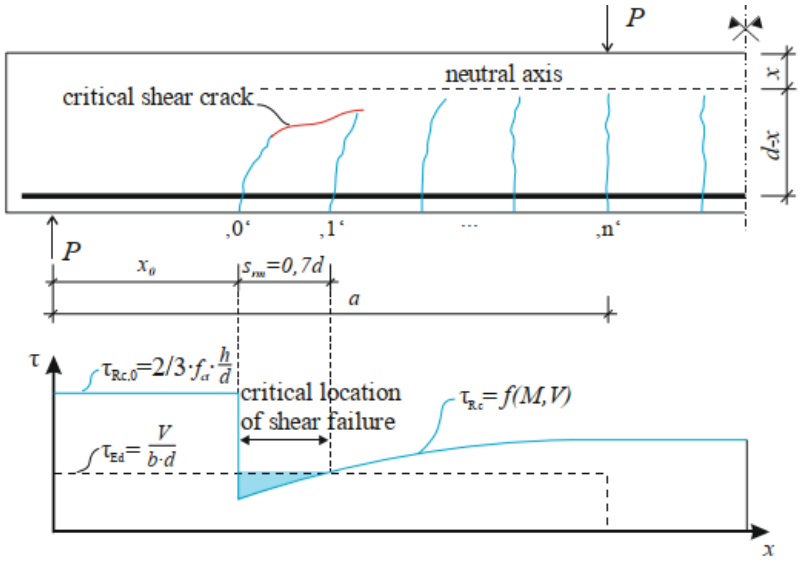

Figure 2-8 Analysis of the location of critical shear crack (Tung & Tue, 2016)

2.4.2.2 Compression chord models

In 1963, Bresler et al. observed three modes of failure including diagonal tension (D-T) failures, shear-compression (V-C) failures, and flexural-compression (F-C) failures (Kotsovos, 1983). They found that diagonal failure occurs closer to the support for beams without stirrups, while for beams with stirrups, it occurs in proximity to the applied load (Fig. 2-9) (Bresler & Scordelis, 1963). Given that the shear forces remain uniform across the entire span, they raised the possibility that diagonal failure is attributed not solely to shear forces but also to bending action. This bending

action arises from longitudinal compressive forces and holds greater influence in the occurrence of diagonal failure (Kotsovos, 1983).

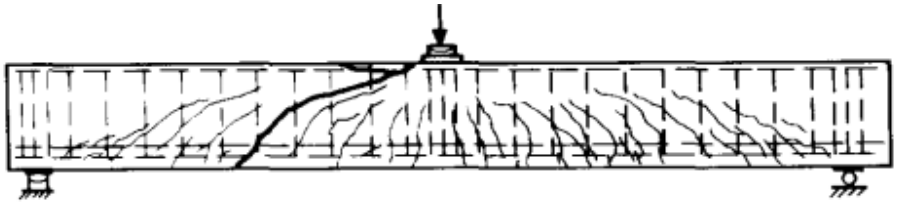

(a) Beam with stirrups

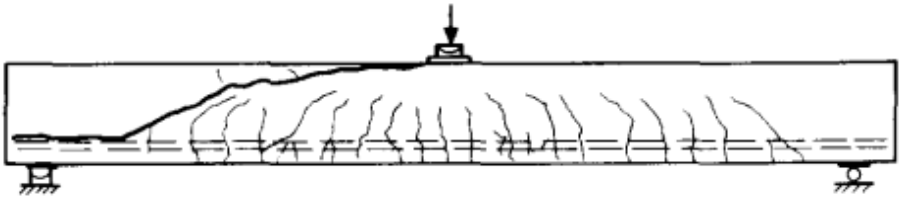

(b) Beam without stirrups

Figure 2-9 The effect of stirrups on the diagonal failure of the beams (Kotsovos, 1983)

The compressive force path in a RC member can lead to diagonal shear failure; based on the equilibrium conditions shown in Figure 2-10, a tensile force should be present near the tip of crack when the compressive force is shifted towards the support (Kotsovos, 1983).

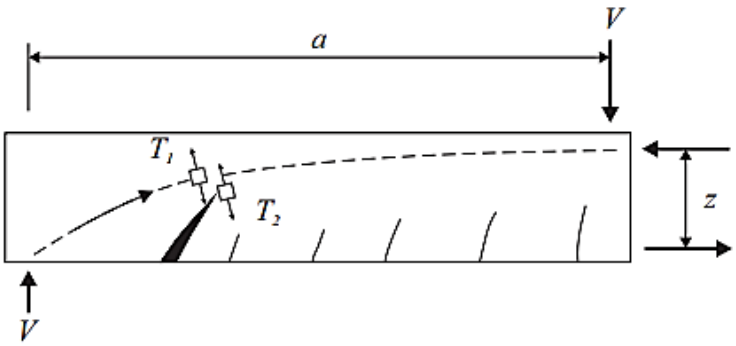

Figure 2-10 Path of compression force due to a loading point toward a support (Kotsovos, 1983)

Based on Zararis & Papadakis's investigations, two different branches can be created as inclined shear cracks. The first one which is propagated at the flexural cracks tip and near the support will be created just after the beginning of the first flexural cracking. However, the second branch is the crucial one and the reason of the failure. It starts from the first branch tip and connects to the

loading point which means it passes through the compression zone (Fig. 2-11). This mode of failure can only occur in slender beams, in which a/d>2.5, and they noted that slenderness and size effect factors can have an influence on shear strength (Eq. 2-12).

$$V_u = (1.2 - 0.2\frac{a}{d}d)\frac{x_0}{d} f_{ct} b_w d \quad \text{Where} \quad 1.2 - 0.2\frac{a}{d}d \geq 0.65, a \text{ in } m \qquad \text{Eq. 2- 12}$$

One of the primary findings derived from their experiments was that, apart from the beam depth, the size effect is also influenced by the ratio of shear span to depth (Zararis & Papadakis, 2001).

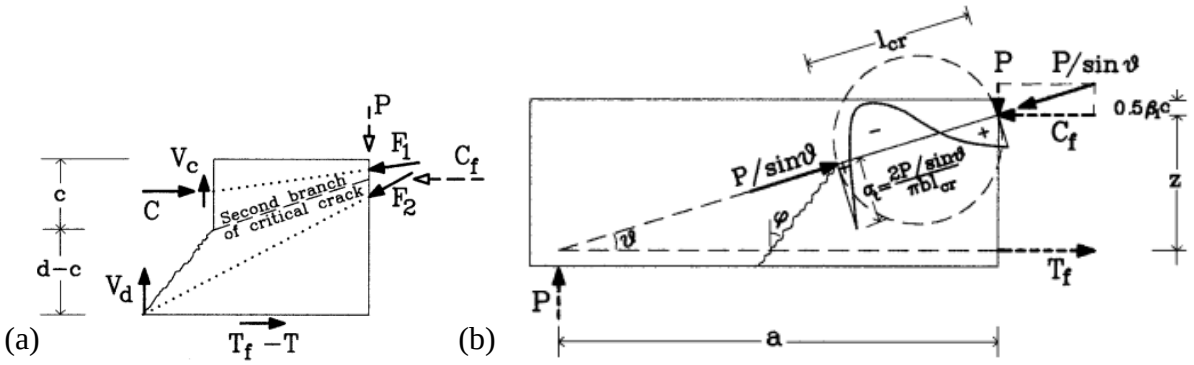

Figure 2-11 a) Proposed arrangement of the second branch of critical crack, b) Normal stress distribution along second branch line (Zararis & Papadakis, 2001)

In 2015, Cladera et al. illustrated that shear strength is derived from several parameters such as compression zone (v_c which is dependent on size effect term (ξ), and effective shear width $b_{v,eff}$), stirrup (v_s), and longitudinal reinforcement (v_l) (Eq. 2-13 to 2-20) (Cladera et al., 2015).

$$V_u = (v_c + v_w + v_l + v_s) f_{ct} b_w d \leq \frac{\alpha_{cw} b_w d . v_l f_c'}{\cot\theta + \tan\theta} \qquad \text{Eq. 2- 13}$$

$$v_c = \xi \left[\left(0.70 + 0.18 K_T + \left(0.2 + 0.5\frac{b}{b_w} \right) v_s \right) \frac{x_0}{d} + 0.02 K_T \right] \frac{b_{v,eff}}{b} \qquad \text{Eq. 2- 14}$$

$$\xi = 1.2 - 0.2\text{a} \geq 0.65; \text{ a in m} \qquad \text{Eq. 2- 15}$$

$$\text{K}_\text{T} = 0.1 + 0.9\frac{\text{b}_\text{w}}{\text{b}} + 2.5\frac{\text{h}_\text{f,tens}}{\text{h}}\left(\frac{\text{b}_\text{tens} - \text{b}_\text{w}}{\text{b}}\right) \qquad \text{Eq. 2- 16}$$

$$v_w = 167\frac{f_{ct}}{E_c}\left(1 + \frac{2E_c G_f}{f_{ct}^2 d}\right)\frac{b_w}{b}$$ Eq. 2- 17

$$v_l = 0.23\frac{\alpha_e \rho_l}{1 - {x_0}/{d}} \text{ if } v_s > 0;\ v_l = 0 \text{ if } v_s = 0$$ Eq. 2- 18

$$v_s = 0.85 K_\theta \rho_w \frac{f_{yw}}{f_{ct}}$$ Eq. 2- 19

$$K_\theta = \frac{(d - h_f) + (h_f - x_0)\frac{b_v}{b_w}}{d - x_0}$$ Eq. 2- 20

2.4.2.3 Fracture mechanics models

Fracture mechanics models have been considered for shear failure prediction because flexural or diagonal shear cracking in concrete and RC members without stirrups are assumed as a brittle mode of failure (Herbrand, 2017). Based on solid mechanics, one of the important challenges is the scaling problem which was addressed by Bazant (Bazant & Chen, 1997). He investigated three primary categories of size effects: 1- statistical size effect, arising from strength randomness, 2- energy release size effect, and 3- possible size effect attributed to fracture mechanics or microcracks. He illustrated that the nature of concrete is quasi-brittle and based on this assumption, developed a formula to describe a structural size effect law which is dependent on maximum aggregate size, a factor that is a relative structure size, and an empirical constant (Eq. 2-21) (Bazant & Kim, 1984).

$$\sigma_N = f_t' \phi(\lambda) and\ \phi(\lambda) = \frac{1}{\sqrt{1 + {\lambda}/{\lambda_0}}}\ where\ \lambda = {d}/{d_{ag}}, and\ \lambda_0 = constant$$ Eq. 2- 21

Xu & Reinhardt illustrated that the rotation occurring at the diagonal shear crack tip induces an extra moment equivalent to the fracture energy and lead to an extension of the longitudinal

reinforcement length that is unbonded (Fig. 2-12). This unbonded failure can be affected by mode II fracture which is caused by high bond stress between the interface of concrete and steel. They claimed that more investigations should be done on mode II fracture to predict the diagonal shear type of failure which is dependent on K_{IIc} (fracture toughness) and G_{IIF} (fracture energy) parameters (Xu & Reinhardt, 2005). Accordingly, one of the important parameters which most researchers considered in their models for fracture mechanics is the size effect.

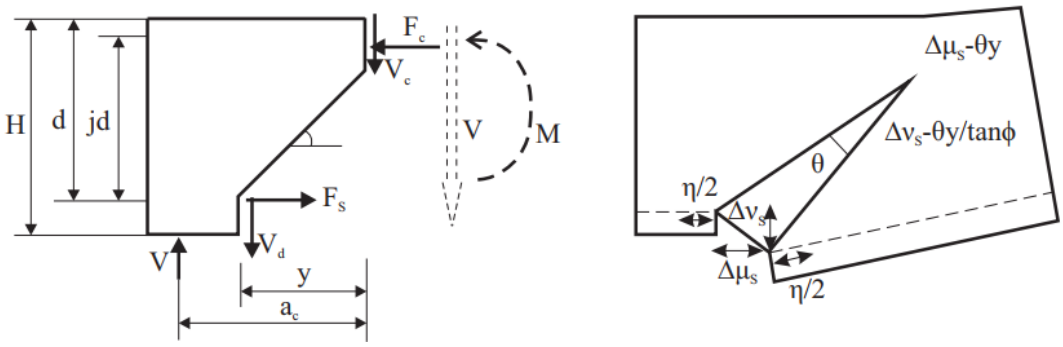

Figure 2-12 The free-body illustration and steel bar deformation details (Xu & Reinhardt, 2005)

2.4.2.4 Plasticity theory models

Reineck was one of the first researchers who presented the plasticity theory based on strut-and-tie models for reinforced concrete without shear reinforcement (Fig 2-13). One of the important conclusions from his mechanical models was the importance of the effect of the reinforcement ratio (ρ) and size effect (which is dependent on the depth) on the shear capacity (Reineck, 1991).

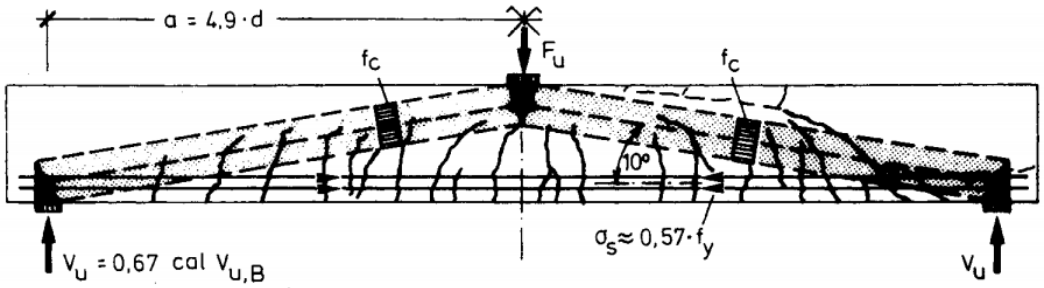

Figure 2-13 The model developed on the basis of the theory of plasticity by Bresler & Scordelis (represented by Reineck) (Bresler & Scordelis, 1963)

In 1978, Nielsen et al. proposed a model with one single strut located between the support and the loading point based on plasticity theory and assumed that a tensile stringer force is anchored behind the support. Based on their theory, the shear strength depends on various factors, including compressive strength, shear span ratio, the longitudinal reinforcement strength, and concrete quality (Eq. 2-22 & 2- 23) (Nielsen et al., 1978).

$$v_c = \frac{1}{2} b_w h v f_c' \left(\sqrt{\left(\frac{a}{h}\right)^2 + \frac{4\rho_l {f_y}/{f_c'} (v - \rho_l {f_y}/{f_c'})}{v^2}} - \frac{a}{h} \right) for\ \rho_l {f_y}/{f_c'} \leq \frac{1}{2} v \quad \text{Eq. 2- 22}$$

$$v_c = \frac{1}{2} b_w h v f_c' \left(\sqrt{\left(\frac{a}{h}\right)^2 + 1} - \frac{a}{h} \right) for\ \rho_l {f_y}/{f_c'} \geq \frac{1}{2} v \quad \text{Eq. 2- 23}$$

Some of the researchers concluded that an effective factor that is dependent on several factors such as concrete compressive strength, reinforcement ratio, size effect, and shear slenderness need to show the residual concrete compressive strength derived from crossing the flexural shear cracks with the strut (Eq. 2-24 to 2-28) (Herbrand, 2017). They also showed that the strut-and-tie approach can only applied to the members in D-regions (for a/d≤1).

$$v = f_1 f_2 f_3 f_4 \quad \text{Eq. 2- 24}$$

$$f_1 = \frac{3.5}{\sqrt{f_c'}}\ and\ 5 < f_c' < 60\ MPa \quad \text{Eq. 2- 25}$$

$$f_2 = 0.27\left(1 + \frac{1}{\sqrt{h}}\right) and\ 0.08 < h < 0.7m \quad \text{Eq. 2- 26}$$

$$f_3 = 15\rho_l + 0.58\ and\ \rho_l < 0.045 \quad \text{Eq. 2- 27}$$

$$f_4 = 1.0 + 0.17(\frac{a}{h} - 2.6)^2\ and\ {a}/{h} < 5.5 \quad \text{Eq. 2- 28}$$

Recent research has focused on the yield line theory within three distinct cutoff sections, as depicted in Figure 2-14, instead of a single straight yield line. Three different parameters such as sliding of unreinforced concrete in the compression zone and shear crack, and concrete layer splitting along the longitudinal reinforcement which are derived from the vertical deflection (δ_u) lead to activate shear components. It is also shown that for slender beams, shear failures derive from already existing cracks, develop due to the bending effect, and form because of both bending and shear impacts. Besides, dowel action, aggregate interlock, critical crack width, and concrete layer bending are additional parameters that should be noticed in this model (Fisker & Hagsten, 2016; Herbrand, 2017).

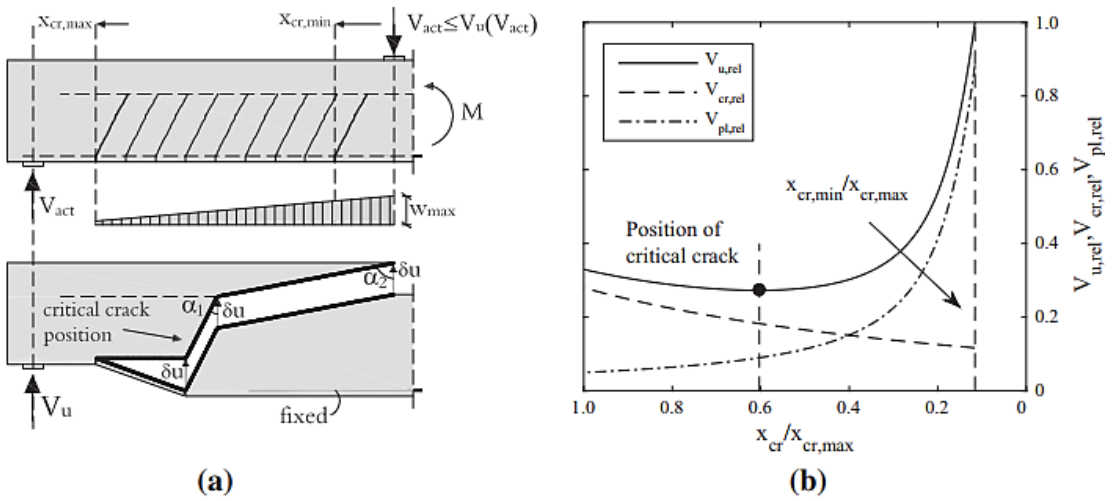

Figure 2-14 a) Crack position (between $X_{cr,max}$, and $X_{cr,min}$), b) variation of shear capacity for each possible crack position (Fisker & Hagsten, 2016)

2.4.3. Modified Compression Field Theory (MCFT)

In the 1970's, Collins and Mitchell developed the Compression Field Theory (CFT) to estimate the post-cracking behaviour of RC members in torsion and shear (Mitchell & Collins, 1974). However, the CFT had some deficiencies that were addressed by their new theory named Modified Compression Field Theory (MCFT) in 1986. In CFT, compression softening effects, tension

stiffening effects, and examination of stress conditions at crack surface were not considered, while MCFT addressed all of them (Bentz et al., 2006; Vecchio & De Lorenzi, 2009).

To develop the MCFT, several RC elements were examined under pure shear stresses as well as various combinations of shear and axial loads using a novel "Panel Element Tester" (Fig. 2-15). Several main hypotheses were considered for this method:

1- The longitudinal and transverse reinforcement loads (stresses), and cracks are uniformly distributed in the element.
2- The edge of the element should remain straight and parallel in deformation (Fig. 2-16).
3- The effect of loading history is not considered and based on this logic, for every strain only one corresponding stress should be assumed.
4- For the large areas which several cracks may be included, the average values of stresses and strains should be calculated.
5- The bond exists between the reinforcing bars and concrete is assumed to be perfect, and no slip should be considered at the boundaries of the element (Vecchio & Collins, 1986).

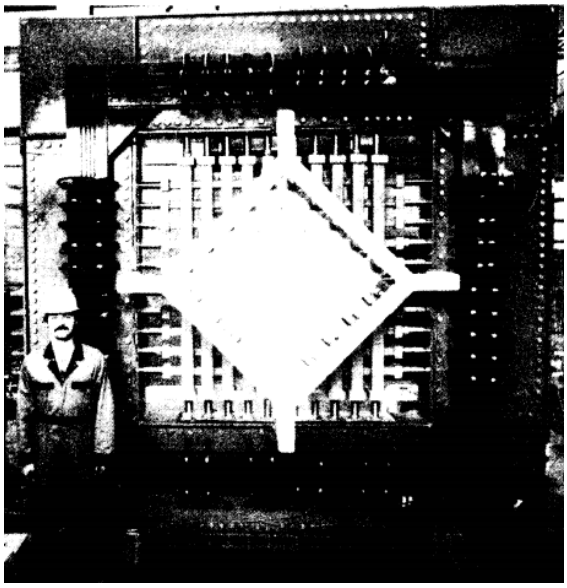

Figure 2-15 Panel Element Tester (Vecchio & Collins, 1986)

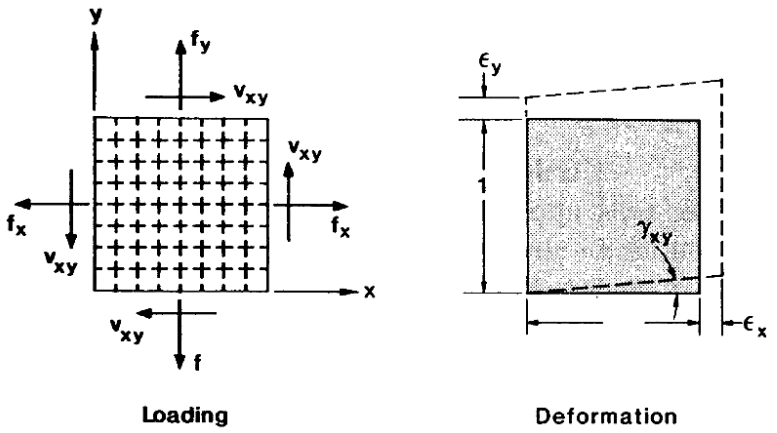

Figure 2-16 The formation of the element after deformation (Vecchio & Collins, 1986)

In general, there are three main components which are considered in MCFT:

1- Compatibility conditions: It looks at deformation of different parts of the element, and they should be compatible with each other.

2- Equilibrium conditions: It looks at stress and forces conditions at the crack location, and they did not consider dowel action in their equilibrium.

3- Constitutive conditions: It looks at strain and stress conditions.

3-1- Compression softening effect: It is indicated that there is a strength and stiffness reduction for the cracked concrete in compression in comparison with a uniaxially compressed concrete (Fig. 2-17).

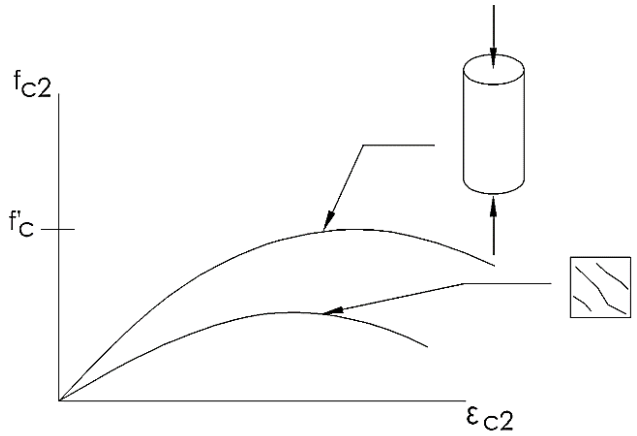

Figure 2-17 Compression softening effect (Vecchio & De Lorenzi, 2009).

3-2- Tension stiffening effect: By looking at the element before and after cracking, it can be indicated that the tensile stresses should be considered even in a cracked element. At the location of crack, this value will be zero, but there are still tensile stresses between the cracks by transferring them through the reinforcement. Thus, for the whole element, it should be considered average tensile stresses due the bond effects with the reinforcement (Fig. 2-18 & 2-19).

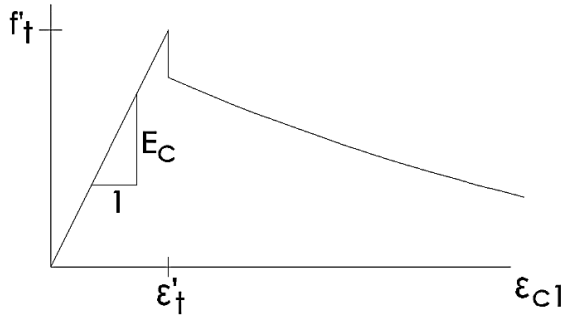

Figure 2-18 Strain and tensile stresses relationship before and after the crack (Vecchio & De Lorenzi, 2009)

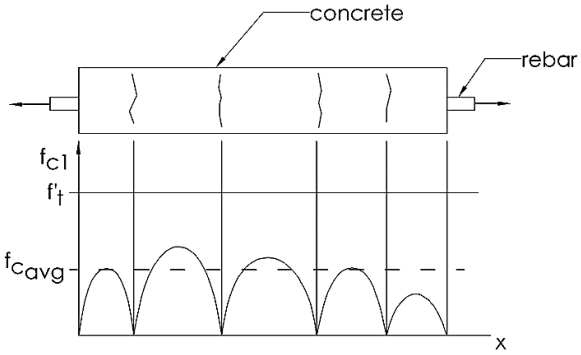

Figure 2-19 Average tensile stresses due to the bond effects (Vecchio & De Lorenzi, 2009)

In MCFT, the tension stiffening effect can be applied by Equation s 2-29 & 2-30:

$$f_{c1} = \frac{f_t'}{1+\sqrt{200\varepsilon_{c1}}} \qquad \varepsilon_{c1} > \varepsilon_t' \quad \text{(For small elements)} \qquad \text{Eq. 2- 29}$$

$$f_{c1} = \frac{f_t'}{1+\sqrt{500\varepsilon_{c1}}} \qquad \text{(For larger elements)} \qquad \text{Eq. 2- 30}$$

Which f_{c1} should be limited by the capacity of the reinforcement:

$$f_{c1} \leq \rho_x(f_{yx} - f_{sx}) \cdot sin^2\,\theta_c + \rho_y(f_{yy} - f_{sy}) \cdot cos^2\,\theta_c \qquad \text{Eq. 2- 31}$$

3-3- It is examined the stress condition at the crack location (local conditions), not the average stress and strain in the element ($\overline{G_c} \neq 0$).

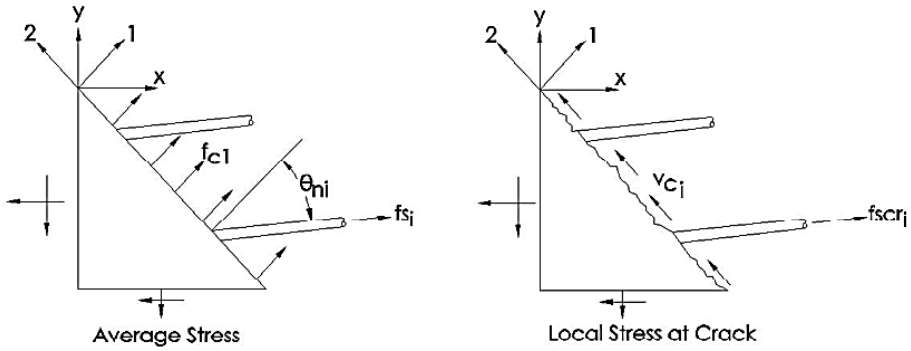

Figure 2-20 Average tensile stresses due to the bond effects (Vecchio & De Lorenzi, 2009)

As it can be seen in Figure 2-20, there is a normal stress f_{c1} between the cracks, but at the crack location, the shear stress v_{ci} is acting and has a limit which is based on the capacity of aggregates to resist the shear stress along the crack. This shear stresses on the crack (v_{ci}) can be calculated based on Equations 2-32 to 2-39:

$$\varepsilon_{1cr} = \varepsilon_1 + \Delta\varepsilon_{1cr} \qquad \text{Eq. 2- 32}$$

$$\varepsilon_{scri} = \varepsilon_{si} + \Delta\varepsilon_{1cr} \cdot cos^2\theta_{ni} \qquad \text{Eq. 2- 33}$$

$$f_{scri} = E_s \cdot \varepsilon_{scri} \leq f_{yi} \qquad \text{Eq. 2- 34}$$

$$f_{c1} = \sum_{i=1}^{n} \rho_i (f_{scri} - f_{si}) \cdot cos^2\theta_{ni} \qquad \text{Eq. 2- 35}$$

$$v_{ci} = \sum_{i=1}^{n} \rho_i (f_{scri} - f_{si}) \cdot \cos\theta_{ni} \cdot \sin\theta_{ni} \qquad \text{Eq. 2- 36}$$

$$v_{ci} \leq v_{cimax} \qquad \text{where} \qquad v_{cimax} = \frac{0.18\sqrt{f'_c}}{0.31 + \frac{24w}{a+16}} \qquad \text{Eq. 2- 37}$$

$$w = \varepsilon_1 \cdot s_{cr} \qquad \text{Eq. 2- 38}$$

$$s_{cr} \simeq \frac{1}{\frac{\cos\theta}{s_{mx}} + \frac{\sin\theta}{s_{my}}} \qquad \text{Eq. 2- 39}$$

The main parameters influencing the shear stress across a crack are the maximum aggregate size (a), crack spacing (s_{cr}), longitudinal strain due to cracking ($\Delta\varepsilon_{1cr}$), total strain in reinforcement (ε_{1cr}), average strain (ε_1), and angle of reinforcement (θ_{ni}) (Vecchio & De Lorenzi, 2009).

2.4.3.1 CSA code

MCFT formulations have been used worldwide and incorporated into various design standards, including CSA A23.3, for the purpose of shear design. For analyzing shear strength, the CSA standard defines V_c and V_s as the shear carried by concrete and stirrups, respectively. Based on CSA A23.3-19, the factored shear resistance can be determined by Equation 2-40 (CSA A23.3:19, 2019):

$$V_r = V_c + V_s + V_p \qquad \text{Eq. 2- 40}$$

Where V_p is the component in the direction of the applied shear of the effective prestressing force factored by ϕ_p. V_s for members with transverse reinforcement is equal to:

$$V_s = \frac{\phi_s A_v f_y d_v \cot\theta}{s} \qquad \text{Eq. 2- 41}$$

However, V_s will be zero for the members without shear reinforcement.

V_r has the maximum limitation based on Equation 2-42:

$$V_{r,max} = 0.25\phi_c f_c' b_w d_v + V_p \qquad \text{Eq. 2- 42}$$

Also, V_c can be calculated based on Equation 2-43:

$$V_c = \phi_c \lambda \beta \sqrt{f_c'} b_w d_v, which \begin{cases} \beta > 0.05 \\ \sqrt{f_c'} < 8MPa \end{cases} \qquad \text{Eq. 2- 43}$$

CSA A23.3-19 recommends two different methods called “simplified method” and “general method” for calculating β and θ. The simplified method estimates these two parameters based on

approximations. However, the general method considers more details by considering the effect of longitudinal strains (ε_x) and size effect in the formula.

1- Simplified Method:

For members without shear reinforcement and with a nominal maximum size of aggregate equal to 20 mm, θ shall be taken as 35° and β should be determined as:

$$\beta = \frac{230}{(1000+d_v)} \quad \text{Eq. 2- 44}$$

However, for all the other aggregate sizes, the formula can be adjusted by replacing the equivalent crack spacing parameter (s_{ze}) with d_v, where:

$$s_{ze} = \frac{35 s_z}{15+a_g} < 0.85 s_z \quad \text{Eq. 2- 45}$$

Which s_z is the crack spacing which should be considered with the minimum amount of d_v or the maximum distance between layers of distributed longitudinal reinforcement.

2- General Method

For the general method, the value of β is determined based on Equation 2-46:

$$\beta = \frac{0.40}{(1+1500\varepsilon_x)} . \frac{1300}{(1000+s_{ze})} \quad \text{Eq. 2- 46}$$

Where ε_x is:

$$\varepsilon_x = \frac{M_f/d_v + V_f - V_p + 0.5N_f - A_p f_{po}}{2(E_s A_s + E_p A_p)} \quad \text{Eq. 2- 47}$$

For members without shear reinforcement, s_{ze} can be calculated based on Equation 2-45.

2.4.4. Shear Crack Propagation Theory (SCPT)

2.4.4.1. Introduction

As elaborated in the preceding section, a crucial aspect requiring further research is the mechanical behaviour of various shear transfer mechanisms within a crack. However, until recently, there was a lack of unified mechanical approaches encompassing all seven fundamental stages of the process of shear failure for beams without shear reinforcement, as depicted in Figure 2-21 (Classen, 2020).

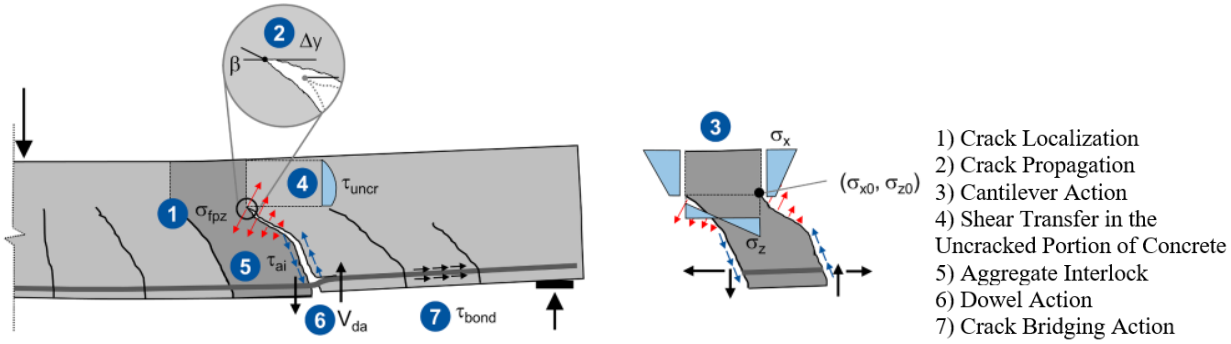

Figure 2-21 Elementary stages of the process of shear failure for members without shear reinforcement (Classen, 2020)

Although various research studies have investigated these parameters separately, no mechanical model was available that considered all the effective factors together. Moreover, most previous models have focused only on the shear failure state. However, studying the progress of crack growth and even in the uncracked zone is crucial to understanding the interaction between various shear transfer mechanisms which changes with different loading stages (Classen, 2020).

A new mechanical theory, named shear crack propagation theory (SCPT), was developed in which all 7 stages illustrated in Figure 2-21 are considered together to have a more precise understanding of shear behaviour and the process of crack propagation (Classen, 2020).

Figure 2-22 further illustrates the SCPT solution process. The location for investigation in this model is $d.\lambda_{cs}$ from the support (Fig. 2-22-a). There is a control section (cs) that includes two parts: the inclined crack section, and a vertical section which extends from the crack tip and continues

through the uncracked zone (Fig. 2-22-a). Figure 22-c shows the shear force-deformation history of four states of the shear crack propagation (Classen, 2020).

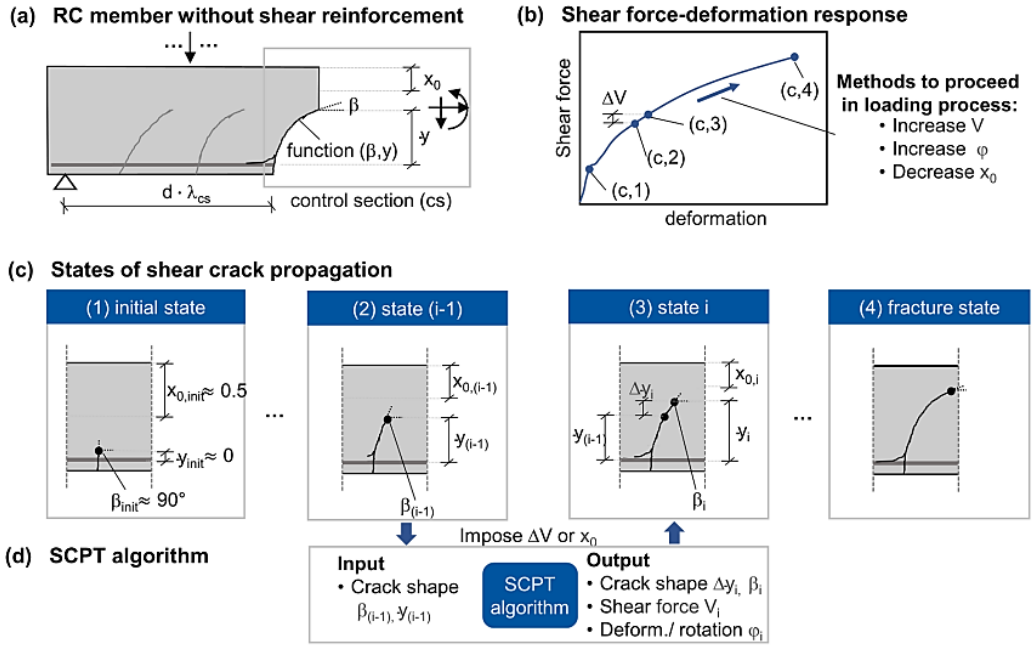

Figure 2-22 The procedure of the shear crack propagation (Classen, 2020)

In this method, the member can be divided into two sections. One of them is the area between two shear cracks which can be considered as concrete teeth and the other one is the compression zone (Fig. 2-23a).

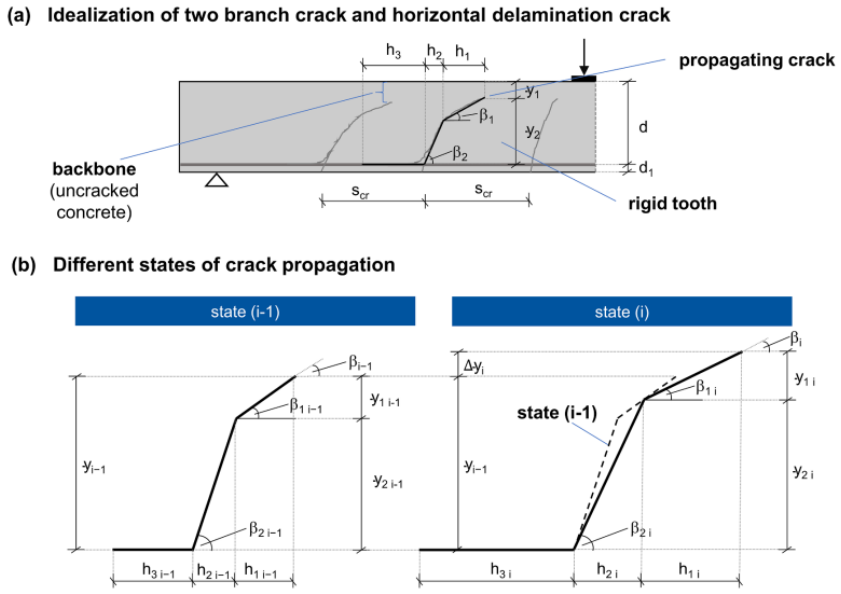

Figure 2-23 Crack geometry (Classen, 2020)

One of the main parameters which should be determined is the width of concrete teeth (spacing between two cracks). Reineck, Collins et al., Tung & Tue, and Cladera et al. considered the width of concrete teeth (S_{cr}) as 0.7(d-c) (in which c is the compression zone depth), 0.5d, and 0.7d respectively (Cladera et al., 2017; Collins et al., 2008; Reineck, 1991; Tung & Tue, 2016).

Based on Figure 2-24, there is one point which is the center of rotation (CR) which can change during the loading process. Another important point is the crack tip; the distance between this point and CR can be defined by x_1 which is positive (negative) when the shear crack is in the tensile (compression) zone (Fig. 2-24) (Classen, 2020).

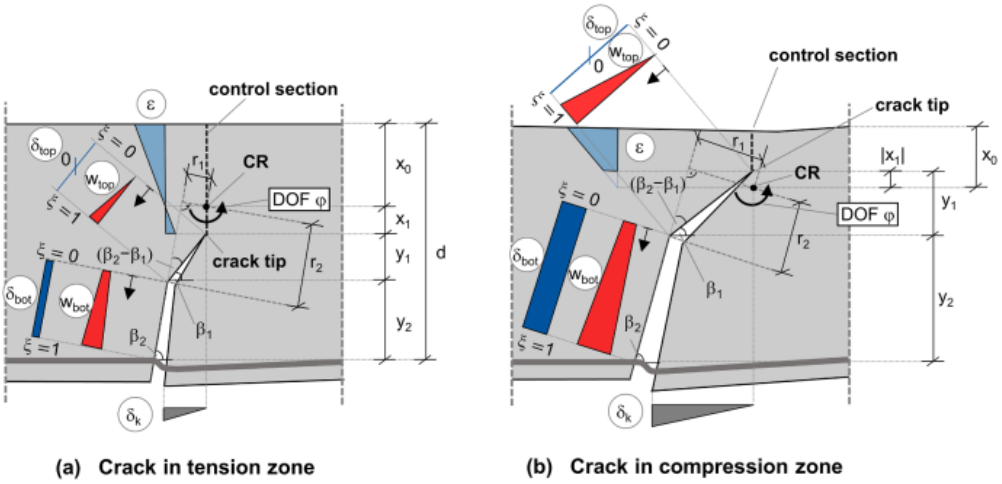

Figure 2-24 The kinematic model for two different crack opening zone (tension and compression zone (Classen, 2020)

Another important area is the fracture process zone (FPZ) which is the area with microcracks near the crack tip. In SCPT, it is supposed that the residual tensile stresses will become active within the fracture process zone. At this point, the crack propagation depends on the stress-strain behaviour according to the biaxial stress state at the crack tip propagation (Fig. 2-25) (Classen, 2020).

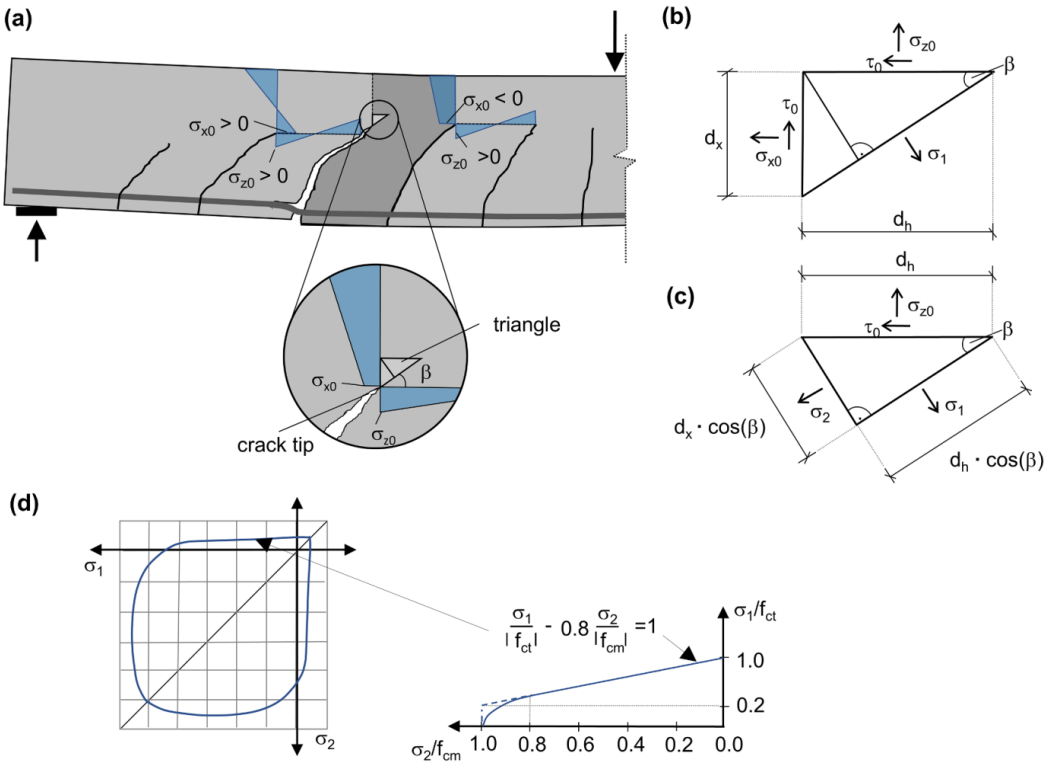

Figure 2-25 Fracture process zone, and the biaxial fracture (Classen, 2020)

Previous literature primarily emphasized shear failure but overlooked shear forces in the uncracked tension zone. However, when the shear failure occurs, the crack has propagated into the compression zone (Classen, 2020). Research by Reineck (1991) has shown that shear in the compression zone depends on geometric factors and stress transfer mechanisms within the crack, such as dowel action and aggregate interlock. Additionally, based on the Reineck study, the shear transmitted within the compression zone is constrained to a maximum of one-third of the overall shear capacity of a structural element. This limitation arises due to the maximum compression zone depth that is approximately 0.4 times the effective depth (d) for $\rho \approx 0.02$ (Eq. 2-48, and Fig. 2-26) (Reineck, 1991).

$$V = \frac{2}{3} c\, b_w\, v_n = \frac{2}{3}\frac{c}{z} V, \qquad z = d - \frac{c}{3} \qquad \text{Eq. 2- 48}$$

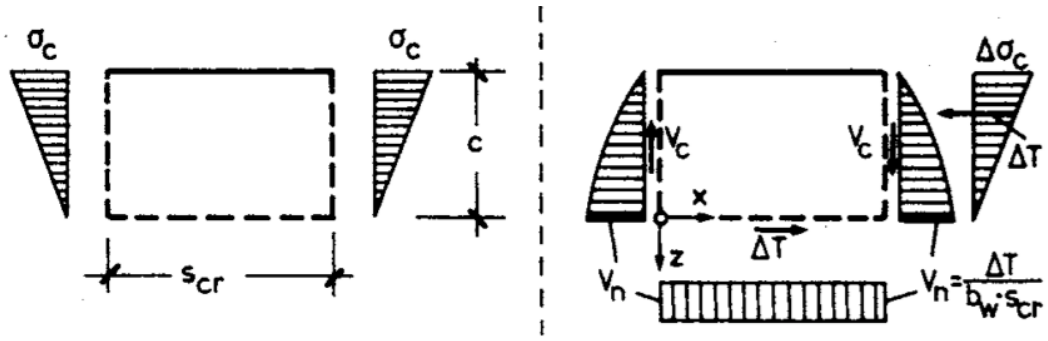

Figure 2-26 Forces diagram in compression zone (Reineck, 1991)

The importance of this issue is that in some members, it is possible that the failure of the members may occur because of the shear failure in the compression zone, and SCPT can solve this problem (Classen, 2020).

Classen (2020) showed that the normal stress reaches the uniaxial tensile strength for β=90^o (β is the shear crack propagation angle which is shown in Figure 2-22) and reaches the uniaxial compressive strength for β=0^o, while the shear stress for both situations will be zero. Furthermore, when the vertical stress is zero for β=45^o, the shear stress will be equal to the uniaxial tensile strength (f_{ct}). Finally, it shows that failure occurs in the flatter shear crack angles, and the shear crack can propagate into the compression zone even after the increase of the shear load (Classen, 2020).

The shear transfer mechanism caused after the concrete cracking can be divided into two different categories. One is kinematic behaviour which depends on crack deformations, steel strains and concrete strains, and the other one is constitutive behaviour which depends on shear transfer action. Obviously, the shear transfer between the uncracked concrete and in the propagation crack is different.

Several phenomena are dependent on the constitutive behaviour which are listed below (Fig. 2-27):

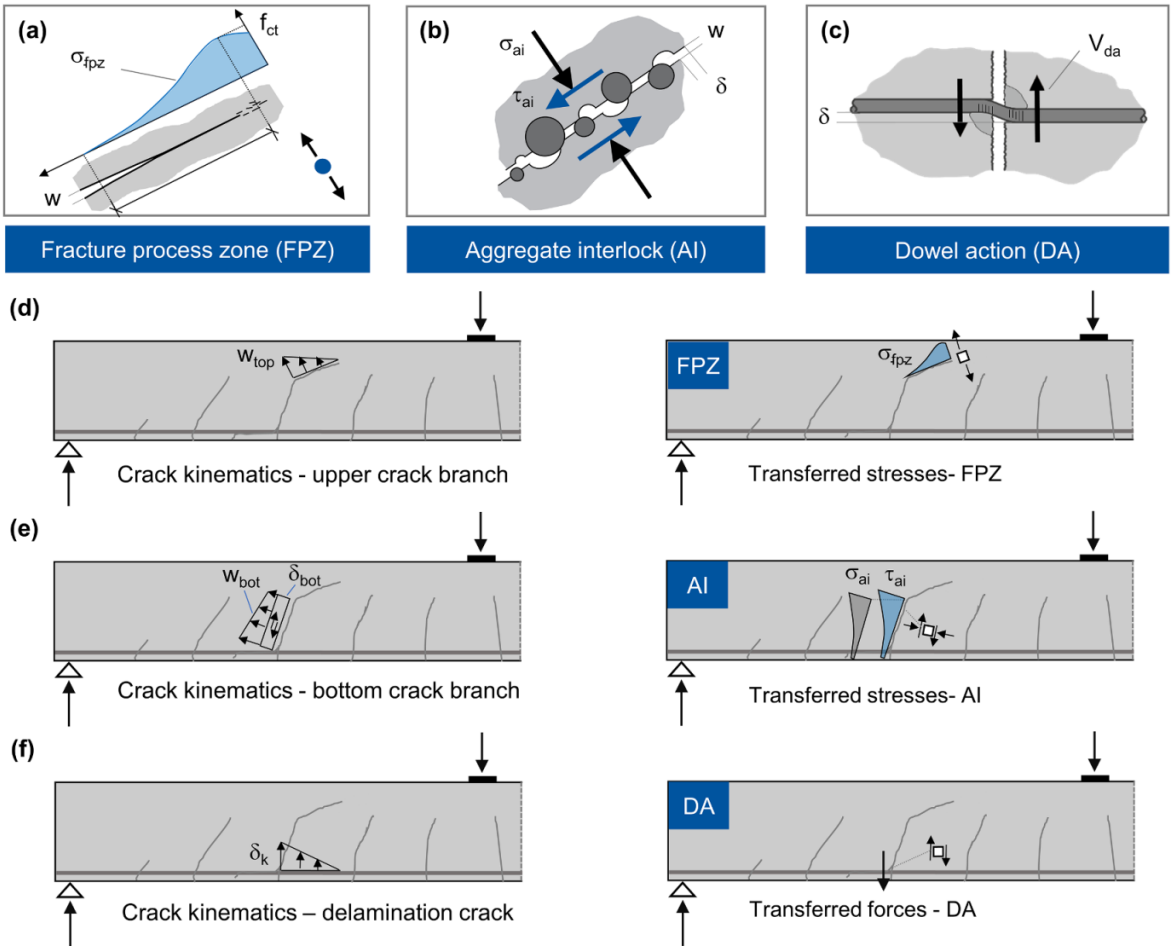

Figure 2-27 The process of shear transfer action among the shear cracks (Classen, 2020)

1- Fracture process zone (FPZ): the modeling for the growth of microcracks is often simulated by a cohesive behaviour of a discrete macro crack based on Figure 2-27a. In this mechanism, the concrete can transfer residual tensile stresses between two sides of the cracks until a certain amount of crack width is reached which will be defined as the maximum crack width. After passing this maximum crack width which often happens by increasing the shear and bending, the cohesive behaviour will disappear (as shown in Equation A-1 to A-7 in Appendix A) (Fig. 2-27a) (Classen, 2020).

2- Aggregate interlock: this phenomenon occurs when cracks are formed between aggregates and in the cement paste. One of the purposes of the longitudinal reinforcement is to lock

these two sides of the crack together. The activation of this phenomenon which is started by the sliding of cracked lips has a direct impact on the shear process (as shown in Equation A-8 to A-13 in Appendix A) (Fig. 2-27b) (Classen, 2020).

3- Dowelling action of reinforcement: this mechanism will be activated when the number of cracks exceeds a certain number and depends on several parameters such as the flexural stiffness of the longitudinal reinforcement, and the concrete that exists around the steel reinforcement. Besides, this action depends on the tensile strength of the concrete. The dowelling action not only does not lead to an extra force in the shear crack but also causes the loss of a secondary crack propagation at the tip of shear crack (As shown in Equation A-14 to A-17 in Appendix A) (Fig. 2-27c) (Classen, 2020).

When the element is exposed to bending stress, the longitudinal reinforcement will be under tensile force, leading to a strain. This strain influences the rotation (φ) of the shear crack in the control section. The strain of flexural reinforcement can be divided into two different sections (Fig. 2-28).

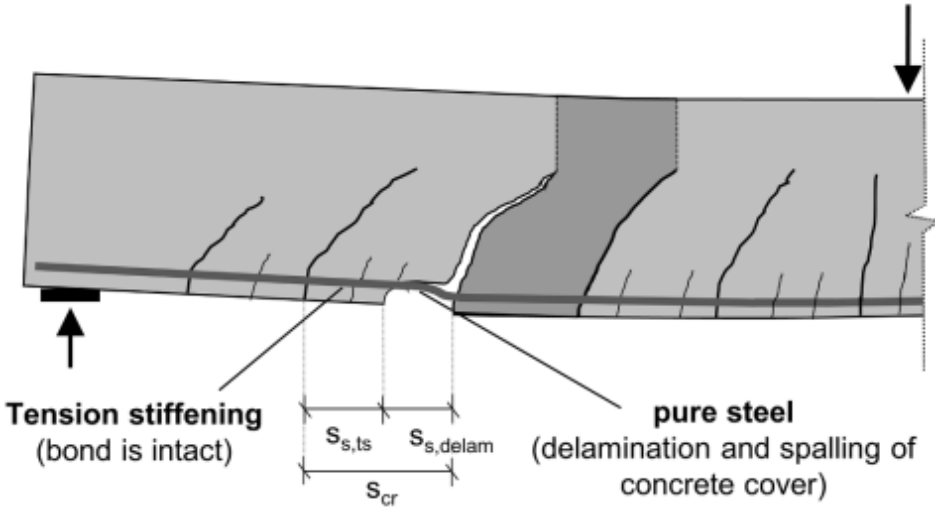

Figure 2-28 Strain in the region with tension stiffening and delamination (Classen, 2020)

The first one is for the area where there is not any bond, and all the concrete surrounding the reinforcement has been delaminated ($\varepsilon_{s,delam}$) (Equations A-18 to A-20 in Appendix A). The other

one is for the area where the bond between concrete and reinforcement is still there ($\varepsilon_{s,ts}$) (Equation A-21 in Appendix A). The average of these two strains and rotation φ can be calculated based on Equations A-22 and A-23 in Appendix A, respectively (Classen, 2020).

For analyzing the darker gray area in Figure 2-28, Kani (1964) considered this area as a tooth model which is like a restricted end member under vertical stress. He neglected the shear in the crack; however, there is a shear transfer action in the concrete tooth in reality and can be transferred between the two borders of the cracks. In SCPT, the length and geometric characteristics of cantilevers were also considered to determine the crack propagation into the compression zone (Fig. 2-29) (Classen, 2020).

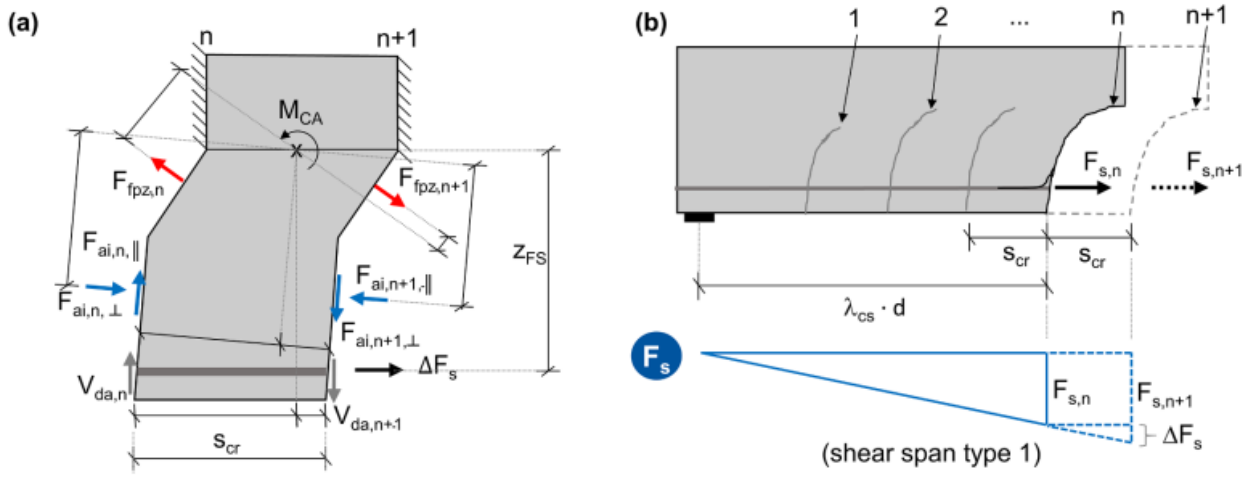

Figure 2-29 a) a dissected concrete tooth and its inner forces, b) tensile forces in every single tooth member (Classen, 2020)

2.4.4.2. SCPT algorithm

The SCPT algorithm employs an iterative strategy based on some initial assumptions. In this method, all the geometrical data, material properties, loading conditions, and the shear crack geometry in step (i-1) are used as inputs for step (i). Then, the transferred shear stress above the crack tip (τ_0) and the concomitant horizontal crack tip stress (σ_{x0}) will be calculated by estimating the crack extension path (β_{estim}, Δy_{estim}), the vertical crack tip stress ($\sigma_{z0,estim}$), and the estimated

shear crack rotation (φ_{estim}). After that, the crack opening, crack sliding, and the distance (x_1) between the center of rotation and crack tip should be determined. For the next step, it is necessary to compute the normal force and shear force within the uncracked concrete, and to assess the shear transfer action alongside the crack. From equilibrium, the total transferred shear force V_E, bending moment M_E in the control section, and the associated tensile force in the reinforcement F_s will be obtained (Fig. 2-30), and compared with initial assumptions. If it is valid, it means that a compatible equilibrium state and the propagation of crack is discovered. Otherwise, other initial assumptions should be considered (Classen, 2020).

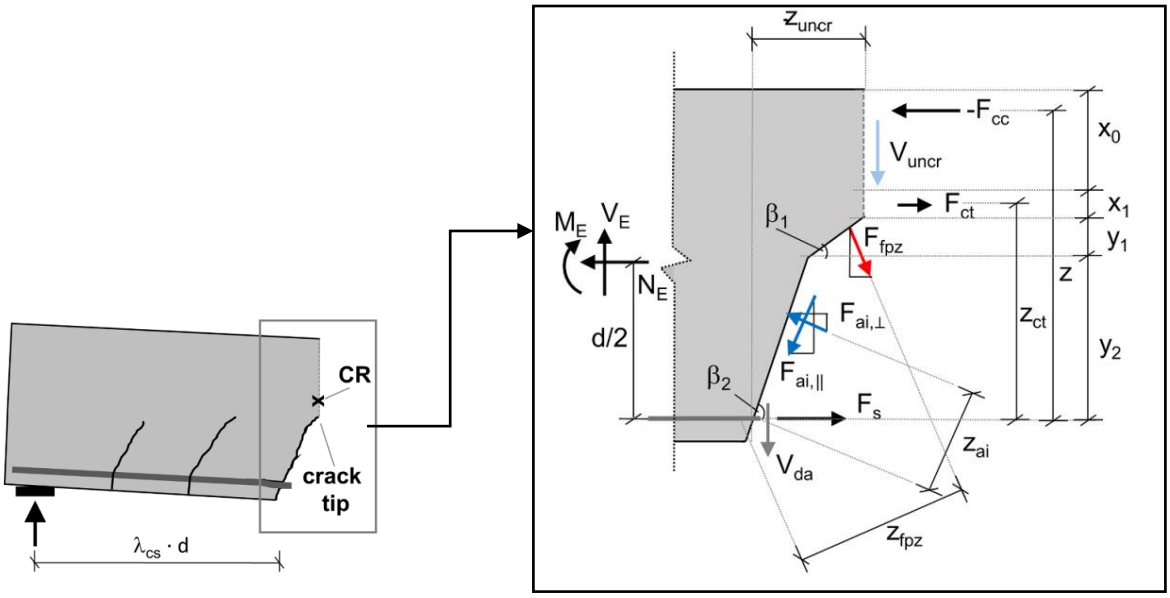

Figure 2-30 Free body and forces in the control section (Classen, 2020)

The outputs of the SCPT algorithm include β and y (representing crack geometry), φ (indicating the rotation of the control section due to deformations), as well as all internal forces (Classen, 2020). The SCPT algorithm is shown in Figure 2-31.

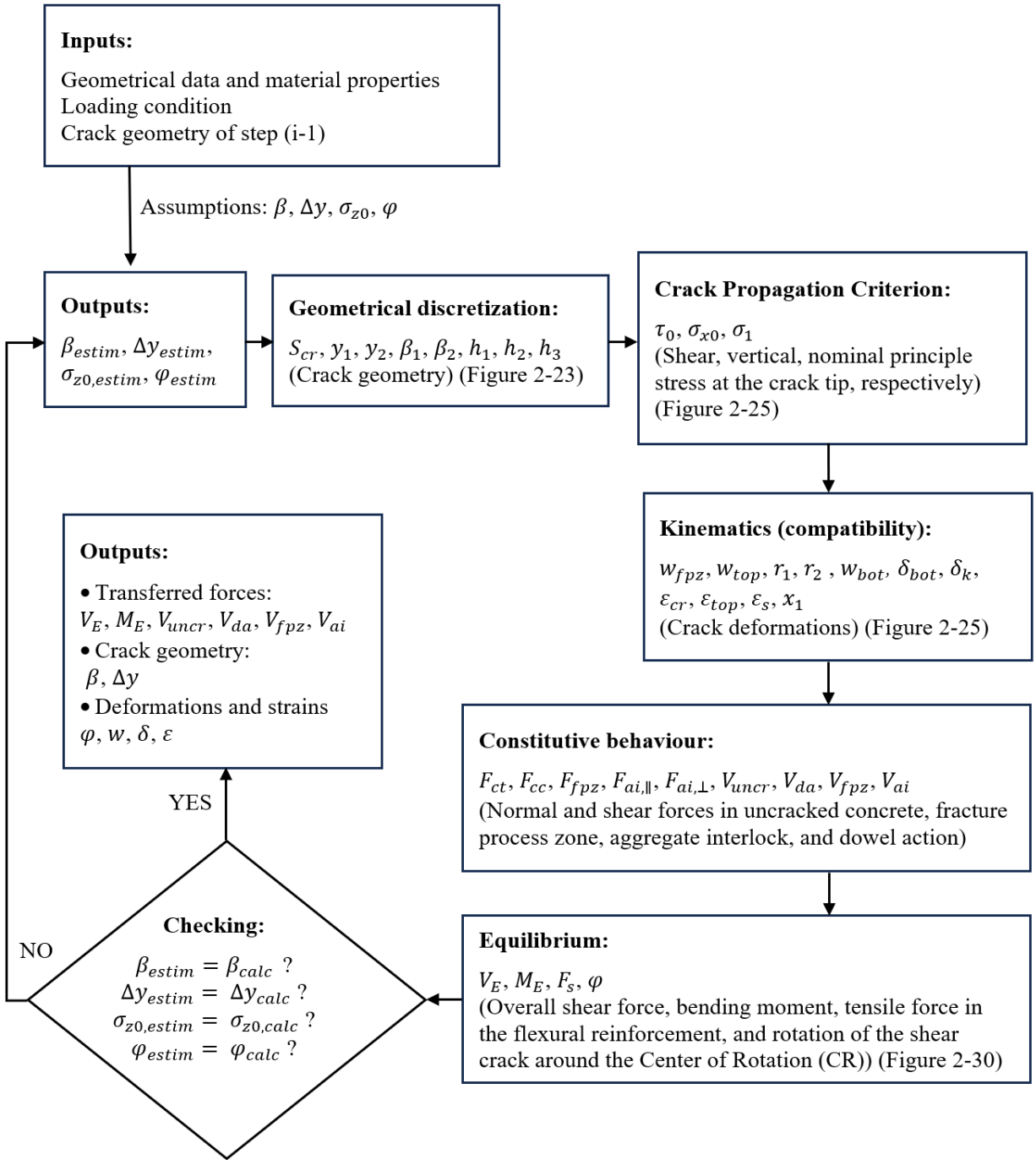

Figure 2-31 SCPT algorithm (Reproduced from Classen, 2020)

By this analysis and by considering a constant spacing for all shear cracks, we can access the location of critical crack which is not necessarily placed in the minimum shear capacity location. However, it is located at the tangent point of acting shear force and the shear capacity (Fig. 2-32) (Classen, 2020).

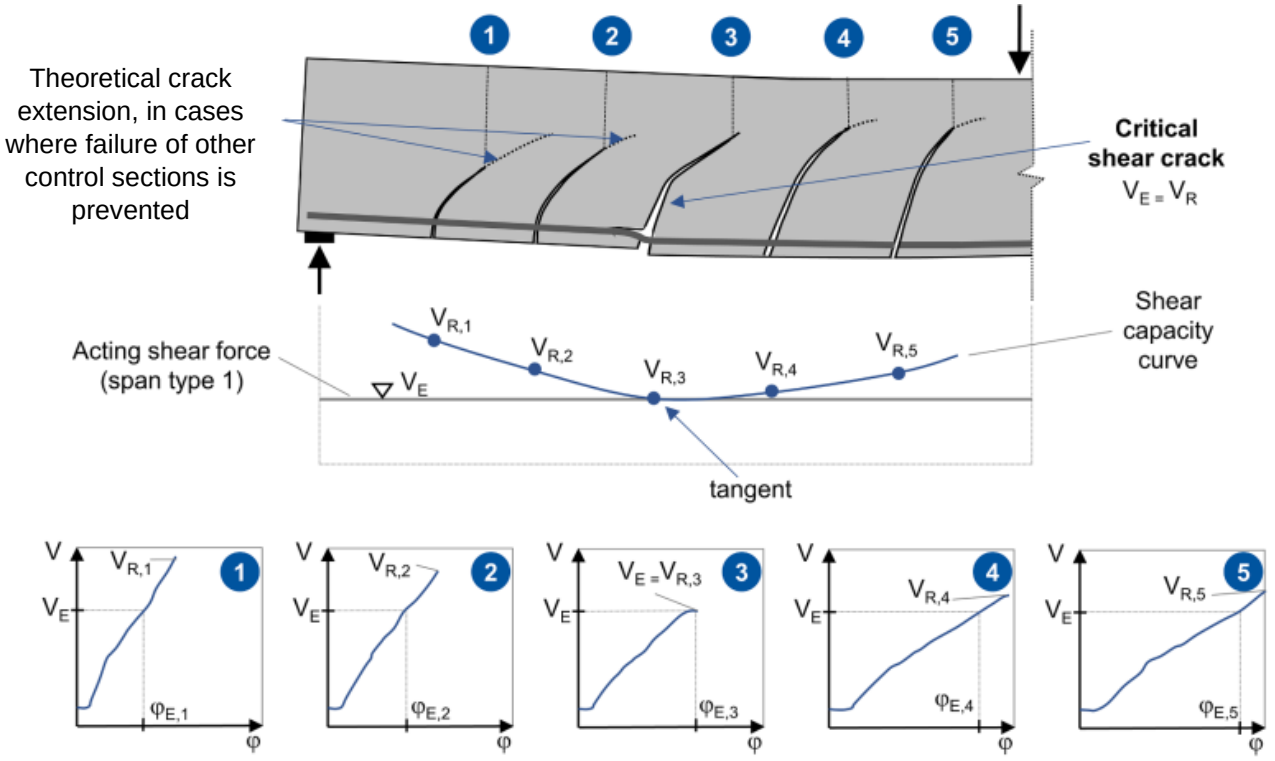

Figure 2-32 The location of critical control section based on shear response and deformation behaviour (Classen, 2020)

2.4.4.3. SCPT Results

The SCPT results can be allocated to four primary parameters which are shown in Fig. 2-33. One of them is the uncracked zone (compression zone) which can support between 40 to 50% of the shear contribution. By increasing the loads, the vertical stress on the crack tip will increase causing the transferred shear stresses within the uncracked concrete to be reduced (Classen, 2020). Some researchers consider this section of the element as the most important area for carrying the shear load (V_{uncr}) (Fig. 2-33a) (Rombach & Kohl, 2016).

The other one is the fracture process zone (FPZ) which can bear approximately 15% of the shear force. It should be mentioned that the crack width will not be opened by increasing the loads. However, it causes the crack propagation. The vertical component of the FPZ increases with additional loading because it acts like a compression force. This phenomenon leads to a flatter

shear crack propagation angle. In other methods like MCFT, it supposes that the crack tip is fixed and the contribution of FPZ in shear decreases with increasing rotation. However, SCPT has proven otherwise. Based on Figure 2-33b, by increasing the crack width and increasing the load, the shear contribution for FPZ does not decrease (V_{FPZ}) (Classen, 2020).

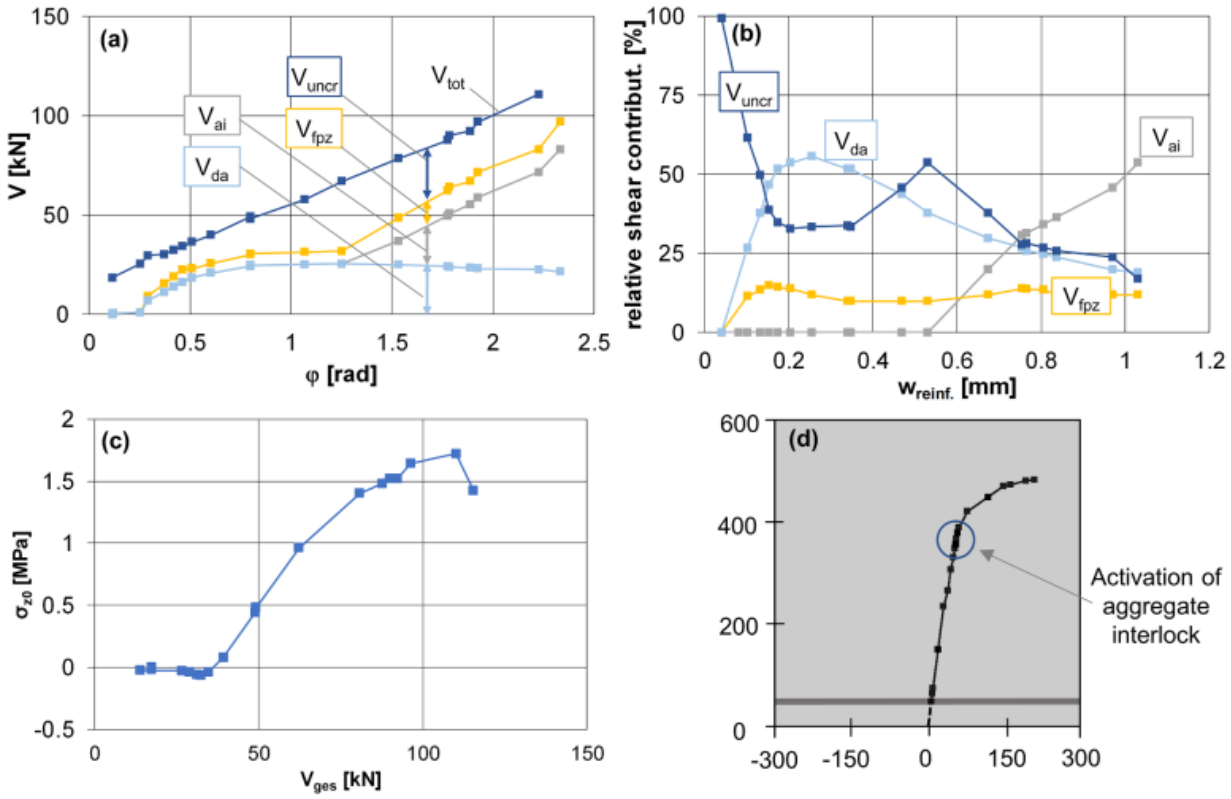

Figure 2-33 the effect of four phenomenon based on SCPT (Classen, 2020)

The third parameter is aggregate interlock which is known among researchers. This phenomenon will be activated late in the shear loading process, particularly when crack propagation starts deviating from a straight path and begins to curve (Fig. 2-33d). The reason for the curved crack shape and activation of aggregate interlock is because of sliding deformation increase in the straight crack at the bottom. This phenomenon contributes up to approximately 50% of shear strength. Although other methods indicated that the aggregate interlock stresses reduce by

increasing the crack opening, the most important aspect is the large sliding deformation effect in the crack (V_{agg}) (Classen, 2020).

The last parameter is the dowel action which is activated at the start of the loading when the vertical deformation component of the crack opening occurs. It will be activated just after the inclined bending crack forms. It should be mentioned that the dowel action is not activated for the pure bending action (vertical crack opening), as it requires an inclined crack with a vertical displacement (V_{da}) (Classen, 2020).

As reported by Classen (2020b), the shear failure process is triggered by crack propagation in the compression zone for the following reasons:

1- Referring to Figure 2-34a, two contradictory procedures can be observed for shear transferring in the FPZ. On one hand, there is a moderate reduction in the FPZ force due to crack propagation. On the other hand, an increase in the vertical force component of the FPZ is observed, attributed to the flattening caused by crack propagation. These two conflicting effects lead to the conclusion that the FPZ does not initiate shear failure (Classen, 2020).

2- Referring to Figure 2-34b, two contrasting mechanisms are evident in shear transfer within the aggregate interlock mechanism. As cracks propagate, the rotation of the crack becomes flattened, resulting in an increased lever arm between the center of rotation (CR) and the steeper bottom crack branch, accompanied by a rise in sliding deformation. Consequently, it can be inferred that despite the expansion of crack openings, the aggregate interlock can carry the shear stress, thereby negating the possibility that shear failure arises from the degradation of aggregate interlock (Classen, 2020).

3- The effect of dowel action on shear strength remains relatively consistent due to its inherently ductile behaviour, which remains unaffected by rotational changes in the control section. Consequently, dowel action does not serve as a mechanism capable of initiating or exerting influence on shear failure (Classen, 2020).

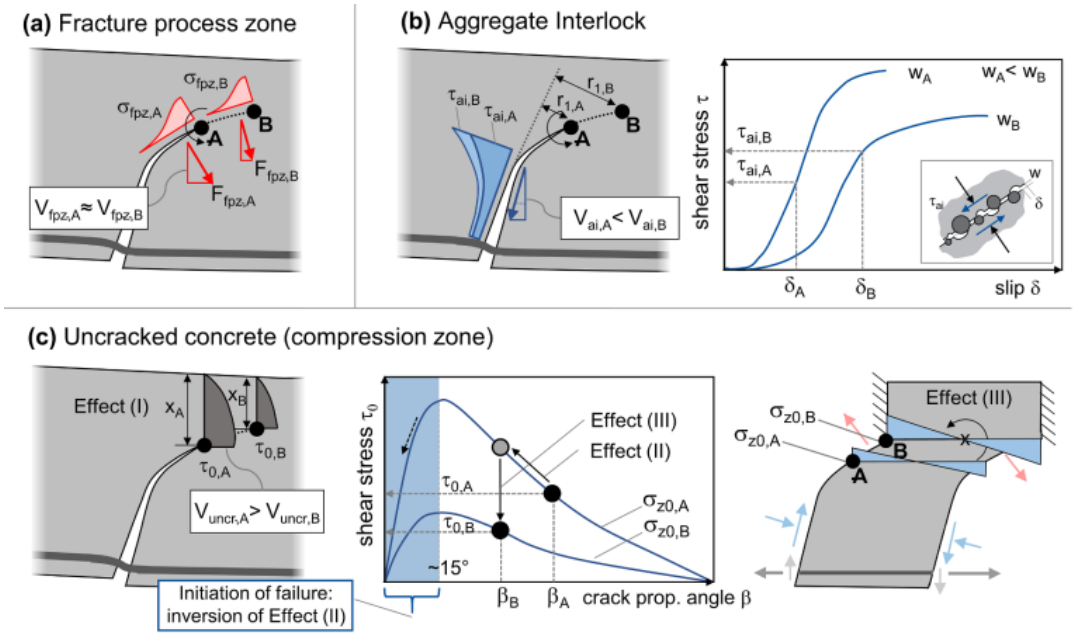

Figure 2-34 Physical explanation of shear failure based on SCPT (Classen, 2020)

Therefore, it can be concluded that shear failure occurs within the compression zone through crack propagation. The effects of shear failure can be divided in three different effects:

Effect (I): At the beginning of crack propagation into the compression zone, the angle of crack propagation is typically within the range of 20-45 degrees relative to the longitudinal direction. As the crack propagates, its vertical component reduces the compression zone.

Effect (II): the transferred shear stresses at the crack tip elevate by decreasing the shear crack angle, and the crucial angle for having the maximum shear stress is around 15^{o} (Fig. 2-34c).

Effect (III): when the crack angle declines by crack propagation, it leads to an increase in bending moment and vertical tensile stresses (σ_{z0}) and a decrease in the shear stresses at the crack tip (τ_0) (Classen, 2020).

The transferred shear stresses will be decreased as the crack propagation angle becomes flatter, resulting in a reduced compression zone and an increase in vertical stress at the crack tip. The crack propagation is stable when the angle is less than 15^{o}, after which the crack propagation will be unstable. In conclusion, it can be said that the crack angle flattening, and the sudden reduction of transferred shear stresses, will cause a brittle flexural shear failure (Classen, 2020).

2.4.4.3. SCPT Validation

This section focuses on the comprehensive validation of the SCPT algorithm through a rigorous analysis conducted at RWTH Aachen University in 2021 (Schmidt et al., 2021). The aim of this study was to assess the accuracy and reliability of the theoretical models by comparing their predictions with experimental results. By examining the fundamental aspects of shear crack propagation, it aimed to enhance the understanding of this critical phenomenon and establish a strong foundation for future engineering applications.

The experimental analysis involved meticulously designed tests and precise measurements to capture the intricate behaviour of shear crack propagation. The researchers devised a series of controlled experiments that simulated various real conditions by considering factors such as material properties, loading conditions, etc. These tests were carefully executed to generate accurate and representative data sets, serving as a basis for comparison against the theoretical predictions (Schmidt et al., 2021).

To facilitate the validation process, SCPT codes were developed using Python. By comparing the outputs of these codes with the experimental measurements, the researchers sought to evaluate the predictive capabilities and limitations of the theoretical models (Schmidt et al., 2021).

The validation process involved a comprehensive analysis of multiple parameters, including crack growth angles, shear strength by considering the contribution of several mechanisms such as

fracture process zone (FPZ), uncracked area in the compression zone, dowel action, and aggregate interlock. Through meticulous data analysis, they quantified the agreement between the experimental and SCPT results (Schmidt et al., 2021).

To validate the SCPT model, an experimental test setup of a simply supported beam was employed by Schmidt et al. in 2021. They tested beam specimens with varying conditions including flexural reinforcement ratio or maximum aggregate size to study the shear response of a beam without stirrups. Figure 2-35 illustrates both the test setup and the specifics of the reinforcement used in the experiment. The material specifications are presented in Table 2-1 (Schmidt et al., 2021).

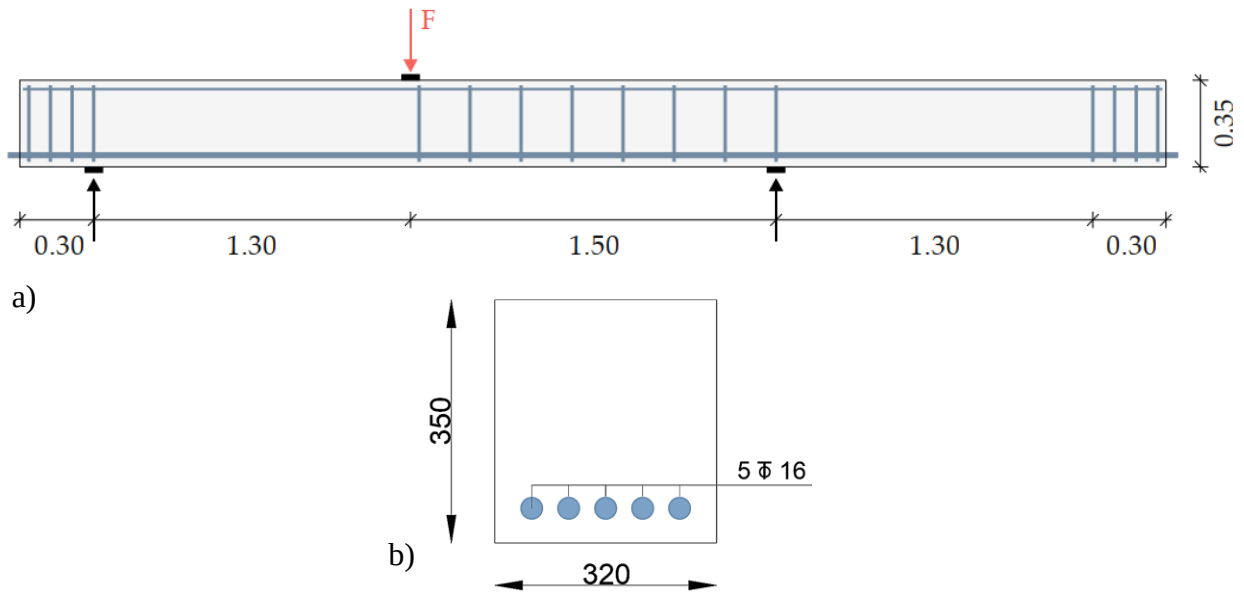

Figure 2-35 a) Section beam geometry (mm), b) Side view of beam (m) (Schmidt et al., 2021)

Table 2-1 Specimen Specifications (Schmidt et al., 2021)

L (mm)	a (mm)	d (mm)	b (mm)	h (mm)	d_s (mm)	n
2800	1300	300	320	350	16	5
f_{cm} (N/mm^2)	f_{ct} (N/mm^2)	E_c (N/mm^2)	E_s (N/mm^2)	f_y (N/mm^2)	f_u (N/mm^2)	
36.9	2.93	26800	199000	575	664	

Loading was carried out using a hydraulic jack with a force of 630 kN (Fig. 2-35). The root of the failure crack was located at $2.67 \times d$ from the support ($\lambda_{cs} = 2.67$). The results of the analysis indicated a shear failure load of 104.8 kN based on experimental testing. When comparing these experimental results with the values obtained through the SCPT, there was a difference of approximately 6%, with the SCPT estimating a shear failure load of 111.4 kN. While detailed results are presented by Schmidt et al. (2021), in summary, the SCPT accurately predicted the critical shear crack geometry and provided key insights regarding the contribution of various shear transfer mechanisms throughout the loading process (Schmidt et al., 2021).

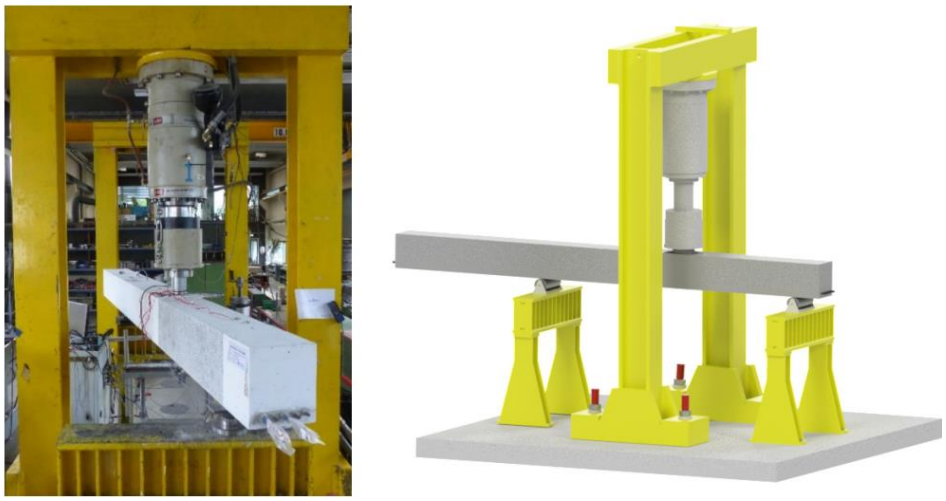

Figure 2-36 Test setup (Schmidt et al., 2021)

2.5 Fibre-Reinforced Polymers

Fibre-reinforced polymers (FRP) have gained significant attention in the field of structural engineering due to their exceptional mechanical properties, lightweight nature, and corrosion resistance. Steel reinforcement has long been used to enhance the strength and durability of concrete elements. However, FRP reinforcement offers numerous advantages over steel, including higher strength-to-weight ratio, corrosion resistance, and simpler installation due to its lightweight

nature. This makes it easier to transport, eliminates the need for welding or cutting, and facilitates shaping. The limitations of steel reinforcement, such as susceptibility to corrosion in aggressive environments can lead to premature deterioration and reduced service life of concrete structures. In contrast, FRP reinforcement eliminates the corrosion issue and offers enhanced durability, making it particularly suitable for applications in harsh or corrosive environments.

There are three main components of FRP composites:

1) Fibres: The role of fibres is to provide the mechanical properties such as strength and stiffness of the FRP. The most common fibre types in construction applications are glass or carbon. Glass FRP (GFRP) has relatively low strength and stiffness (compared to other FRP types), but is the most widely used due to its competitive cost. Conversely, carbon FRP (CFRP) has both high strength and stiffness.
2) Resin: It plays a protective role for fibres against environmental and mechanical damage which can also transfer shear stress between adjacent fibres. It can reduce the absorption of moisture and can improve the durability of FRP composites.
3) Interface: It is located between fibre and resin and can support the physical properties of the FRP such as durability, hygrothermal properties, stress corrosion, and fatigue behaviour.

Other components such as fillers and additives can also play a crucial role to reduce cost and shrinkage, and improving the mechanical, and physical properties and workability of the polymer, respectively (Bonić et al., 2015).

The stress-strain behaviour of FRPs is different in comparison with steel reinforcing bars, most notably with respect to their lower moduli of elasticity and linear elastic response up to failure (Fig. 2-37) (Noël, 2013).

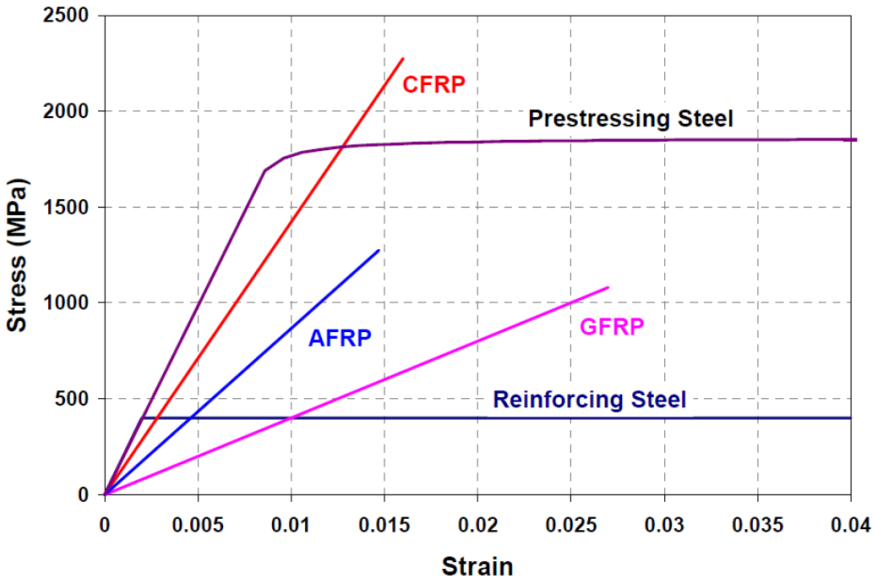

Figure 2-37 The behaviour of strain-stress for various types of materials (ISIS Canada, 2008)

2.5.1. FRP-Reinforced Concrete members

Key differences between steel- and FRP-RC members result from the lower values of FRP reinforcement stiffness, linear elastic behaviour of FRP, lower dowel resistance, and lower shear strength. This lower value makes the member more flexible and have greater crack widths. Linear elastic behaviour of FRPs results in a sudden failure by rupturing the reinforcement in under-reinforced members (Noël, 2013).

One of the principal parameters which should be considered in design is bond effect between reinforcement and concrete. Bond can affect the structural behaviour of a member including ultimate capacity, tension stiffening, crack spacing and widths, and deformability (Aiello et al., 2007). The bond strength of FRP-RC members is less than steel-RC members due their different surface configurations and mechanical properties (Okelo & Yuan, 2005). Bond effect in FRP-RC members depends on the diameter of reinforcement bar, surface roughness, concrete cover, bar spacing, and strength of the concrete (Fico et al., 2005).

By combining shear strength and bond behaviour topics in FRP-RC members, five mechanisms can be mentioned for resisting under shear stresses which are aggregate interlock, dowel action, shear stresses in uncracked concrete, arch action, and residual tensile stresses transmitted across cracks (Noël, 2013). Based on previous studies, it can be concluded that due to the more flexible nature of FRP reinforcements, FRP-RC members have wider and deeper cracks which have influence on shear capacities due to:

1) Aggregate interlock and residual stresses can be reduced due to the wider cracks.
2) Dowel action can be reduced due to the longitudinal orientation of the fibers, and lack of stiffness in the transverse orientation.
3) The contribution of uncracked concrete in compression zone can be reduced due to the deeper crack.

Thus, all these phenomena can reduce the shear strength of FRP-RC member without stirrups (El-Sayed et al., 2005).

There are several models for estimating the shear strength of FRP-RC members which will be discussed in the next sections.

2.5.3. Canadian Highway Bridge Design Code (CHBDC) (CSA S6:19)

Based on CSA S6:19, the factored shear resistance (V_r) shall be computed as follows:

$$V_r = V_c + V_{st} + V_p \quad \text{Eq. 2- 49}$$

Which V_{st} (V_s or V_{FRP}) refers to the steel or FRP stirrups which is not addressed in this research. The contribution of shear strength in concrete will be:

$$V_c = 2.5\beta\phi_c f_c' b_v d_{long} \quad \text{Eq. 2- 50}$$

Where d_{long} is the effective shear depth and can be calculated the same as RC beams which is:

$$d_{long} = max\{0.72h, 0.9d\}$$ Eq. 2- 51

Besides, β can be calculated according to the section 2.4.3.1 by considering the new ε_x which is:

$$\varepsilon_x = \frac{M_f/d_{long} + V_f - V_p + 0.5N_f - A_{FRP}f_{po}}{2(E_sA_s + E_{FRP}A_{FRP})} \leq 0.003$$ Eq. 2- 52

2.5.4. Design And Construction of Building Structures with Fibre-Reinforced Polymers (CSA S806-12)

Based on CSA S806-12, the factored shear resistance of members with longitudinal FRP reinforcement shall be calculated as follows:

$$V_r = V_c + V_s$$ Eq. 2- 53

Which V_s (V_{ss} or V_{sF}) is referred to the steel or FRP stirrups which is not addressed in this research.

Besides, V_r cannot exceed as follows:

$$V_{rmax} = 0.22\phi_c f_c' b_w d_v + 0.5V_p + \left[\left(M_{dc}V_f\right)/M_f\right]$$ Eq. 2- 54

The contribution of shear strength in concrete (V_c) will be equal to:

$$V_c = 0.05\lambda\phi_c k_m k_r (f_c')^{\frac{1}{3}} b_w d_v \begin{cases} \leq 0.22\phi_c\sqrt{f_c'}b_w d_v \\ \geq 0.11\phi_c\sqrt{f_c'}b_w d_v \end{cases}$$ Eq. 2- 55

Where:

$$k_m = \sqrt{\frac{V_f d}{M_f}} \leq 1.0$$ Eq. 2- 56

$$k_r = 1 + (E_F\rho_{Fw})^{\frac{1}{3}}$$ Eq. 2- 57

Equation 2-54 should be modified for some reasons which are listed below:

1- Arch effect:

The support reaction causes compression in the beam within a distance of 2.5d from a support which the shear strength can be modified by the adding the factor k_a:

$$k_a = \frac{2.5}{\frac{M_f}{V_f d}} \begin{cases} \leq 2.5 \\ \geq 1.0 \end{cases} \quad \text{Eq. 2- 58}$$

2- Member size:

For structural members with an effective depth greater 300 mm, or without shear reinforcement, the shear strength should be modified by the adding the factor k_s:

$$k_s = \frac{750}{450+d} \leq 1.0 \quad \text{Eq. 2- 59}$$

2.5.5. Guide for the Design and Construction of Structural Concrete Reinforced with Fiber-Reinforced Polymer (FRP) Bars (ACI Code 440.11-22)

According to ACI 318, the nominal shear strength for RC beams (V_n) will be the sum of the contribution of shear strength in concrete (V_c) and steel shear reinforcement (V_s). However, the contribution of shear capacity of concrete for FRP-RC beams will be equal to (ACI Code 440.11-22, 2022):

$$V_c = \max\left\{5\lambda_s k_{cr}\sqrt{f_c'} b_w d, 0.8\lambda_s\sqrt{f_c'} b_w d\right\} \quad \text{Eq. 2- 60}$$

Where k_{cr} is:

$$k_{cr} = \sqrt{2 \cdot n_f \cdot \rho_f + \left(n_f \cdot \rho_f\right)^2} - n_f \cdot \rho_f \quad \text{Eq. 2- 61}$$

Where: $n_f = {E_f}/{E_c}$, and $\rho_f = {A_f}/{b_w d}$

And the size effect modification factor (λ_s) for members without shear reinforcement ($A_{fv} < A_{fv,min}$) is as follows:

$$\lambda_s = \sqrt{\frac{2}{1 + (d/10}} \leq 1.0 \qquad \text{Eq. 2- 62}$$

2.6 Summary and Research Gaps

In this chapter, various approaches have been studied, namely empirical, mechanical, MCFT (Modified Compression Field Theory), and SCPT (Shear Crack Propagation Theory) to analyze the shear capacity of RC members. Empirical models cannot account for all the parameters influencing shear strength due to the complexity of shear behaviour, and the results can be varied due to the initial conditions. Mechanical methods aim to provide a rational understanding, yet the complexity of shear phenomena often poses challenges in comprehensive modeling. While empirical models lack inclusiveness, mechanical approaches strive for rationality.

MCFT delves deeper into material behaviour and stress distribution, refining predictions. However, SCPT, on the other hand, focuses on crack propagation and offers valuable insights into shear failure mechanisms by combining the crack kinematics with constitutive behaviour.

While SCPT is currently employed for steel-RC beams, its applicability can be extended to FRP-RC beams. This thesis aims to broaden the SCPT approach to encompass FRP-RC beams, exploring the influence of parameters such as the modulus of elasticity. Additionally, various mechanisms like dowel action and tension stiffening for FRP-RC beams will be thoroughly examined and discussed.

Chapter 3

Parametric Analysis

3.1 Introduction

To date, the SCPT has only been applied to steel-RC members, although there is no inherent limitation in the model to any particular reinforcement type provided that appropriate constitutive models are adopted. Although steel remains the most common reinforcing material for concrete structures due to its favourable mechanical properties and competitive cost, the use of FRP reinforcing bars continues to increase around the world as a corrosion-resistant alternative, particularly in marine environments and where de-icing salts are used. The mechanical properties of FRP reinforcement differ from steel in several ways that can influence shear behaviour of RC beams. The relatively lower modulus of elasticity of FRP means that, for the same reinforcement ratio, wider and deeper cracks will develop compared to steel-RC members, reducing shear transfer associated with aggregate interlock and the depth of the uncracked compression zone. Similar effects also influence the contribution of dowel action and tension stiffening.

Due to its mechanical basis, the SCPT is well-suited to investigate the contributions of various shear transfer mechanisms and develop a deeper understanding of the effects of reinforcement type

on overall shear behaviour of RC beams. In this chapter, a preliminary parametric analysis is presented to investigate the effects of incorporating FRP material properties within the SCPT method.

The analysis is based on a reference steel-RC beam (320 mm wide x 350 mm height, shear span-to-depth ratio of 4.33, containing five 16 mm diameter steel reinforcing bars, and maximum aggregate size of 16 mm) previously tested (Fig. 2-35) and analysed by Schmidt et al. (2021) and modified in three steps to account for the different mechanical properties of FRP reinforcement:

Step 1: The beam geometry and reinforcement ratio were kept constant, and the elastic modulus of the longitudinal reinforcement was varied to represent a range of commercially available FRP materials. By systematically varying this parameter, its influence on the behaviour and performance of the FRP-RC beams under shear loading conditions can be clearly observed. In particular, the reinforcement stiffness directly influences the width of cracks (aggregate interlock) and neutral axis depth (compression zone). Thus, the Young's modulus of the reinforcement was changed from E_s = 200 GPa (steel) to E_f = 50, 100, and 150 GPa representing a range of FRP materials.

Step 2: Additionally, the effect of FRP reinforcement on dowel action was evaluated. Although it is explained in the previous sections that the transverse direction of FRP reinforcing bars does not have high stiffness in comparison to the longitudinal direction, the splitting strength of the concrete cover is not negligible and is the dominant component of dowel strength. Thus, accounting for the effect of dowel action in FRP-RC beams will be discussed in the next sections.

Step 3: Furthermore, an important aspect addressed in this research is the consideration of tension stiffening on shear capacity, which is often neglected for steel-RC members (Fig. 2-18, 2-19, and 2-28). Tension stiffening results from the bond between reinforcement and concrete that engages the concrete in tension between two cracks and is more significant for reinforcement with lower moduli of elasticity since the concrete takes on a larger proportion of the tension force resultant in a given cross-section. Thus, the effect of FRP material is applied by adding a ratio to the tension stiffening formulas.

By conducting this preliminary parametric analysis, this research aimed to contribute to the existing knowledge on FRP-RC beams and their behaviour under shear loading. The investigation of different design parameters, the inclusion of the FRP's effect on dowel action, and the consideration of tension stiffening provide insights into the overall performance of FRP-RC beams in shear.

3.2 Validation of RC Beams

First, a validation of the SCPT code for analyzing shear failure in a beam without shear reinforcement was conducted and compared to the results obtained by Schmidt et al. (2021) (Fig. 3-1). Four primary mechanisms will be discussed to evaluate the results of the analysis:

- Shear in the uncracked zone (V_{uncr})
- Shear in the fracture process zone (V_{FPZ})
- Shear transfer by aggregate interlock, activated once the crack propagation starts to become curved and results from sliding deformation of the crack (V_{ai})
- Shear transfer associated with dowel action, activated just after the inclined bending crack forms (V_{da}).

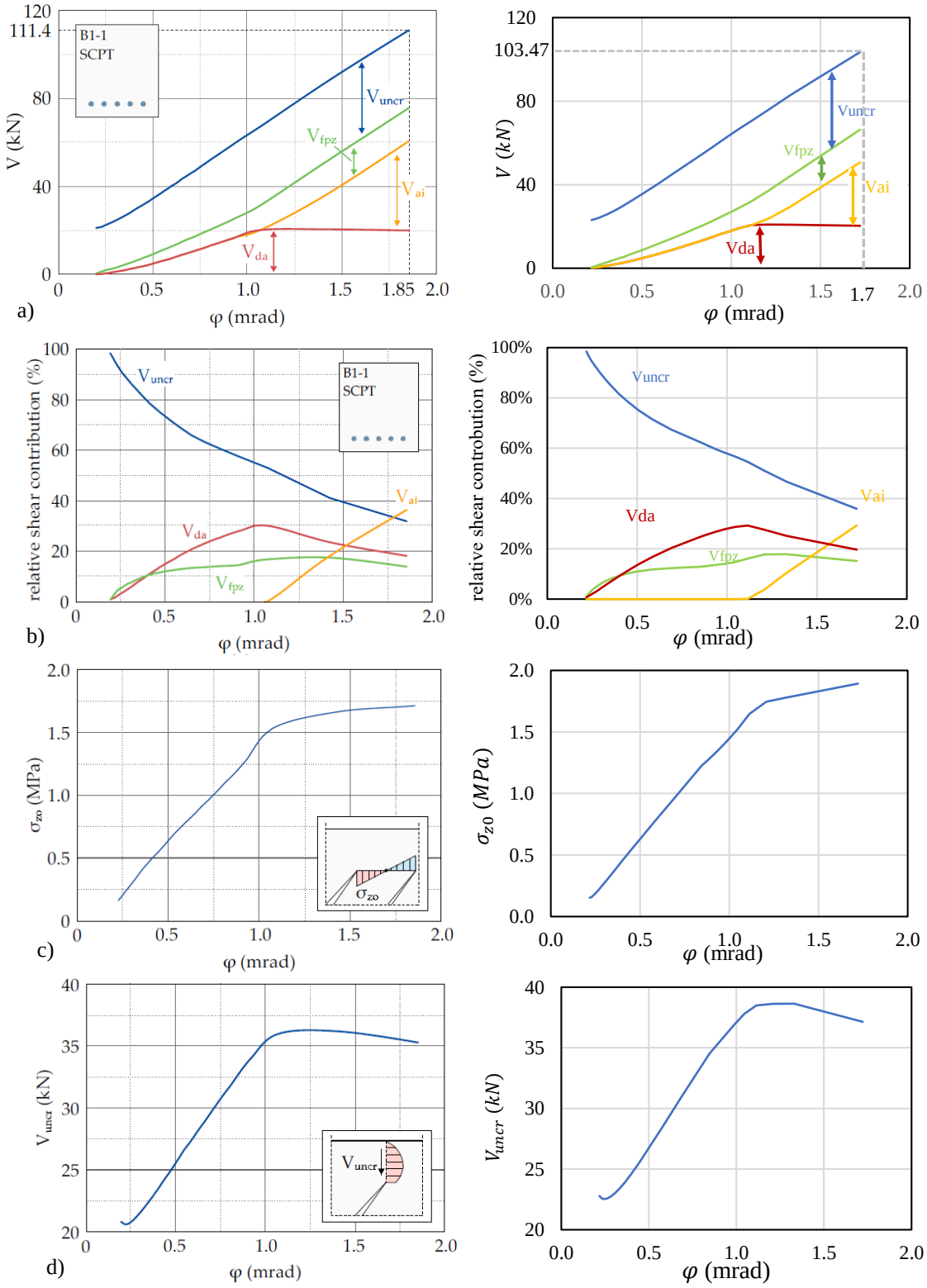

Figure 3-1 The SCPT results comparing shear crack rotation and a) shear force, b) relative shear contribution, c) vertical crack tip stress, and d) absolute shear force in uncracked zone (left sides are based on the Schmidt analysis (Schmidt et al., 2021), and the right sides are based on this research).

The aim was to assess the agreement and consistency between our findings and their established results. In the Schmidt et al. study, the predicted shear failure based on SCPT was reported as 111.4 kN, while the experimental results indicated a shear failure value of 104.8 kN. Upon analyzing our results, it is found that the code produced a shear failure value of 103.5 kN. Importantly, this value was remarkably close to the experimental results reported by Schmidt et al., suggesting a strong agreement between our analysis and the experimental observations. Figure 3-2 also presents the comparison of crack geometry between Schmidt's analysis and this research.

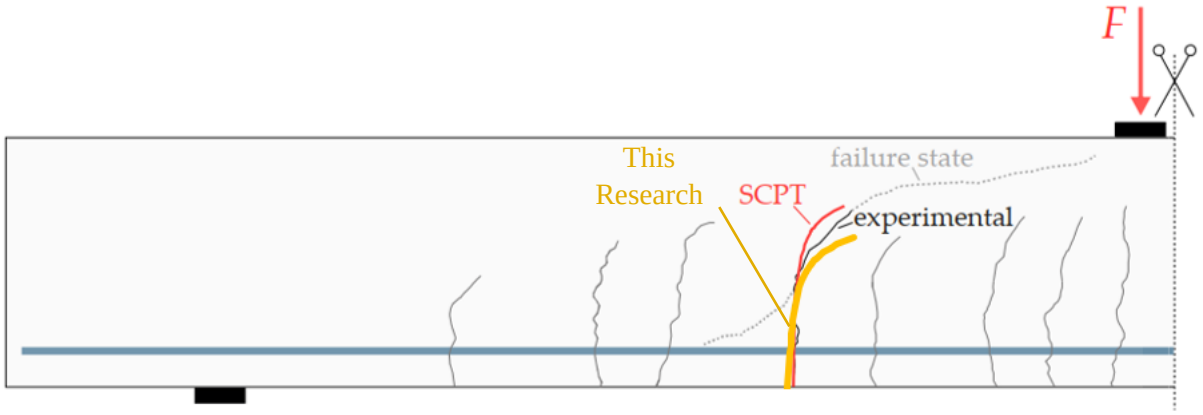

Figure 3-2 The comparison of crack geometry between Schmidt analysis (Schmidt et al., 2021), and this research.

Based on the comparison of the shear failure values, it can be concluded that our validation code performed well, providing results that closely aligned with the experimental data. Minor discrepancies were observed between this analysis and the previous work reported by Schmidt et al., which are likely attributed to differences in initial assumptions such as the first point of the crack propagation ($x_{0,1}$), and the also the crack propagation increment (Δx). Initial assumptions for values of β, Δy, σ_{z0}, and φ, as well as constitutive material models, can also influence results. Initial values used in this research are summarized in Table 3-1.

Table 3-1 The initial inputs and assumptions for this research based on Schmidt analysis (Schmidt et al., 2021).

L (mm)	**a (mm)**	**d (mm)**	**b (mm)**	**h (mm)**	**d_s (mm)**	**n**	**A_s (mm^2)**
2800	1300	300	320	350	16	5	1005.31
f_{cm} (N/mm^2)	**f_{ct} (N/mm^2)**	**E_c (N/mm^2)**	**E_s (N/mm^2)**	**f_y (N/mm^2)**	**λ_{cs}**	**ρ_l**	**d_{ag} (mm)**
36.9	2.93	26800	199000	575	4.33	0.01047	16
α	**Δy (mm)**	**β (degree)**	**σ_{z0} (N/mm^2)**	**φ (degree)**	**S_{cr} (mm)**	**$x_{0,1}$ (mm)**	**Δx (mm)**
0.3	50	90	0.02	0.0015	0.7d	0.48d	3

Note: $x_{0,1}$ is the first point of crack propagation.

3.3 Modulus of Elasticity

Due to the inherent advantages offered by FRP reinforcing bars, including high durability, an outstanding ratio of strength-to-weight, and favourable fatigue properties, these materials have emerged as a promising alternative to traditional steel reinforcement in various structural applications. However, a notable challenge associated with FRPs is their relatively lower modulus of elasticity in comparison with conventional materials such as steel. The modulus of elasticity, also known as Young's modulus, is a fundamental mechanical property that characterizes the stiffness or rigidity of a material. It measures the ability of material to deform elastically in response to an applied stress. Due to the unique behaviour exhibited by FRPs and the lack of consensus among scholars regarding a definitive approach for predicting shear failure in these materials, there exists a pressing need to address this issue through innovative research.

The primary objective of this chapter is to investigate the influence of modulus of elasticity on the shear failure. By exploring new methodologies and theoretical frameworks, it is endeavoured to gain comprehensive insights into the underlying factors influencing shear strength in FRPs (Marí et al., 2014).

Additionally, it is important to consider the effect of crack width on structural elements without stirrups, as this phenomenon can have a more detrimental impact on FRP-RC beams, primarily due to their lower modulus of elasticity. In structural elements where stirrups are not provided, the absence of lateral confinement can lead to an increase in crack widths. The susceptibility to widening cracks is more pronounced in FRP reinforced beams owing to their lower modulus of elasticity when compared to traditional reinforcement materials. Thus, it can have effect on aggregate interlock and dowel action.

In this section, the Young's modulus of the reinforcement will be varied to represent the range of commercially available FRP materials and their influence on shear behaviour.

3.3.1. Results

Figure 3-3 presents the shear force vs. crack rotation for RC beams having the same geometry and reinforcement as that from Schmidt et al. (2021), except with different values of elastic modulus of the reinforcement. The shear capacities corresponding to various elastic moduli are presented in Table 3-2.

Table 3-2 The absolute values of various components at shear failure for different moduli of elasticity

$V_{uncr}\ (kN)$	$V_{FPZ}\ (kN)$	$V_{ai}\ (kN)$	$V_{da}\ (kN)$	Total $V\ (kN)$
E = 200 GPa				
36.97	15.93	30.23	20.34	103.47
E = 150 GPa				
32.83	13.56	28.44	20.23	95.06
E = 100 GPa				
28.13	10.91	25.16	20.18	84.38
E = 50 GPa				
23.75	4.88	0.00	20.76	40.39

Decreasing the modulus of elasticity from 200 GPa to 150 GPa reduced the ultimate strength by only 9%, whereas reinforcement with an elastic modulus of 50 GPa exhibited a shear capacity that was 61% lower than the reference beam.

For reinforcement moduli between 100 and 200 GPa, the contribution of dowel action remained constant at about 20 kN beyond a certain shear crack rotation angle (between 1.0 to 1.5 mrad), which also corresponded to the point where aggregate interlock began to increase. However, for the lowest value of modulus of elasticity (E=50 GPa), dowel action contribution was still increasing beyond 2 mrad rotation, and aggregate interlock did not contribute to shear capacity.

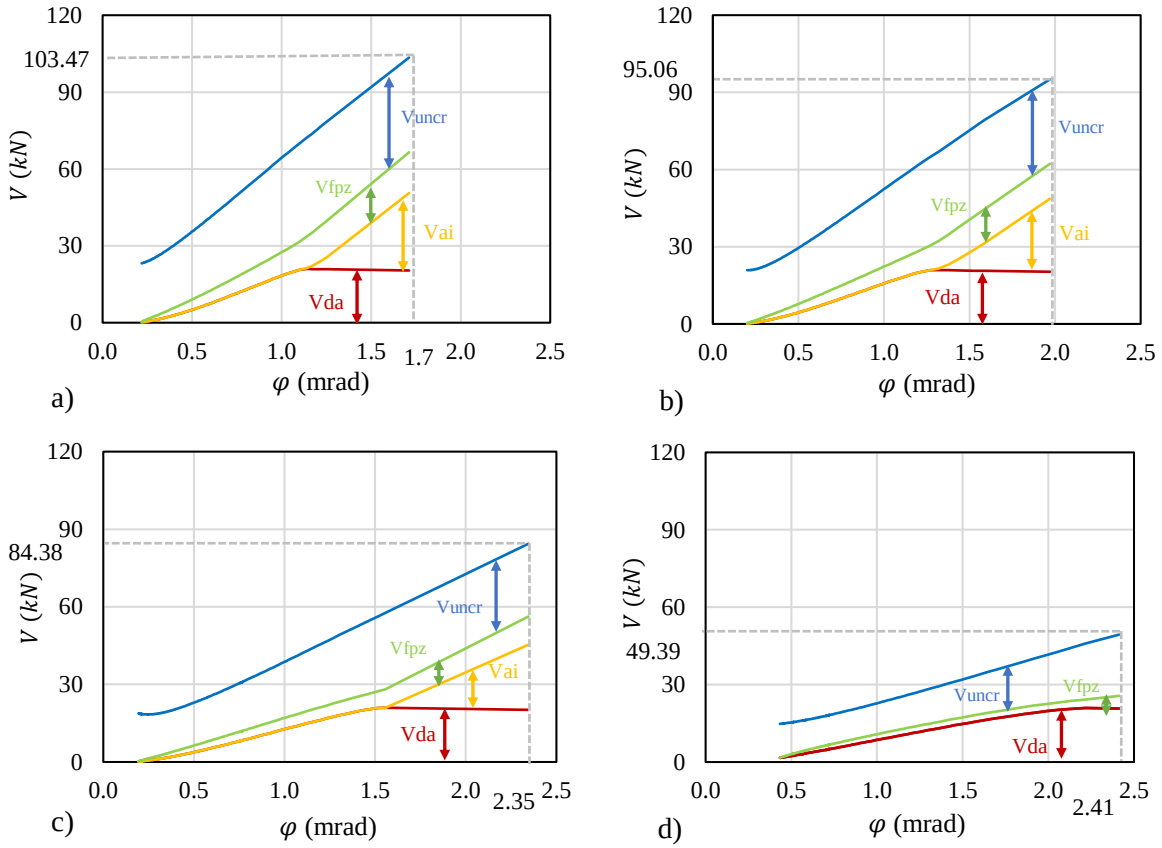

Figure 3-3 The relationship between shear force and crack rotation for various moduli of elasticity: a) E = 200 GPa, b) E = 150 GPa, c) E = 100 GPa, and d) E = 50 GPa.

In general, the combined contribution of dowel action and fracture process zone were relatively less affected by changes in the elastic modulus, whereas a significant effect on the compression

zone and aggregate interlock was observed which is attributed to the effect of reinforcement stiffness on limiting the width and depth of shear cracks. Besides, it can be seen that by decreasing the modulus of elasticity, the crack opening at the height of reinforcement will be increased which is due to the reinforcement stiffness (Fig. 3-4).

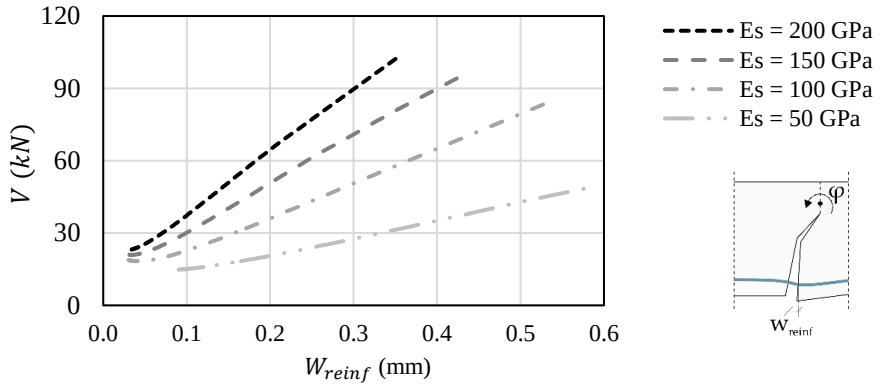

Figure 3-4 The relationship between shear force and crack opening at the height of reinforcement layer.

Furthermore, Figure 3-5 presents the contribution of each mechanism in relative terms. In the early stages of loading, almost all the shear force is carried by the uncracked concrete; although the value of V_{uncr} remains relatively constant throughout the test, its relative contribution decreases rapidly as the crack rotation increases. Figure 3-6 shows that the crack height increased with decreasing values of Young's modulus. At failure, the contribution of the uncracked zone was approximately 50% for the low modulus reinforcement (50 GPa) but only about 30-35% for reinforcement with moduli between 100 to 200 GPa (Table 3-3). The shear transferred through the fracture process zone remained relatively stable at approximately 10-15% of the total shear force regardless of the reinforcement stiffness.

The contribution of dowel action and aggregate interlock were related; dowel action was more dominant at lower values of crack rotation (i.e., lower angle of inclination), reaching a peak value between 30 to 50% of the total shear force before gradually decreasing to a value between 20 to 45% at the failure load. The peak value for dowel action coincided with the aggregate interlock

mechanism engaging in resisting shear, which quickly increased to around 30% of total shear for beams with reinforcement stiffness between 100 and 200 GPa. Conversely, aggregate interlock did not play a role in the shear resistance of the beam with low reinforcement stiffness (50 GPa).

Table 3-3 The percentage of various components at shear failure for different moduli of elasticity

V_{uncr}	V_{FPZ}	V_{ai}	V_{da}	Total V
E = 200 GPa				
35.7%	15.4%	29.2%	19.7%	100%
E = 150 GPa				
34.5%	14.3%	29.9%	21.3%	100%
E = 100 GPa				
33.3%	12.9%	29.8%	24.0%	100%
E = 50 GPa				
48.1%	9.9%	0.0%	42.0%	100%

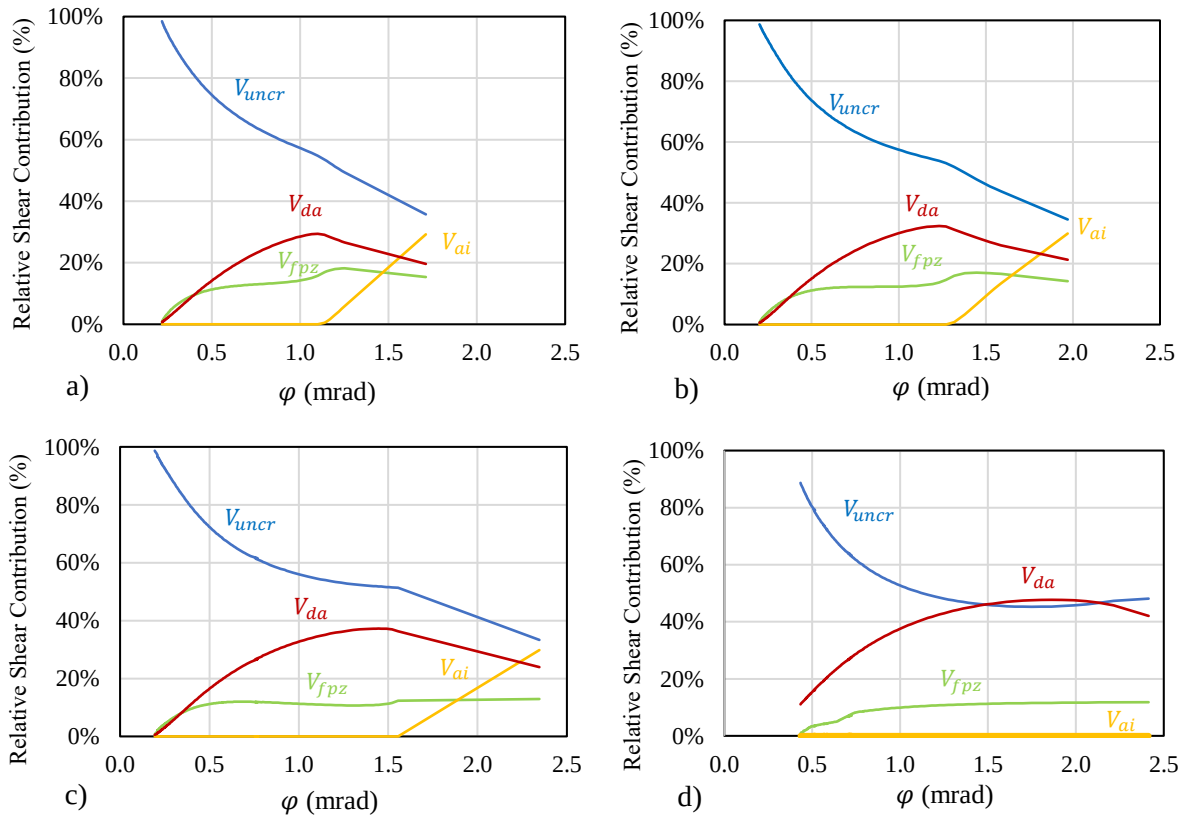

Figure 3-5 The relative shear contribution and crack rotation for various moduli of elasticity: a) E = 200 GPa, b) E = 150 GPa, c) E = 100 GPa, and d) E = 50 GPa.

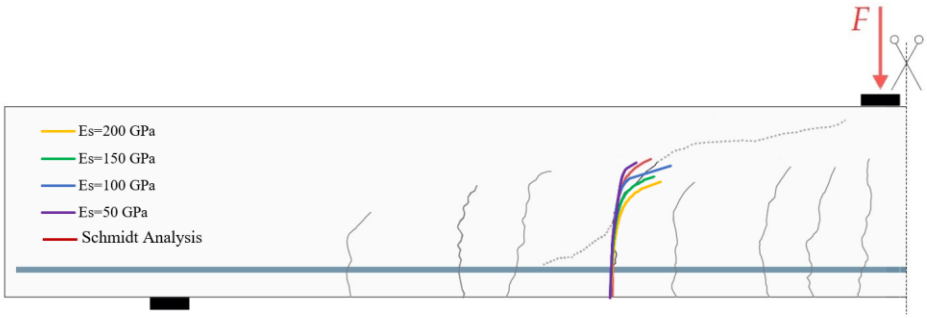

Figure 3-6 The comparison of crack geometry for various moduli of elasticity and Schmidt analysis (Schmidt et al., 2021).

3.4 Dowel Action

In this section, the effect of using FRP reinforcement on dowel action will be investigated. The reduced dowel action associated with FRP reinforcement is introduced according to the results of previous studies. Although the transverse shear strength and stiffness of FRP reinforcing bars is considerably lower than steel bars of the same diameter, dowel action is still largely controlled by the splitting strength of the concrete cover. Unfortunately, there is no consensus regarding this effect, with some researchers suggesting that the effect of bar stiffness can be neglected (e.g., Oller et al., 2015), while others have reported a significant influence. Tottori and Wakui (1993) suggested that the dowel capacity of test specimens reinforced with FRP bars is about 70% of those containing reinforcing steel with the same diameter, corresponding to $(E_f/E_s)^{1/3}$. However, Michaluk et al. (1998) claimed that the effect is directly proportional to elastic modulus and proposed to modify existing equations by the modular ratio of the reinforcement (E_f/E_s). The assumption of a direct correlation between the elastic modulus and dowel capacity is excessively conservative and lacks substantial support, considering that the concrete cover plays a substantial role in determining a significant portion of the dowel capacity. Thus, in this study, the dowel action is modified by the factor $(E_f/E_s)^{1/3}$. One of the benefits of the SCPT is its compatibility with any choice of constitutive models; thus, this assumption can be easily adapted in future works as more accurate data on the contribution of FRP reinforcement to dowel action becomes available.

The modified formulations, based on the work of Reineck (1990) and Yang (2014) adopted by Classen (2020), are given by Equations 3-1:

$$V_{da,0} = 1.64 \cdot b_n \cdot \phi_s \cdot (f_c')^{1/3} (\frac{E_f}{E_s})^{1/3} \quad \text{Eq. 3- 1}$$

$$b_n = b_w - \phi_s \cdot n_s \quad \text{Eq. 3- 2}$$

$$V_{da} = \begin{Bmatrix} \delta_k \leq 0.05mm: & V_{da,0} \cdot \frac{\delta_k}{0.05} \cdot (2 - \frac{\delta_k}{0.05}) \\ \delta_k > 0.05mm: & V_{da,0} \cdot \frac{2.55 - \delta_k}{2.5} \geq 0 \end{Bmatrix} \quad \text{Eq. 3- 3}$$

3.4.1. Results

In this step, the dowel action was modified by the ratio $(E_f/E_s)^{1/3}$, keeping all other parameters constant, giving the results presented in Figure 3-7. The total shear resistance was reduced by 1.5%, 4.7%, and 6.6% for beams with reinforcement elastic moduli of 150, 100, and 50 GPa, respectively. Furthermore, the only mechanism that experiences a significant reduction in comparison with the previous section is dowel action, which is also decreased by lowering the modulus of elasticity. However, in the previous section, it had almost the same amount for all the range of modulus of elasticities (Table 3-4).

Table 3-4 The absolute values of various components at shear failure for different moduli of elasticiy

V_{uncr} (kN)		V_{FPZ} (kN)		V_{ai} (kN)		V_{da} (kN)		Total V (kN)	
E = 150 GPa									
32.73	32.83	13.78	13.56	28.76	28.44	18.37	20.23	93.64	95.06
E = 100 GPa									
27.40	28.13	11.46	10.91	25.66	25.16	16.05	20.18	80.57	84.38
E = 50 GPa									
22.71	23.75	7.07	4.88	3.56	0.00	13.00	20.76	46.34	49.39
Note: The coloured cells are the results from the previous section.									

The slight reduction in dowel action reduced the crack rotation at failure as well as the rotation angle at which aggregate interlock was engaged. Even the beam containing 50 GPa reinforcement exhibited a small contribution from aggregate interlock at failure (Table 3-5).

Table 3-5 The percentage of various components at shear failure for different modulus of elasticities

V_{uncr}	V_{FPZ}	V_{ai}	V_{da}	Total V
E = 150 GPa				
35.0%	14.7%	30.7%	19.6%	100%
E = 100 GPa				
34.0%	14.2%	31.9%	19.9%	100%
E = 50 GPa				
49.0%	15.3%	7.6%	28.1%	100%

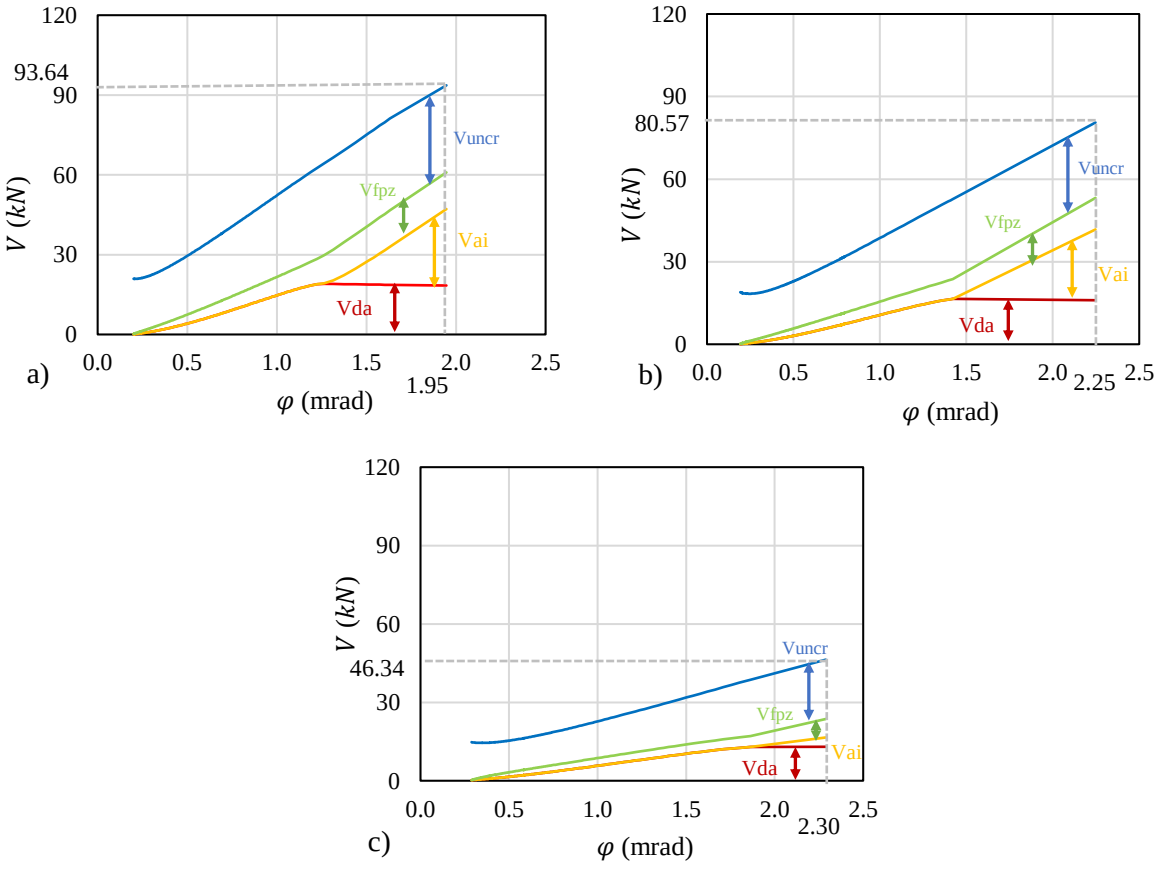

Figure 3-7 The relationship between shear force and crack rotation for various moduli of elasticity with reduced dowel action: a) E = 150 GPa, b) E = 100 GPa, and c) E = 50 GPa.

3.5 Tension Stiffening

In the previous validations, the effect of tension stiffening was neglected. In this section, the reinforcement strain is divided into two sections following the methodology proposed by Bentz (2005) and adopted in Classen (2020) which is illustrated in Figure 3-8. The strain in steel reinforcement at a cracked section is assumed constant along the length of horizontal delamination cracks ($\varepsilon_{s,delam}$), and can be calculated by Equation 3-4. For the regions between cracks where bond is intact, a portion of the tensile force is transferred to the concrete resulting in a lower reinforcement strain ($\varepsilon_{s,ts}$) which is calculated by solving Equation 3-5 (Classen, 2020).

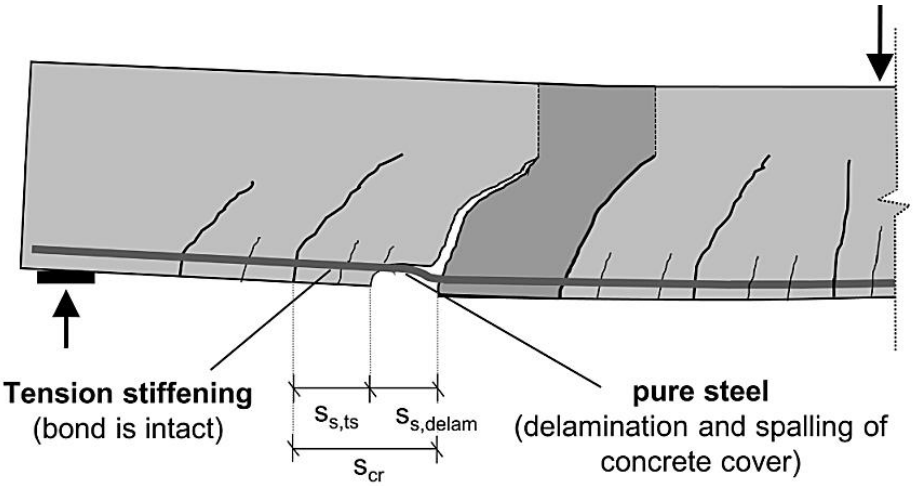

Figure 3-8 Tension stiffening and delamination regions (Classen, 2020).

$$\varepsilon_{s,delam} = \frac{\sigma_s}{E_s} = \frac{F_s}{A_s \cdot E_s} \qquad \text{Eq. 3- 4}$$

$$\sigma_s(\varepsilon_{s,ts}) = \frac{F_s}{A_s} = \varepsilon_{s,ts} \cdot E_s + \frac{f_{ct}}{1 + \sqrt{3.6 \cdot M \cdot \varepsilon_{s,ts}}} \qquad \text{Eq. 3- 5}$$

Where: Eq. 3- 6

$$M = \frac{A_{c,eff}}{\sum d_s \cdot \pi} \qquad \text{Eq. 3- 7}$$

$$A_{c,eff} = h_{c,eff} \cdot b_w \quad \text{Eq. 3- 8}$$

$$h_{c,eff} = min\left(2.5 \cdot d_1; \frac{h - x_0}{3}\right) \quad \text{Eq. 3- 9}$$

Then, the average reinforcement strain in the cracked region will be calculated by Equation 3-10 for a new rotation value as defined in the previous chapter (φ) (Classen, 2020).

$$\varepsilon_s = \frac{\varepsilon_{s,ts} \cdot \left(s_{cr} - s_{cr,delam}\right) + \varepsilon_{s,delam} \cdot s_{cr,delam}}{s_{cr}} \quad \text{Eq. 3- 10}$$

The influence of tension stiffening on shear capacity is frequently neglected for steel-RC members. However, Bischoff and Paixao (2004) demonstrated that tension stiffening is more significant in FRP-RC due to the lower elastic modulus of the reinforcement which makes the contribution of the concrete in tension proportionally larger. They proposed to normalize the post-cracking reinforcement strain by adding a tension stiffening factor (β) to tensile cracking strength of concrete to obtain the average tensile stress in cracked concrete (Bischoff & Paixao, 2004). Thus, it is proposed to modify the tension stiffening model in a similar manner, as presented in Equations 3-11 and 3-12:

$$\sigma_s(\varepsilon_{s,ts}) = \frac{F_s}{A_s} = \varepsilon_{s,ts} \cdot E_s + f_{ct} \cdot \beta \quad \text{Eq. 3- 11}$$

Where the value of β, obtained from Bischoff & Paixao (2004), is:

$$\beta = exp\left[-1100(\varepsilon_m - \varepsilon_{cr})\left(^{E_f}/_{E_s}\right)\right] \quad \text{Eq. 3- 12}$$

Where ε_m is the average reinforcement strain, it should be replaced by ε_s defined in Equation 3-10. Additionally, E_s is considered as 200 GPa for all models.

3.5.1. Results

In this step, by keeping the dowel action effect and all other parameters constant, the tension stiffening effect is added, and the results are presented in Figure 3-9. Based on the comparison

with and without tension stiffening, the results were almost the same, and indicated that the inclusion of tension stiffening does not significantly alter the shear strength outcomes. To further validate these new findings and to account for any potential variations, an alternative approach was also considered. Instead of incorporating the tension stiffening factor β into Equation 3-11, the modular ratio of the reinforcement ($^{E_f}/_{E_s}$) was added in tension stiffening formulations (Eq. 3-13). In both cases, the results are almost the same (Fig. 3-10).

$$\sigma_s(\varepsilon_{s,ts}) = \frac{F_s}{A_s} = \varepsilon_{s,ts} \cdot E_s + \frac{f_{ct}}{1 + \sqrt{3.6 \cdot M \cdot \varepsilon_{s,ts} \cdot (\frac{E_f}{E_s})}} \qquad \text{Eq. 3- 13}$$

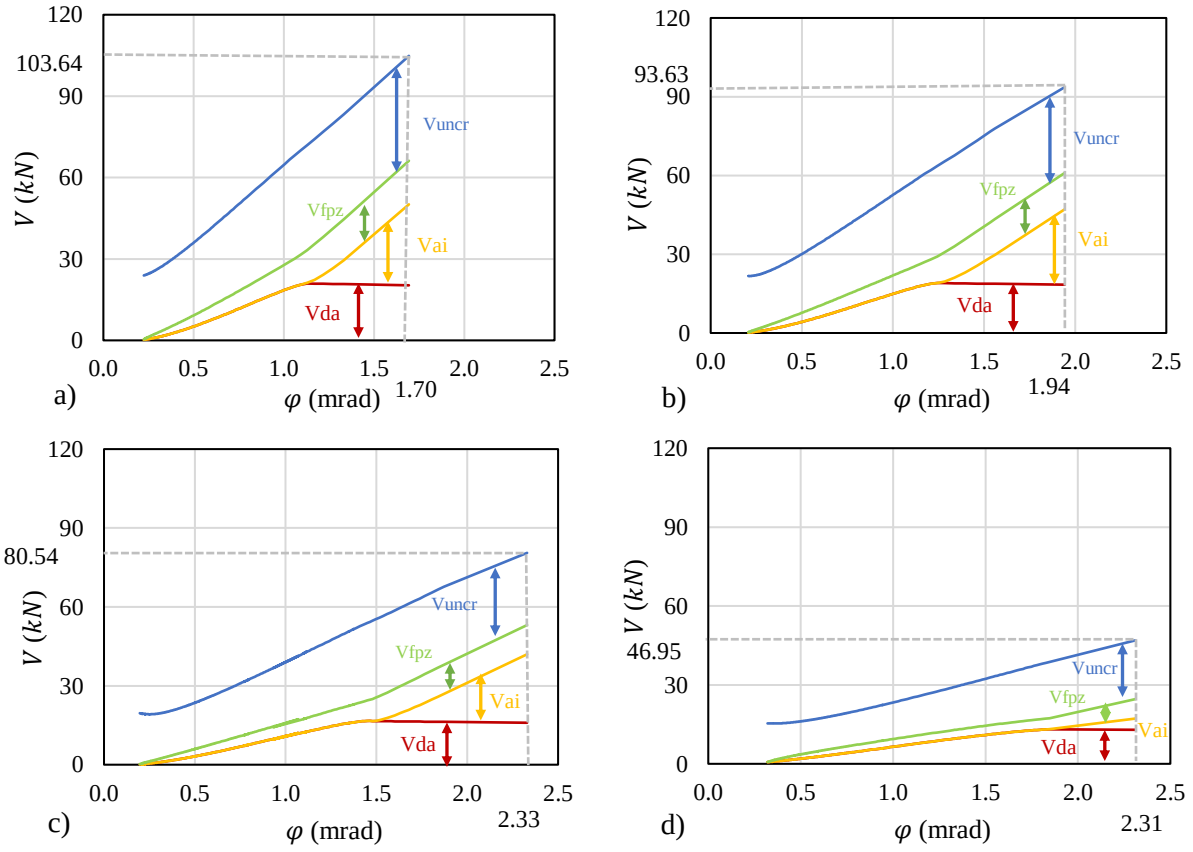

Figure 3-9 The relationship between shear force and crack rotation for various moduli of elasticity by applying β: a) E = 200 GPa, b) E = 150 GPa, c) E = 100 GPa, and d) E = 50 GPa.

Table 3-6 The absolute values of various components at shear failure for different moduli of elasticiy

$V_{uncr}\ (kN)$		$V_{FPZ}\ (kN)$		$V_{ai}\ (kN)$		$V_{da}\ (kN)$		Total $V\ (kN)$	
E = 200 GPa									
37.06	36.97	15.91	15.93	30.36	30.23	20.31	20.34	103.64	103.47
E = 150 GPa									
32.66	32.73	13.85	13.78	28.75	28.76	18.37	18.37	93.63	93.64
E = 100 GPa									
27.44	27.40	11.11	11.46	26.06	25.66	15.93	16.05	80.54	80.57
E = 50 GPa									
22.34	22.71	7.40	7.07	4.26	3.56	12.95	13.00	46.95	46.34
Note: The coloured cells are the results from the previous section.									

Table 3-7 The percentage of various components at shear failure for different modulus of elasticities

V_{uncr}	V_{FPZ}	V_{ai}	V_{da}	Total V
E = 200 GPa				
36.9%	15.3%	28.4%	19.4%	100%
E = 150 GPa				
34.9%	14.8%	30.7%	19.6%	100%
E = 100 GPa				
34.1%	13.8%	32.3%	19.8%	100%
E = 50 GPa				
47.6%	15.7%	9.1%	27.6%	100%

The results of this validation process provided valuable insights into the role of tension stiffening in FRP-RC structures. While it may not significantly impact shear strength for the range of parameters considered, the presented approach enables a better understanding of the relative importance of these contributing factors associated with FRP-RC members. The tension stiffening phenomenon is additionally impacted by the bonding properties of the reinforcement, which differ depending on the surface treatment applied to the FRP reinforcement. Nevertheless, as our findings indicated a negligible influence of tension stiffening, further exploration into these effects was not pursued.

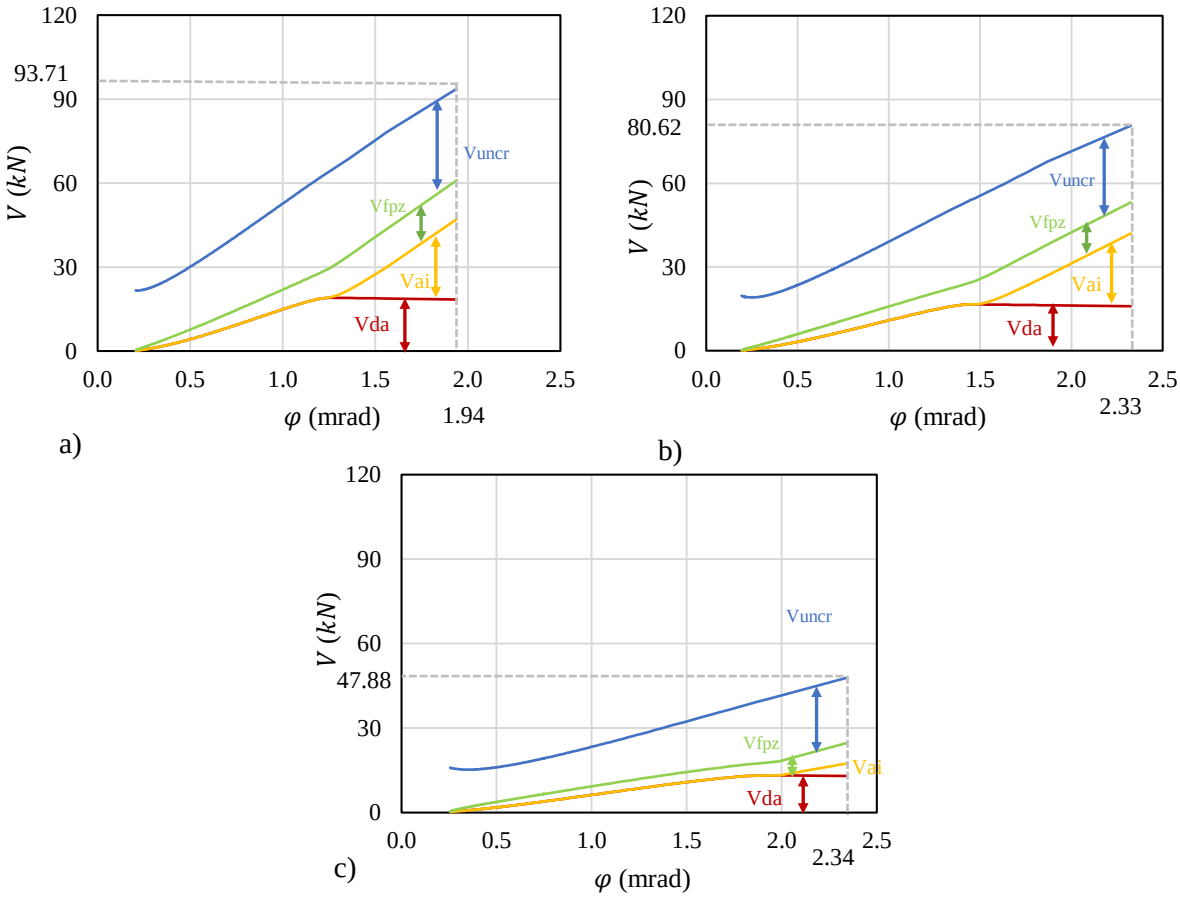

Figure 3-10 The relationship between shear force and crack rotation for various moduli of elasticity by applying the ratio of (E_f/E_s)*: a) E = 150 GPa, B) E = 100 GPa, and C) E = 50 GPa.*

3.5 Summary

This chapter focused on the behaviour of concrete beams reinforced with FRP materials, with a particular emphasis on the effects of varying modulus of elasticity, dowel action, and tension stiffening based on the SCPT methodology.

First, the results for a steel-RC beam were independently obtained and compared with Schmidt et al.'s experimental results to analyze the shear behaviour of a beam without shear reinforcement. The predicted response was almost the same as the previous study, and the small deviation between this analysis and Schmidt et al.'s results may be attributed to differences in assumptions about

crack propagation, distance between crack steps, and various initial parameters. Overall, this validation exercise confirms proper implementation of the SCPT algorithm.

Second, the different modulus of elasticity values in FRP reinforcement were chosen to investigate their impact on the shear failure. The aim was to gain a comprehensive understanding of the factors influencing shear strength in FRP-RC members which showed that the modulus of elasticity has a significant impact on shear capacity. Lowering the modulus of elasticity in FRP leads to decreased shear capacity, and the relative contribution of dowel action remains approximately constant for moderate modulus values but increases for very low modulus values. Aggregate interlock's role in shear capacity is also significantly influenced by reinforcement stiffness.

Third, the impact of dowel action by applying the elastic modulus ratio (E_f/E_s) is addressed. The results of this investigation show that modifying dowel action led to a reduction in total shear resistance, with greater reductions associated with lower modulus of elasticity for the reinforcement. Specifically, beams with reinforcement elastic moduli of 150, 100, and 50 GPa experienced reductions of 1.5%, 4.7%, and 6.6% in total shear resistance, respectively. The decrease in dowel action resulted in reduced crack rotation at failure and a lower rotation angle for engagement of aggregate interlock. Even in the case of beams containing 50 GPa reinforcement, there was a slight contribution from aggregate interlock at failure.

Finally, the influence of tension stiffening was examined, and the average reinforcement strain within the cracked area was considered, even in regions where there is no bond between the reinforcement and concrete. An adjustment factor (β) is proposed to account for tension stiffening's influence on shear capacity, although it was found that incorporating tension stiffening does not

significantly affect shear strength. An alternative adjustment using the modular ratio (E_f/E_s) was also considered; however, the results were identical.

Therefore, with the inclusion of these additional factors and the adaptation of the code for FRP-RC members, the upcoming chapter will focus on validating various experimental analyses of FRP-RC structures using the new theory, SCPT.

Chapter 4

SCPT Model Validation

4.1 Introduction

The objective of this chapter is to validate the SCPT model against experimental findings involving FRP-RC members reported in available literature. This comparative analysis serves to establish the accuracy and reliability of the SCPT model within the context of FRP-RC applications.

Initially, 20 experimental tests were chosen, as shown in Table 4-1, followed by a comprehensive comparison of their results with the SCPT predictions. Furthermore, the shear strength of these experimental beams is compared with predictions obtained through the shear design equations outlined in ACI 440.11-22 (ACI 440.11-22, 2022), CSA S806-12 (CSA S806-12, 2012), and CSA S6-19 (CSA S6:19, 2019) standards (Table 4-1 and Fig. 4-1). This examination facilitates an insightful validation of the SCPT model's performance against different kinds of reinforcing materials.

Table 4-1 Summary of validation results

Row	Description	L mm	a mm	h mm	d mm	λ_{cs} -	b mm	$f_{cm,cyl}$ MPa	f_{ct} MPa	E_c MPa	E_f MPa	f_u MPa	d_{ag} mm	ρ_l -	d_s mm	n -	A_s mm^2	ACI 440 (KN)	CSA S806 (KN)	CSA S6 (KN)	SCPT (KN) A	Experimental (KN) B	Ratio (A/B)
	(1)	(2)	(3)	(4)	(5)	(6)	(7)	(8)	(9)	(10)	(11)	(12)	(13)	(14)	(15)	(16)	(17)	(18)	(19)	(20)	(21)	(22)	(23)
1	Alam (C-500)	3540	1150	500	460	1.5	250	34.5	3.29	26432	144000*	1899*	20	0.00449	12.7	4	516	47.14	94.11	98.88	84.37	74.10	**1.14**
2	Alam (G-650)	4040	1460	650	584		300	37	3.41	27372	48200*	751*		0.00913	15.875	8	1600	56.83	115.25	144.60	91.16	103.7	**0.88**
3	Alam (G-800)		1835	800	734			41.8	3.62	29094				0.00908		10	2000	67.81	131.54	177.46	115.48	129.4	**0.89**
4	Noel (G1)	4500	1750	300	270	5.5	600	58.1	3.90	34301	55900	784	13	0.00733	16	6	1187.4	79.92	103.86	196.06	75.50	83.1	**0.91**
5	Noel (G2)													0.01466		12	2374.8	99.68	127.65	196.06	100.67	109.9	**0.92**
6	El-Sayed (CN-2)	3250	1000	400	326	2.07	250	44.6	3.74	30052	134000	986	20	0.01247	12.7	8	1016	60.16	102.56	87.11	87.49	104.0	**0.84**
7	El-Sayed (CN-1.7)							43.6	3.00	29714				0.0172		11	1397	68.20	112.46	86.13	89.73	124.5	**0.72**
8	El-Sayed (GN-1.7)										42000	754		0.0171	15.9	7	1386	41.49	78.76	86.13	60.44	77.5	**0.78**
9	Issa (5-10N5)	2440	960.5	200	170	4.65	300	35.9	3.36	26962	53000*	1070	20	0.00804	10*	5	410	20.88	30.17	54.86	23.89	29.3	**0.82**
10	Issa (5-13N5)										51000*	1050		0.01343	13*		685	25.85	34.74	54.86	31.89	38.7	**0.82**
11	Bentz (M20-0)	4000	1525	500	405	2.77	450	35	3.31	26622	37000	397	10	0.02362	25.4	8	4304	89.21	142.29	147.78	121.59	138.0	**0.88**
12	Bentz (M05-0)				438	2.48								0.00546		2	1076	65.61	100.20	155.54	70.09	86.0	**0.81**
13	Yost (4FRP)	2284	914	286	225	3.06	279	36.3	4.73	39900	40336	689.5	15	0.0181	19	4	1136	27.62	51.58	64.19	40.26	45.3	**0.89**
14	Yost (5FRP)				224	3.08	254							0.0204	22	3	1161	26.37	48.30	58.44	42.74	45.1	**0.95**
15	Guadagnini (GB43)	2300	750	250	223	2.3	150	42.8	4.38	29440	45000	1000	20	0.0128	14	3	429	16.49	30.03	37.73	28.35	27.2	**1.04**
16	Guadagnini (GB44)	1800	500			1.2												16.49	40.63	37.73	32.88	44.7	**0.74**
17	Kim (C-3.5)	3200	747.25	250	213.5	2.5	150	30	3.07	24648	147900*	2023*	9.5	0.0079	13	2	253.4	19.47	30.69	28.49	25.88	29.0	**0.89**
18	Kim (G-3.5)										49100*	940.6*						11.97	22.07	28.49	16.88	18.8	**0.99**
19	Razaqpur (BR1)	2262	600.75	250	225	1.67	200	40.5	3.56	28638	145000*	2550*	20	0.0025	8	2.25	112.50	18.90	38.45	49.30	32.27	36.11	**0.89**
20	Razaqpur (BR4)		1013			3.50								0.0050		4.50	225	24.19	36.36	49.30	32.17	38.45	**0.84**

Note 1: The yellow highlighted cells were not reported, and some of them are either assumed or calculated.

Note 2: The stars represent the values provided by the manufacturer when measured properties were not reported.

Note 3: The $\boldsymbol{\lambda_{cs}}$ represents the location of major crack from the support, taken as $\left(\frac{a-d}{d}\right)$, as discussed later in Figure 4-27.

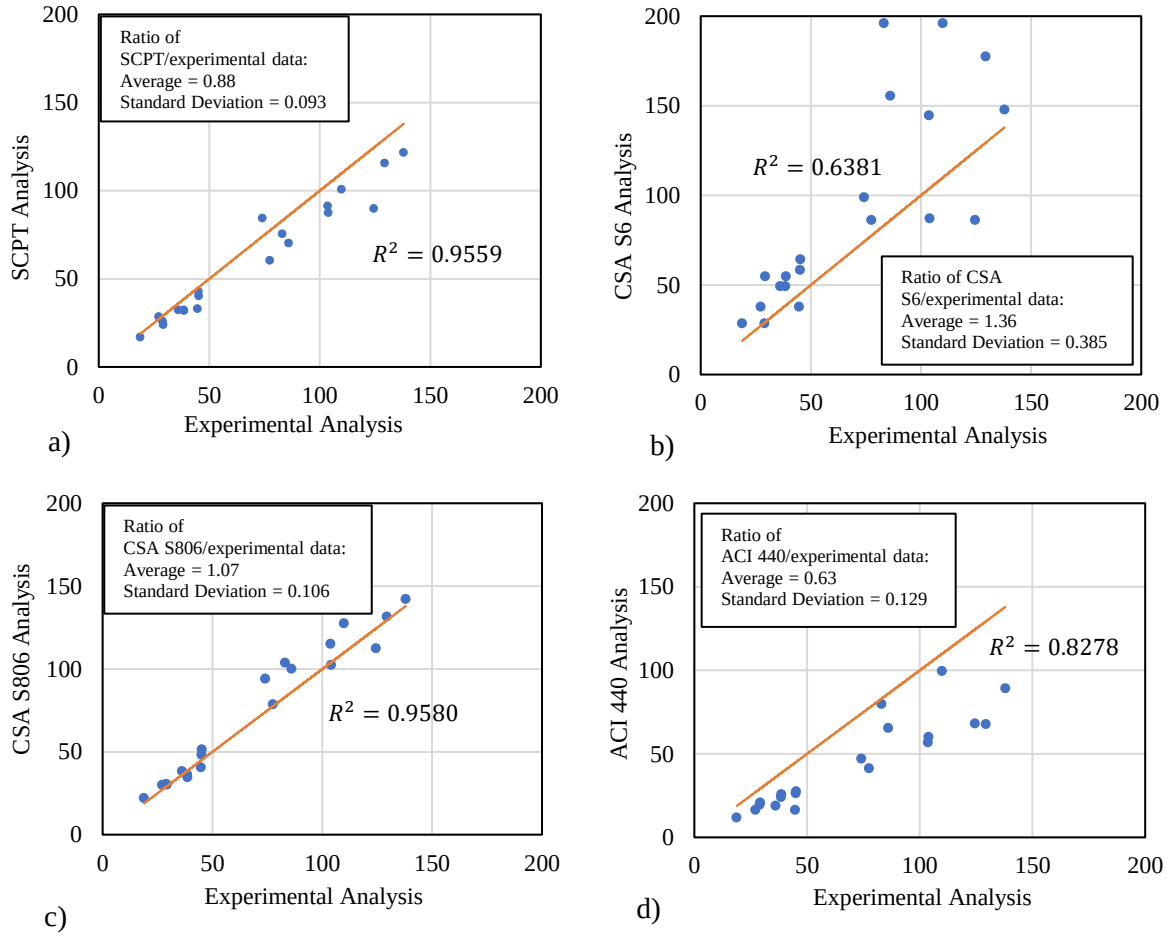

Figure 4-1 The variation of experimental analysis with a) SCPT, b) CSA S6, c) CSA S806, and d) ACI440 analysis.

4.2 FRP Beams Without Shear Reinforcement

Numerous experimental studies in the literature have investigated the impact of FRP on the shear strength of FRP-RC beams over the years. For validation purposes in this report, nine specific studies have been selected.

4.2.1. Experimental Investigation by Alam et al. (2013)

One of their research objectives was to analyze the performance of RC beams reinforced with FRP bars by differing the beam depth and reinforcement type.

Table 4-2 Specimen specifications (Alam & Hussein, 2013)

Specimen #1 (C-500)							
L (mm)	**a (mm)**	**d (mm)**	**b (mm)**	**h (mm)**	d_s **(mm)**	**n**	A_s **(mm²)**
3540	1150	460	250	500	12.7	4	516
f_{cm} **(N/mm²)**	f_{ct} **(N/mm²)**	E_c **(N/mm²)**	E_f **(N/mm²)**	f_u **(N/mm²)**	λ_{cs}	ρ_l	d_{ag} **(mm)**
34.5	3.29	26432	144000	1899	1.5	0.00449	20
Specimen #2 (G-650)							
L (mm)	**a (mm)**	**d (mm)**	**b (mm)**	**h (mm)**	d_s **(mm)**	**n**	A_s **(mm²)**
4040	1460	584	300	650	15.875	8	1600
f_{cm} **(N/mm²)**	f_{ct} **(N/mm²)**	E_c **(N/mm²)**	E_f **(N/mm²)**	f_u **(N/mm²)**	λ_{cs}	ρ_l	d_{ag} **(mm)**
37	3.41	27372	48200	751	1.5	0.00913	20
Specimen #3 (G-800)							
L (mm)	**a (mm)**	**d (mm)**	**b (mm)**	**h (mm)**	d_s **(mm)**	**n**	A_s **(mm²)**
4040	1835	734	300	800	15.875	10	2000
f_{cm} **(N/mm²)**	f_{ct} **(N/mm²)**	E_c **(N/mm²)**	E_f **(N/mm²)**	f_u **(N/mm²)**	λ_{cs}	ρ_l	d_{ag} **(mm)**
41.8	3.62	29094	48200	751	1.5	0.00908	20

Note: The splitting tensile strength (f_{ct}) and concrete modulus of elasticity (E_c) is calculated based on ACI318-19 ($f_{ct} = 0.56\sqrt{f_{cm}}$, and $E_c = 4500\sqrt{f_c'}$).

They conducted 12 large-scale beam tests on various types of steel-RC and FRP-RC beams, utilizing both glass FRP and carbon FRP, all without shear reinforcement. Selected material and geometric properties for beams selected for this validation are presented in Table 4-2, and the test setup is shown in Figure 4-2.

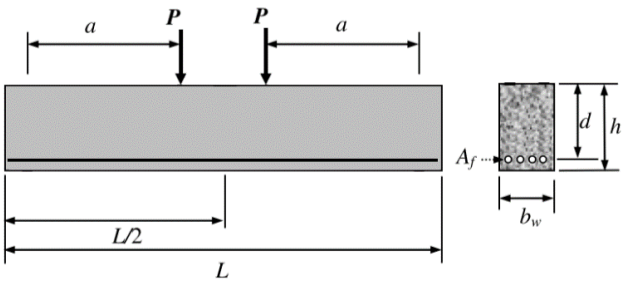

Figure 4-2 Test setup schematic (Alam & Hussein, 2013)

4.2.1.1. Results

Considering the specifications presented in the previous section as inputs, the SCPT model was used to predict crack propagation and the corresponding forces throughout the entire loading process, from initiation to failure. While Figure 4-3 displays SCPT predictions for four different mechanisms from the initial point of loading to the point of failure, the comparison between the SCPT model and the research under review can be based solely on the shear failure point.

According to the findings of Alam et al., the shear failure load for C-500, G-650 and G-800 was determined to be 74.1, 103.7, and 129.4 kN, respectively. However, the SCPT analysis yielded a value of 84.37, 91.16, and 115.48 kN, respectively, for the shear failure (Table 4-1). The results show that the SCPT approach was conservative for G-650 and G-800 specimens, with shear failure predictions almost 12% and 11% lower than the experimental results.

One of the reasons for these differences can be the initial inputs for the experimental data, which include nominal cross-sectional area, tensile strength, and modulus of elasticity of the FRP bars, that were specified by the manufacturer (not measured), therefore conservative. Furthermore, the authors did not mention the splitting tensile strength and concrete modulus of elasticity in the article; therefore, they were calculated based on ACI 318-19 code for SCPT analysis.

It can be concluded that the contribution of dowel action is related to the longitudinal reinforcement ratio, not the amount of rebars. By comparing sections b and d (Figure 4-3), it can be observed that the contribution of dowel action was reduced with a decrease in the longitudinal reinforcement ratio, even though the number of rebars had been increased.

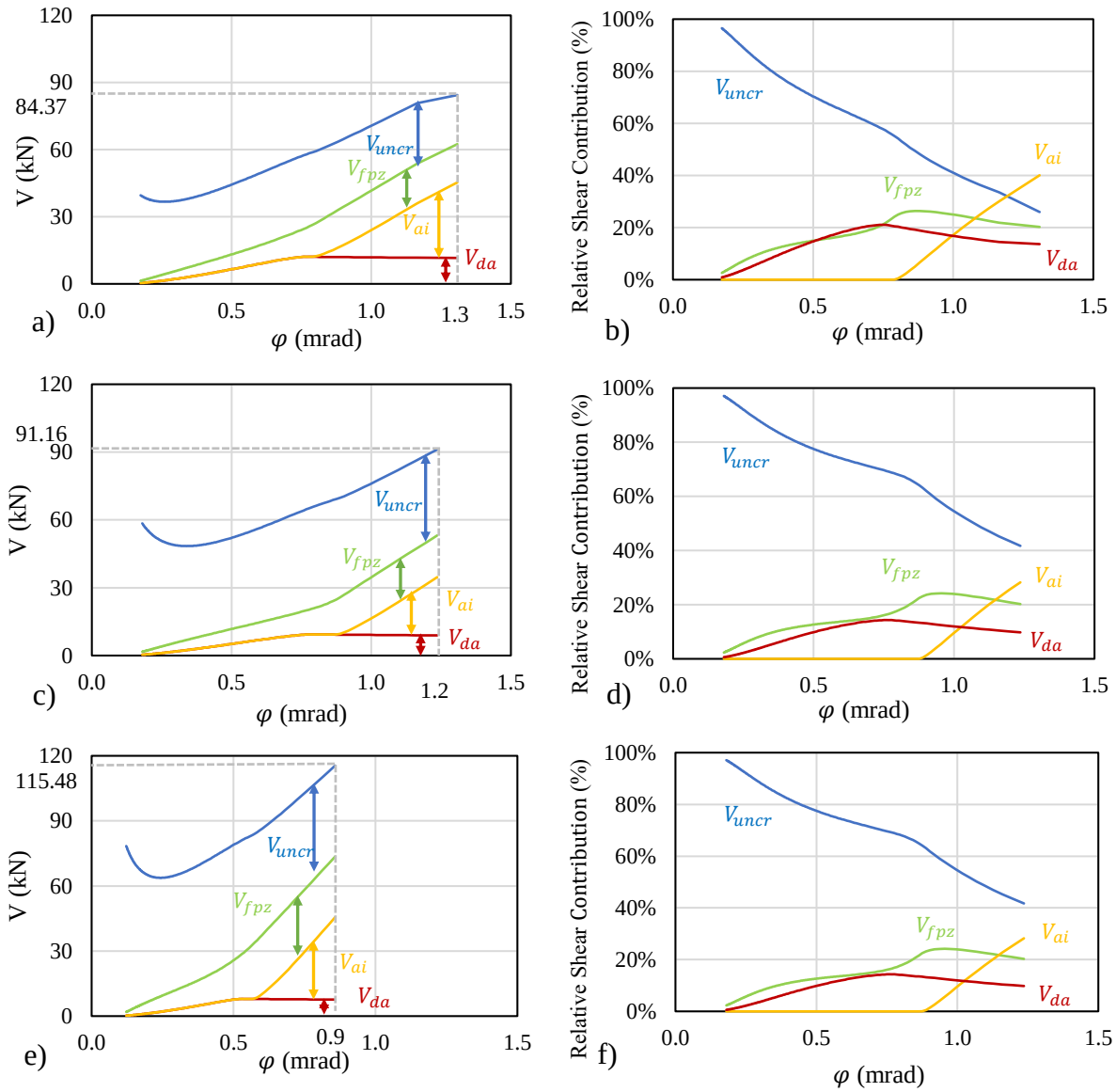

Figure 4-3 The relationship between shear crack rotation and: a) Shear force for C-500, b) Relative shear contribution for C-500, c) Shear force for G-650, d) Relative shear contribution for G-650, e) Shear force for G-800, f) Relative shear contribution for G-800, based on SCPT analysis.

4.2.2. Experimental Investigation by Noel (2013)

The main objective of Noel's research was to examine the performance of an all-FRP reinforcement system, encompassing both glass FRP (GFRP) and carbon FRP (CFRP), in slab bridges across three various limit states: serviceability, ultimate, and fatigue. He tested 57 full-scale slab strips to investigate the impact of different parameters, including reinforcement type, among others. This investigation encompassed variations involving both with and without shear

reinforcement, subjected to both monotonic and fatigue loading. Here, two GFRP slab specimens without shear reinforcement are selected for validation under static loading conditions. The specifications of the selected specimens are provided in Table 4-3. Besides, the test setup is shown in Figure 4-4.

Table 4-3 Specimen specifications (Noël, 2013)

Specimen #1 (G1)							
L (mm)	**a (mm)**	**d (mm)**	**b (mm)**	**h (mm)**	d_s **(mm)**	**n**	A_s **(mm²)**
4500	1750	270	600	300	16	6	197.9
f_{cm} **(N/mm²)**	f_{ct} **(N/mm²)**	E_c **(N/mm²)**	E_f **(N/mm²)**	f_u **(N/mm²)**	λ_{cs}	ρ_l	d_{ag} **(mm)**
58.1	3.9	34301	55900	683	5.5	0.00733	13
Specimen #2 (G2)							
L (mm)	**a (mm)**	**d (mm)**	**b (mm)**	**h (mm)**	d_s **(mm)**	**n**	A_s **(mm²)**
4500	1750	270	600	300	16	12	2374.8
f_{cm} **(N/mm²)**	f_{ct} **(N/mm²)**	E_c **(N/mm²)**	E_f **(N/mm²)**	f_u **(N/mm²)**	λ_{cs}	ρ_l	d_{ag} **(mm)**
58.1	3.9	34301	55900	683	5.5	0.01466	13

Note: The concrete modulus of elasticity (E_c) is calculated based on ACI318-19 ($E_c = 4500\sqrt{f_c'}$).

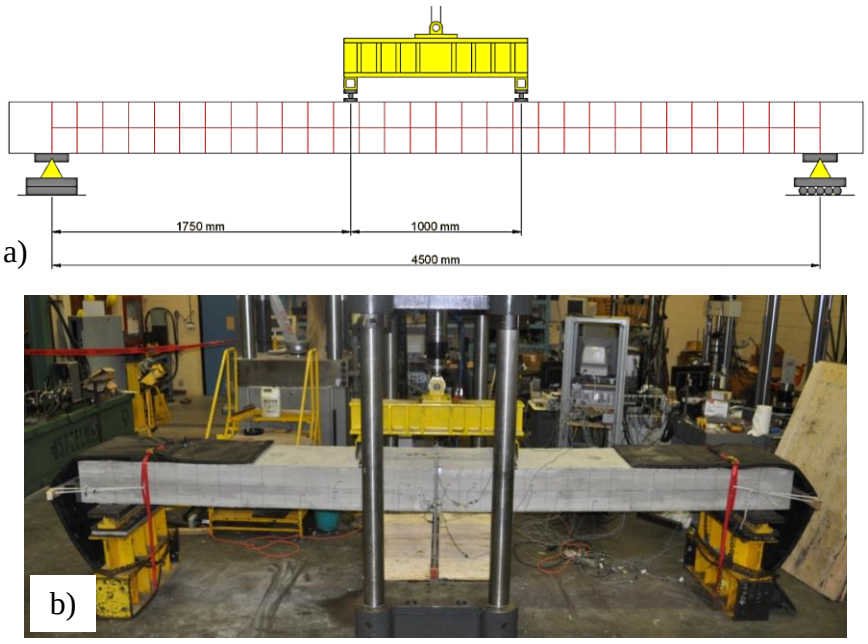

Figure 4-4 a) Test setup schematic, b) Full-scale test setup (Noël, 2013)

4.2.2.1. Results

Considering all the specifications detailed in the preceding section as input parameters, the outcomes are depicted in Figure 4-5. In accordance with Noel's findings, the experimental shear resistance for the designated specimens was measured at 83.1 and 109.9 kN, respectively. Nonetheless, employing SCPT analysis, the calculated shear failure stands at 75.50 and 100.67 kN, respectively, representing a conservative estimate with an approximate 9 and 8% difference (Table 4-1).

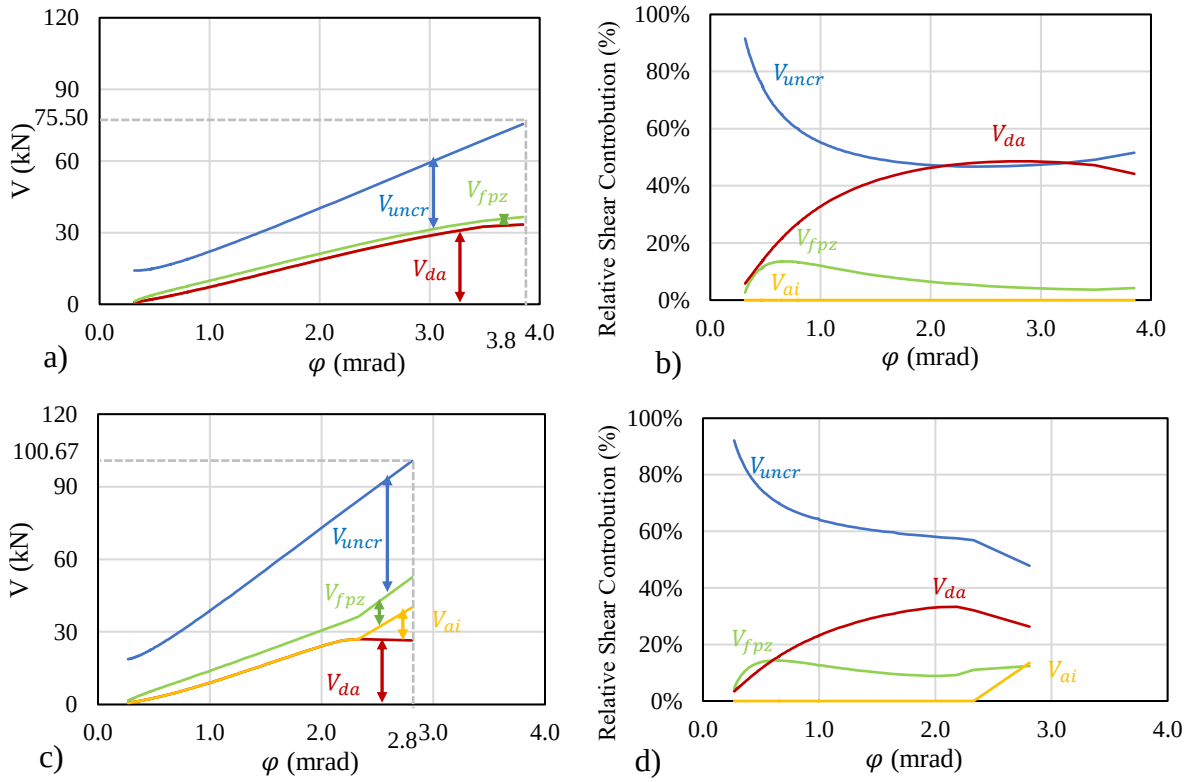

Figure 4-5 The relationshipt between shear crack rotation and: a) Shear force for G1, b) Relative shear contribution for G1, c) Shear force for G2, d) Relative shear contribution for G2, based on SCPT analysis.

One of the noticeable reasons for these differences are based on one assumption related to the crack spacing which can be varied based on the previous models presented by Cladera, Collins, Reineck et al., and Tung & Tue (Cladera et al., 2017; Collins, Bentz, & Sherwood, 2008; Reineck, 1991; Tung & Tue, 2016). In this research, the spacing of primary cracks is assumed to be 0.5d

(this parameter is examined for one of the experimental analyses in section 4.3). The other one is the value of the concrete modulus of elasticity which was not mentioned in Noel's thesis, and it has been calculated based on ACI 318-19 code for SCPT analysis.

It can be concluded that the shear resistance will increase by increasing the longitudinal reinforcement ratio (ρ). However, the crack rotation (φ) and crack width in the longitudinal reinforcement layer (W_{reinf}) were decreased (Fig. 4-5 and 4-6). Interestingly, the relative contribution of dowel action is reduced significantly, and it shows that the most part of the shear failure was carried by the uncracked concrete compression zone (Fig. 4-5).

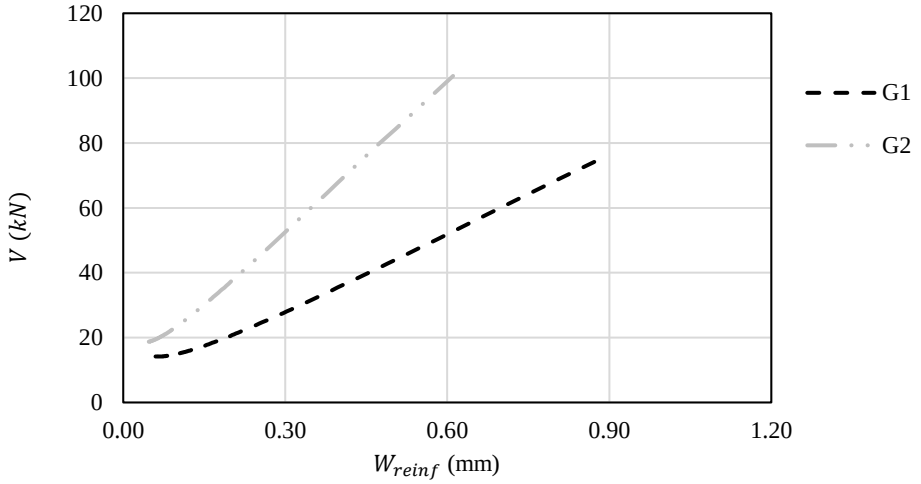

Figure 4-6 The relationshipt between shear force and the crack width in the longitudinal reinforcement layer, based on SCPT analysis.

4.2.3. Experimental Investigation by El-Sayed et al. (2006)

In the studies conducted by El-Sayed et al., their research focused on concrete slender beams that were reinforced with various types of FRPs, such as Carbon FRP (CFRP) and Glass FRP (GFRP). The primary objective was to investigate the influence of varying reinforcement ratios and modulus of elasticity on shear strength. The experimental setup involved the testing of nine large-scale RC beams without shear reinforcement. Among these, three beams were reinforced with CFRP, another three with GFRP, and the remaining three with conventional steel rebars. Among

these tested specimens, the detailed specifications of the selected specimen and the schematic of the testing setup for validation purposes can be found in Table 4-4 and Figure 4-7, respectively.

Table 4-4 Specimen Specimen specifications (El-Sayed et al., 2006)

Specimen #1 (CN-2)							
L (mm)	**a (mm)**	**d (mm)**	**b (mm)**	**h (mm)**	d_s **(mm)**	**n**	A_s **(mm^2)**
3250	1000	326	250	400	12.7	8	1016
f_{cm} **(N/mm^2)**	f_{ct} **(N/mm^2)**	E_c **(N/mm^2)**	E_f **(N/mm^2)**	f_u **(N/mm^2)**	λ_{cs}	ρ_l	d_{ag} **(mm)**
44.6	3.74	30052	134000	986	2.1	0.01247	13

Note 2: The splitting tensile strength (f_{ct}) and concrete modulus of elasticity (E_c) is calculated based on ACI318-19 (f_{ct} = 0.56$\sqrt{f_{cm}}$= 3.74, and E_c = 4500$\sqrt{f_c'}$= 30052).

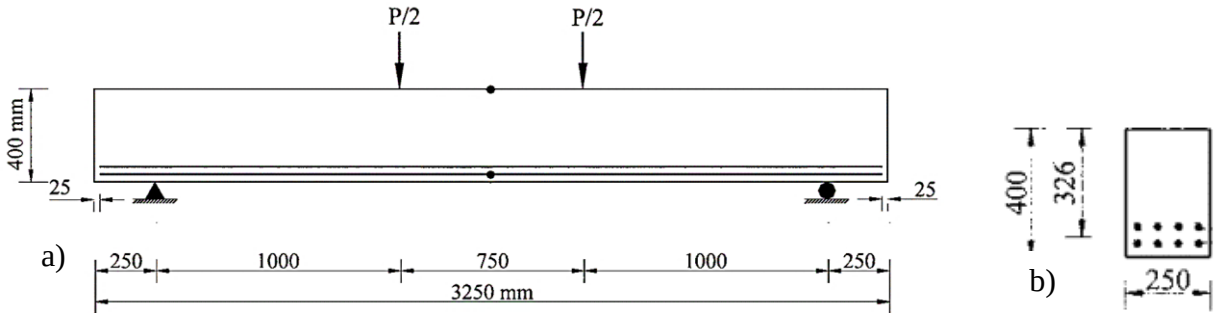

Figure 4-7 a) Test setup schematic, b) Cross-Section (El-Sayed et al., 2006)

In another article, El-Sayed et al. conducted another experimental analysis involving six beams including three high-strength concrete (HSC) slender FRP-RC beams, while the others were made of normal-strength concrete. They explained that HSC, as defined by the ACI code, exhibits a distinctive characteristic where cracks tend to propagate through the aggregates rather than surrounding, mainly due to the higher strength of the cement paste compared to the aggregates. This phenomenon results in reduced aggregate interlock, leading to a decrease in the shear force carried by the concrete (V_c). Consequently, the contribution of dowel forces increases, along with highly concentrated bond stresses, which collectively contribute to higher bond-splitting stresses and a propensity for brittle shear failure.

According to the ACI code, El-Sayed et al. asserted that the contribution of concrete to shear strength (V_c) can be influenced by five variables, including concrete tensile strength (f_{ct}), the longitudinal reinforcement ratio (ρ_l), shear span-to-depth ratio ($^{a}/_{d}$ or $^{M}/_{Vd}$), the axial force, and depth of the member to account for size effect. Furthermore, they highlighted the relatively low modulus of elasticity of FRP bars as another significant parameter that can be considered in addition to these five variables, which also can be combined with longitudinal reinforcement ratio. Hence, they investigated to examine how varying the longitudinal reinforcement ratio and modulus of elasticity impact on shear strength.

In this study, one CFRP and one GFRP-RC specimens have been selected for verification. Detailed specifications of these two specimens can be found in Table 4-5 (with the same schematic presented in Figure 4-7).

Table 4-5 Specimen specifications (El-Sayed et al., 2006)

Specimen #2 (CN-1.7)							
L (mm)	**a (mm)**	**d (mm)**	**b (mm)**	**h (mm)**	d_s **(mm)**	**n**	A_s **(mm²)**
3250	1000	326	250	400	12.7	11	1397
f_{cm} **(N/mm²)**	f_{ct} **(N/mm²)**	E_c **(N/mm²)**	E_f **(N/mm²)**	f_u **(N/mm²)**	λ_{cs}	ρ_l	d_{ag} **(mm)**
43.6	3	29714	134000	986	2.1	0.0172	20
Specimen #3 (GN-1.7)							
L (mm)	**a (mm)**	**d (mm)**	**b (mm)**	**h (mm)**	d_s **(mm)**	**n**	A_s **(mm²)**
3250	1000	326	250	400	15.9	7	1386
f_{cm} **(N/mm²)**	f_{ct} **(N/mm²)**	E_c **(N/mm²)**	E_f **(N/mm²)**	f_u **(N/mm²)**	λ_{cs}	ρ_l	d_{ag} **(mm)**
43.6	3	29714	42000	754	2.1	0.0171	20

Note: The maximum aggregate diameter is assumed 20 mm.

4.2.3.1. Results

Considering all the specifications outlined in the previous section as input variables, the results for all three selected specimens are illustrated in Figure 4-9. Based on El-Sayed's research, the measured shear resistance for the specified test samples (CN-2, CN-1.7, and GN-1.7) was determined to be 104.0, 124.5, and 77.5 kN, respectively. However, when applying SCPT analysis, the predicted shear failure values were 87.49, 89.73, and 60.44 kN, respectively, indicating a conservative estimate with approximately 15-30% disparity (Table 4-1).

One of the possible reasons for these discrepancies is lack of information in some data in the experimental analysis including maximum aggregate size, splitting tensile strength, concrete modulus of elasticity, and crack spacing, all of which are assumed in the SCPT analysis (Table 4-4 and 4-5). These are examined in further detail in a subsequent part of this thesis.

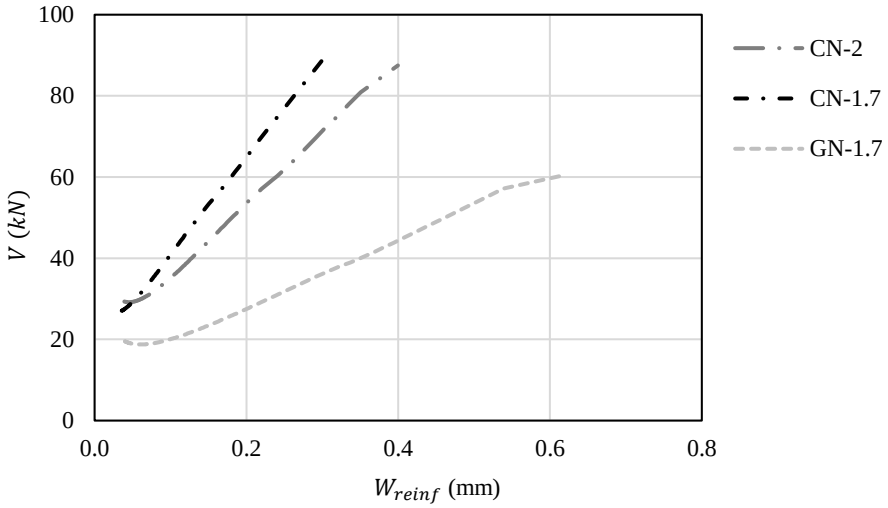

Figure 4-8 The relationship between shear force and the crack width in the longitudinal reinforcement layer, based on SCPT analysis.

By carefully observing the results between CN-2 and CN-1.7, it can be concluded that by increasing the amount of reinforcement (including rebar diameter, rebar numbers, and longitudinal reinforcement ratios), the shear failure load increased, and crack width decreased (despite decreasing the splitting tensile strength) (Fig. 4-8 and 4-9).

Alternatively, when examining the results for CN-1.4 and GN-1.4, it can be inferred that shear failure can be notably reduced by altering the type of FRP (from carbon to glass), i.e. by decreasing the modulus of elasticity. This also resulted in wider cracks by also having the higher crack rotation, highlighting that the primary source of shear capacity lies within the aggregate interlock (Fig. 4-8 and 4-9).

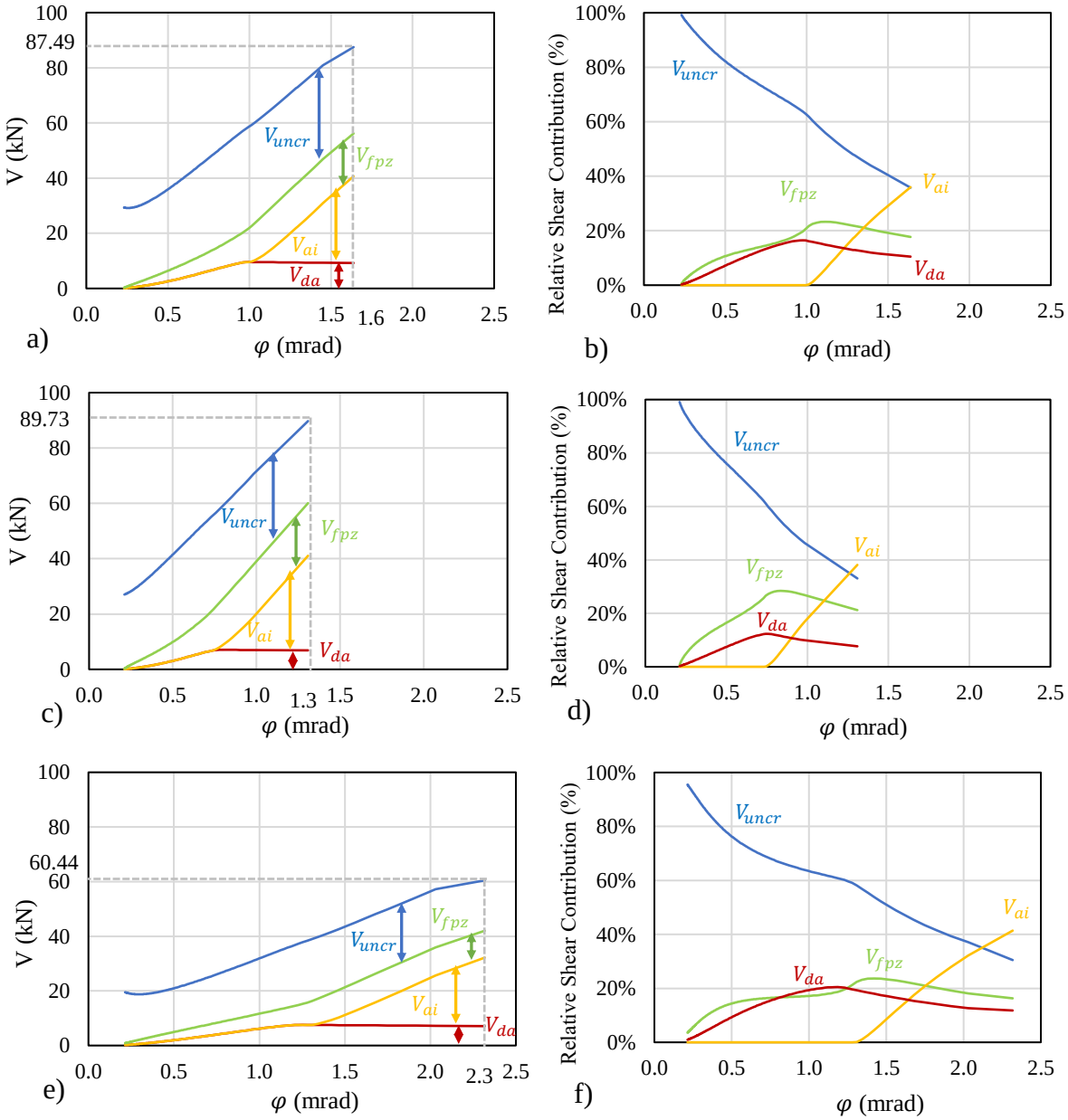

Figure 4-9 The relationship between shear crack rotation and: a) Shear force for CN-2, b) Relative shear contribution for CN-2, c) Shear force for CN-1.7, d) Relative shear contribution for CN-1.7, e) Shear force for GN-1.7, f) Relative shear contribution for GN-1.7, based on SCPT analysis.

4.2.4. Experimental Investigation by Issa et al. (2016)

In 2016, a group of scholars (Issa et al.) conducted a study to explore the impact of various parameters, including shear span-to-depth (a/d) ratios, on the shear strength of RC beams. These beams were reinforced longitudinally with basalt FRP (BFRP). Half of these beams were considered as non-shear-reinforced (NSR), while the remaining half were designed as shear reinforced (SR). To validate the present research, two NSR specimens were chosen for comparison. Their specifications and the schematic test setup are presented in Table 4-6 and Figure 4-10, respectively.

Table 4-6 Specimen specifications (Issa et al., 2016)

Specimen #1 (5-10N5)							
L (mm)	**a (mm)**	**d (mm)**	**b (mm)**	**h (mm)**	d_s **(mm)**	**n**	A_s **(mm²)**
2440	960.5	170	300	200	10	5	410
f_{cm} **(N/mm²)**	f_{ct} **(N/mm²)**	E_c **(N/mm²)**	E_f **(N/mm²)**	f_u **(N/mm²)**	λ_{cs}	ρ_l	d_{ag} **(mm)**
35.9	3.36	26962	53000	1070	4.65	0.00804	20
Specimen #1 (5-13N5)							
L (mm)	**a (mm)**	**d (mm)**	**b (mm)**	**h (mm)**	d_s **(mm)**	**n**	A_s **(mm²)**
2440	960.5	170	300	200	13	5	685
f_{cm} **(N/mm²)**	f_{ct} **(N/mm²)**	E_c **(N/mm²)**	E_f **(N/mm²)**	f_u **(N/mm²)**	λ_{cs}	ρ_l	d_{ag} **(mm)**
35.9	3.36	26962	51000	1050	4.65	0.01343	20

Note1: The maximum aggregate size is assumed 20 mm.

Note 2: The splitting tensile strength (f_{ct}) and concrete modulus of elasticity (E_c) is calculated based on ACI318-19 (f_{ct} = $0.56\sqrt{f_{cm}}$= 3.36, and E_c = $4500\sqrt{f_c'}$= 26962).

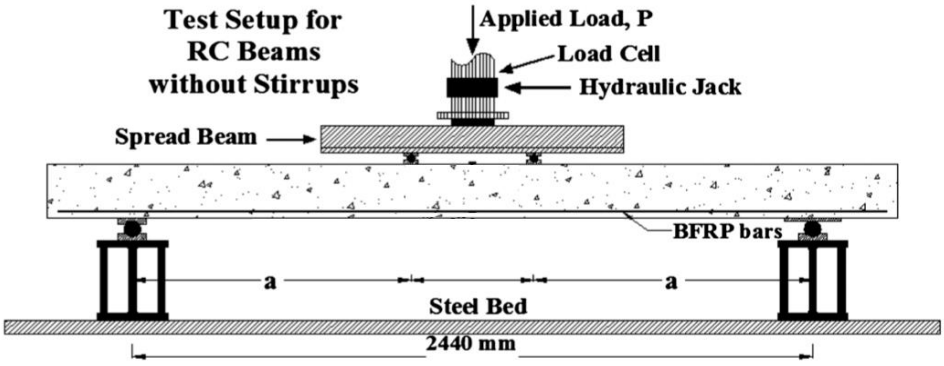

Figure 4-10 Test setup schematic (Issa et al., 2016)

4.2.4.1. Results

Considering all the specifications mentioned in the previous section as input variables, the results for those two selected specimens are illustrated in Figure 4-10. Issa et al. conducted a study to examine the impact of altering the quantity and diameter of FRPs, or varying the longitudinal reinforcement ratio, on shear capacity. It is important to highlight that as they increased these parameters, they made a slight reduction in the modulus of elasticity, decreasing it from 53 to 51 GPa. The results indicated that, according to the experimental analysis, shear failure transpired at 29.3 and 38.7 kN for the respective cases. Conversely, SCPT yielded values of 23.89 and 31.89 kN for these scenarios (Table 4-1). This demonstrates a notable 18% discrepancy between SCPT predictions and experimental findings, with SCPT providing a more conservative estimate.

One potential explanation for these disparities may be the absence of data concerning the maximum aggregate size and crack spacing, which are assumed in SCPT analysis. Additionally, the values for concrete splitting tensile strength and modulus of elasticity, which are computed according to ACI 318-19, could contribute to these differences.

When comparing these two selected samples based on their relative shear contributions, it becomes evident that the contribution from the uncracked compression zone has decreased, while the contribution from the fracture process zone has increased.

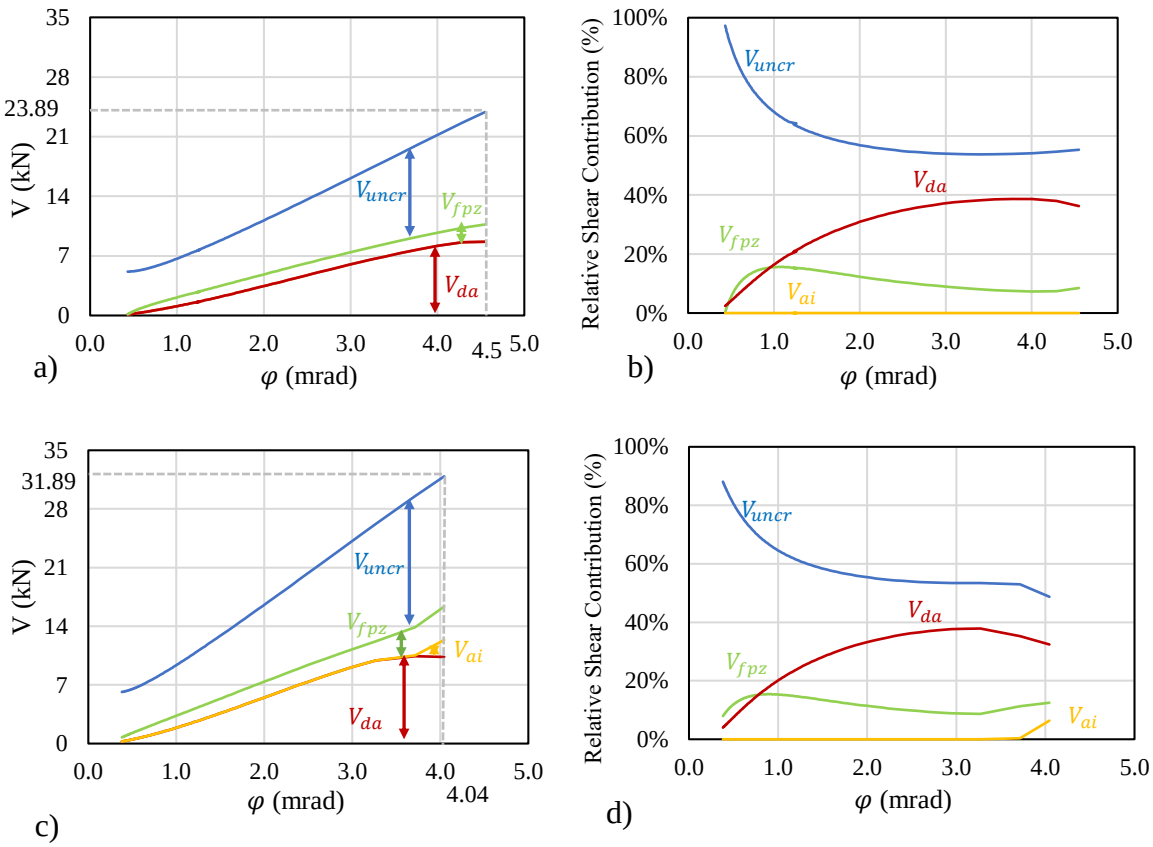

Figure 4-11 The relationship between shear crack rotation and: a) Shear force for specimen 5-10N5, b) Relative shear contribution for specimen 5-10N5, c) Shear force for specimen 5-13N5, d) Relative shear contribution for specimen 5-13N5

4.2.5. Experimental Investigation by Bentz et al. (2010)

Bentz et al. investigated the effects of different parameters such as member depth, flexural reinforcement ratio, and the amount of shear reinforcement on the shear strength of GFRP-RC beams with and without stirrups. They conducted experimental tests on a total of 11 large-scale specimens, 6 of them without stirrups and the remaining 5 with stirrups. In this study, one of the GFRP-RC specimens without shear reinforcement is selected for development and comparison with the SCPT. The detailed specifications and schematic representation can be found in Table 4-7 and Figure 4-12, respectively.

Table 4-7 Specimen specifications (Bentz et al., 2010)

Specimen #1 (M20-0)							
L (mm)	**a (mm)**	**d (mm)**	**b (mm)**	**h (mm)**	d_s **(mm)**	**n**	A_s **(mm²)**
4000	1525	405	450	500	25.4	8	13665
f_{cm} **(N/mm²)**	f_{ct} **(N/mm²)**	E_c **(N/mm²)**	E_f **(N/mm²)**	f_u **(N/mm²)**	λ_{cs}	ρ_l	d_{ag} **(mm)**
35	3.31	26622	37000	397	2.77	0.02362	10
Specimen #2 (M05-0)							
L (mm)	**a (mm)**	**d (mm)**	**b (mm)**	**h (mm)**	d_s **(mm)**	**n**	A_s **(mm²)**
4000	1525	438	450	500	25.4	2	1076
f_{cm} **(N/mm²)**	f_{ct} **(N/mm²)**	E_c **(N/mm²)**	E_f **(N/mm²)**	f_u **(N/mm²)**	λ_{cs}	ρ_l	d_{ag} **(mm)**
35	3.31	26622	37000	397	2.48	0.00546	10

Note: The splitting tensile strength (f_{ct}) and concrete modulus of elasticity (E_c) is calculated based on ACI318-19 (f_{ct} = 0.56$\sqrt{f_{cm}}$= 3.31, and E_c = 4500$\sqrt{f_c'}$= 26622).

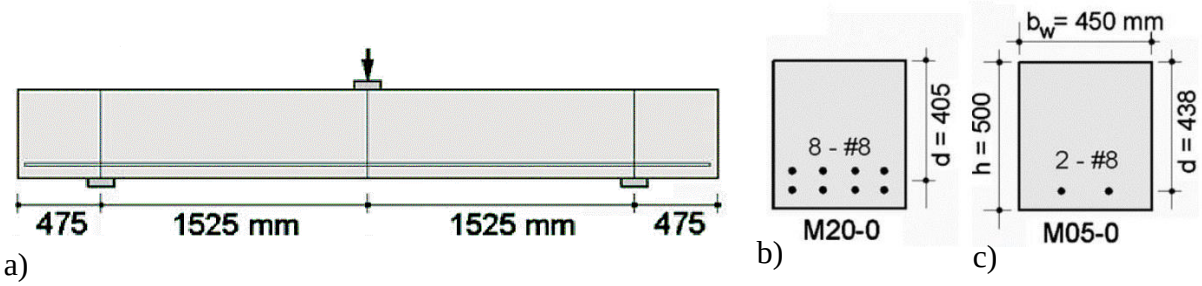

Figure 4-12 a) Test setup schematic, b) Cross-Section (M20-0), c) Cross-Section (M05-0) (Bentz et al., 2010).

4.2.5.1. Results

Considering all the specifications mentioned in the previous section as input variables, the results for those two selected specimens are illustrated in Figure 4-13. The experimental results showed that the shear capacity will reduce significantly by reducing the number of longitudinal reinforcements (leads to a lower longitudinal reinforcement ratio). The tests showed that the specimen M20-0 failed at 138.0 kN, and M05-0 failed at 86.0 kN. However, SCPT showed that

the shear failure happened at 121.59 and 70.09 kN, respectively. By comparison, the SCPT is up to 20% more conservative rather than the experimental ones (Table 4-1).

These disparities can be partially attributed to the initial assumptions regarding material properties, including concrete splitting tensile strength and modulus of elasticity which are calculated based on ACI 318-19.

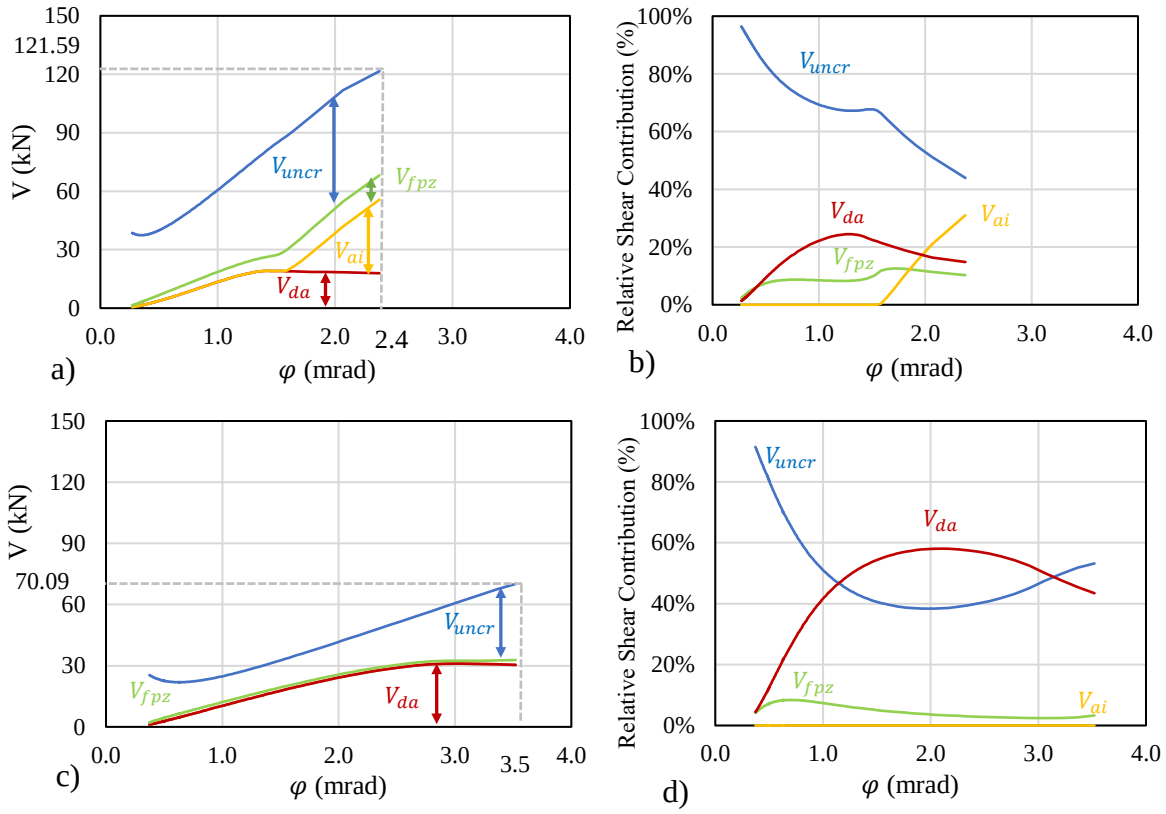

Figure 4-13 The relationship between shear crack rotation and: a) Shear force for M20-0, b) Relative shear contribution for M20-0, c) Shear force for M05-0, d) Relative shear contribution for M05-0.

Upon reviewing the SCPT outputs depicted in Figure 4-13, it is evident that reducing the longitudinal reinforcement ratio (ρ) results in a marked decrease in shear failure and a substantial increase in crack rotation. Furthermore, the contribution of dowel action significantly increases, rising from 14.8% to 43.5% (Table 4-8). Intriguingly, for lower longitudinal reinforcement ratios,

aggregate interlock does not appear to play a role in bearing the shear capacity, with dowel action taking on this responsibility.

Table 4-8 The percentage of various components at shear failure for different modulus of elasticities (%)

V_{uncr}	V_{FPZ}	V_{ai}	V_{da}	Total V
Specimen #1 (M20-0)				
43.9%	10.3%	31.0%	14.8%	100%
Specimen #2 (M05-0)				
53.2%	3.3%	0.0%	43.5%	100%

4.2.6. Experimental Investigation by Yost et al. (2001)

In 2001, a research study was conducted using an approach that examined the use of glass fiber reinforced (GFRP) materials. GFRP offers several advantages, such as having twice the tensile strength compared to steel reinforcement and being resistant to corrosion in saline environments. However, it also exhibits a significant drawback, which is its tendency to behave in an elastic-brittle manner. Nanni suggested that one way to prevent sudden brittle tensile failure is to design GFRP structures with an over-reinforced configuration relative to the balanced strain condition at ultimate (Nanni, 1993). To investigate this further, Yost et al. conducted experiments on 21 specimens (including 18 FRP-reinforced beams and three streel-reinforced beams, all without shear reinforcement) to assess the shear strength of GFRP-reinforced concrete (GFRP-RC) members. They varied the amount of longitudinal reinforcement in their experiments.

In this report, two of the GFRP-RC specimens without shear reinforcement were selected for development and comparison with the SCPT theory. The detailed specifications and schematic representation can be found in Table 4-9 and Figure 4-14, respectively.

Table 4-9 Specimen specifications (Yost et al., 2001)

Specimen #1 (4FRP)							
L (mm)	**a (mm)**	**d (mm)**	**b (mm)**	**h (mm)**	d_s **(mm)**	**n**	A_s **(mm²)**
2284	914	225	279	286	19	4	1136
f_{cm} **(N/mm²)**	f_{ct} **(N/mm²)**	E_c **(N/mm²)**	E_f **(N/mm²)**	f_u **(N/mm²)**	λ_{cs}	ρ_l	d_{ag} **(mm)**
36.3	4.73	39900	40336	689.5	3.06	0.0181	15
Specimen #2 (5FRP)							
L (mm)	**a (mm)**	**d (mm)**	**b (mm)**	**h (mm)**	d_s **(mm)**	**n**	A_s **(mm²)**
2284	914	224	254	286	22	3	1161
f_{cm} **(N/mm²)**	f_{ct} **(N/mm²)**	E_c **(N/mm²)**	E_f **(N/mm²)**	f_u **(N/mm²)**	λ_{cs}	ρ_l	d_{ag} **(mm)**
36.3	4.73	39900	40336	689.5	3.08	0.0204	15

Note: The maximum aggregate diameter is assumed 15 mm.

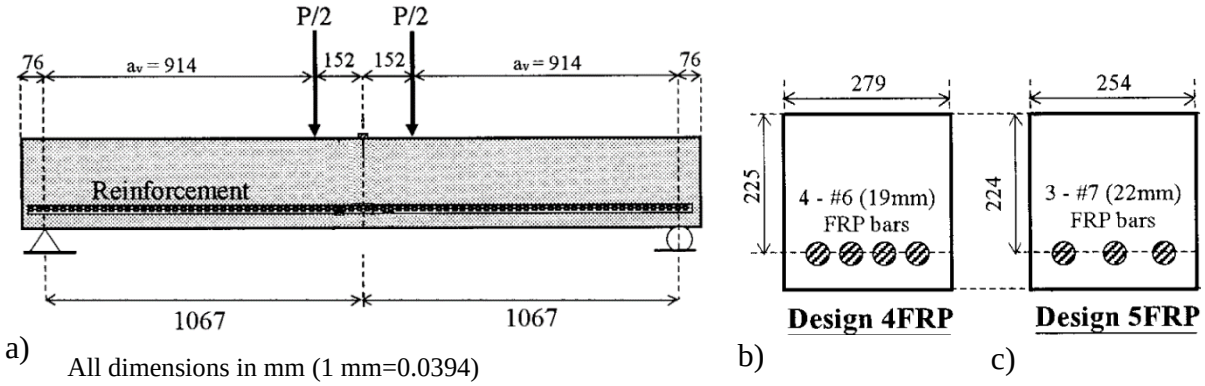

a) All dimensions in mm (1 mm=0.0394) b) c)

Figure 4-14 a) Test setup schematic, b) Cross-Section (4FRP), c) Cross-section (5FRP) (Yost et al., 2001).

4.2.6.1. Results

Utilizing all the specifications outlined in the preceding section as input variables, the results for the two chosen specimens based on SCPT analysis are depicted in Figure 4-15. Yost et al. fixed all parameters except for reinforcement specifications and sample width. The results were intriguing, revealing that the quantity of longitudinal reinforcement had an insignificant impact on shear failure. Their experimental analysis indicated that specimens 4FRP and 5FRP failed under

an average load of 45.3 and 45.1 kN, respectively. However, according to SCPT analysis, the results differed by approximately 5-10%, yielding values of 40.26 and 42.74, respectively (Table 4-1).

One significant disparity may stem from the absence of data regarding crack spacing and maximum aggregate size, both of which were assumed to be 0.7d and 15 mm in the SCPT analysis, respectively.

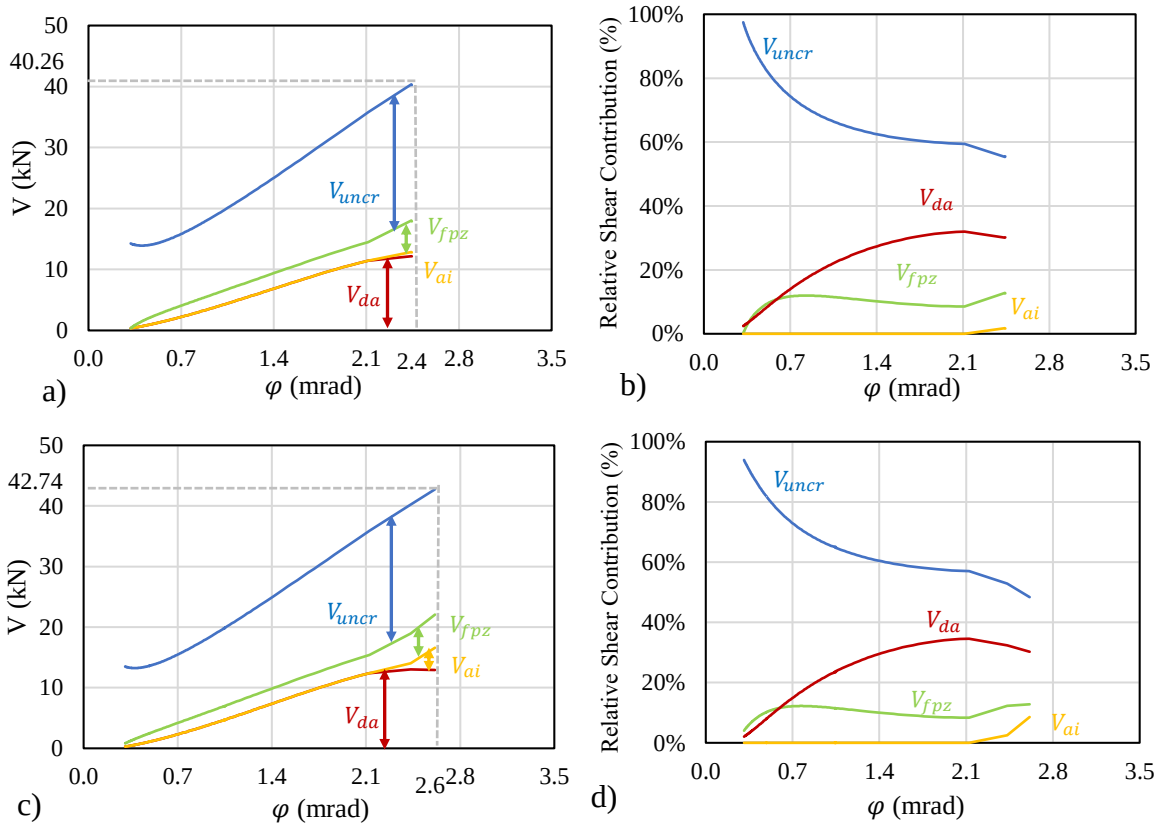

Figure 4-15 The relationship between shear crack rotation and: a) Shear force for 4FRP, b) Relative shear contribution for 4FRP, c) Shear force for 5FRP, d) Relative shear contribution for 5FRP.

Figure 4-15 illustrates that as the longitudinal reinforcement ratio increases and the specimen's width decreases, the shift of shear failure contribution occurs from the uncracked compression zone to aggregate interlock, and the fracture process zone and dowel action did not exhibit any alterations (Table 4-10).

Table 4-10 The percentage of various components at shear failure for different modulus of elasticities

V_{uncr}	V_{FPZ}	V_{ai}	V_{da}	Total V
Specimen #1 (4FRP)				
55.5%	12.7%	1.6%	30.2%	100%
Specimen #2 (5FRP)				
48.4%	12.8%	8.6%	30.3%	100%

4.2.7. Experimental Investigation by Guadagnini et al. (2006)

In 2006, a group of scholars conducted twelve experimental tests (FRC and RC beams with and without shear reinforcement) by varying the shear span to depth ratio to investigate the shear resistance of a beam for different levels of the strain distribution. Besides, they compared their results with two different design codes, ACI 2003 and the Institution of Structural Engineers 1999 (ISE).

Table 4-11 Specimen specifications (Guadagnini et al., 2006)

Specimen #1 (GB43)							
L (mm)	**a (mm)**	**d (mm)**	**b (mm)**	**h (mm)**	d_s **(mm)**	**n**	A_s **(mm²)**
2300	750	223	150	250	13.5	3	429
f_{cm} **(N/mm²)**	f_{ct} **(N/mm²)**	E_c **(N/mm²)**	E_f **(N/mm²)**	f_u **(N/mm²)**	λ_{cs}	ρ_l	d_{ag} **(mm)**
42.8	4.38	29440	45000	1000	2.3	0.0128	20
Specimen #2 (GB44)							
L (mm)	**a (mm)**	**d (mm)**	**b (mm)**	**h (mm)**	d_s **(mm)**	**n**	A_s **(mm²)**
1800	500	223	150	250	13.5	3	429
f_{cm} **(N/mm²)**	f_{ct} **(N/mm²)**	E_c **(N/mm²)**	E_f **(N/mm²)**	f_u **(N/mm²)**	λ_{cs}	ρ_l	d_{ag} **(mm)**
42.8	4.38	29440	45000	1000	1.2	0.0128	20

Note: The yield strength of reinforcement steel is assumed equal to 1000 MPa (f_y).

In this report, two of the GFRP-RC specimens without shear reinforcement have been selected for verifying the code for FRP-RC members. Detailed specifications of these two specimens can be found in Table 4-10, while their schematic representation is presented in Figure 4-16.

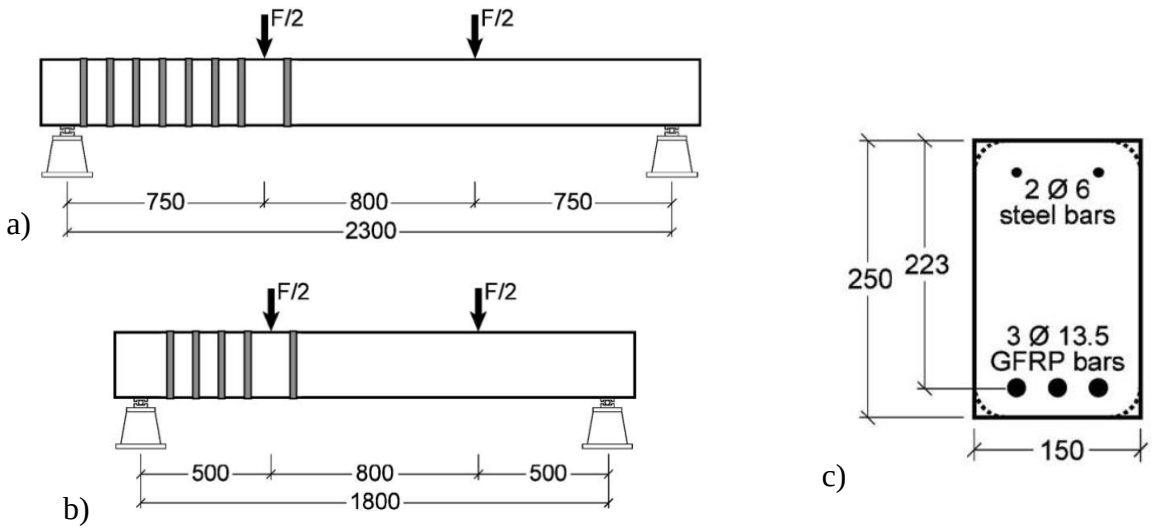

Figure 4-16 a) Test setup schematic (GB43), b) Test setup schematic (GB44), b) Cross-Section for both specimens (Guadagnini et al., 2006)

4.2.7.1. Results

By employing all the parameters described in the previous section as input variables, Figure 4-17 illustrates the outcomes obtained from SCPT analysis for the two selected specimens. Guadagnini et al. conducted a comparison of two specimens by varying their shear slenderness, modifying both the length and shear span. The specimens GB43 and GB44 exhibited failure loads of 27.15 and 44.7 kN in the experimental tests, respectively. However, the SCPT analysis yielded contrasting results. For Sample GB43, the calculated load was approximately 28.35 kN, which represents a nearly 4% increase compared to the experimental results. Conversely, for Sample GB44 (which has a lower shear slenderness), the SCPT analysis indicated a load of 32.88 kN, roughly 25% reduction compared to the experimental findings (Table 4-1).

One of the possible reasons for these differences can be the assumption for crack spacing which is considered equal to 0.7d in the SCPT analysis.

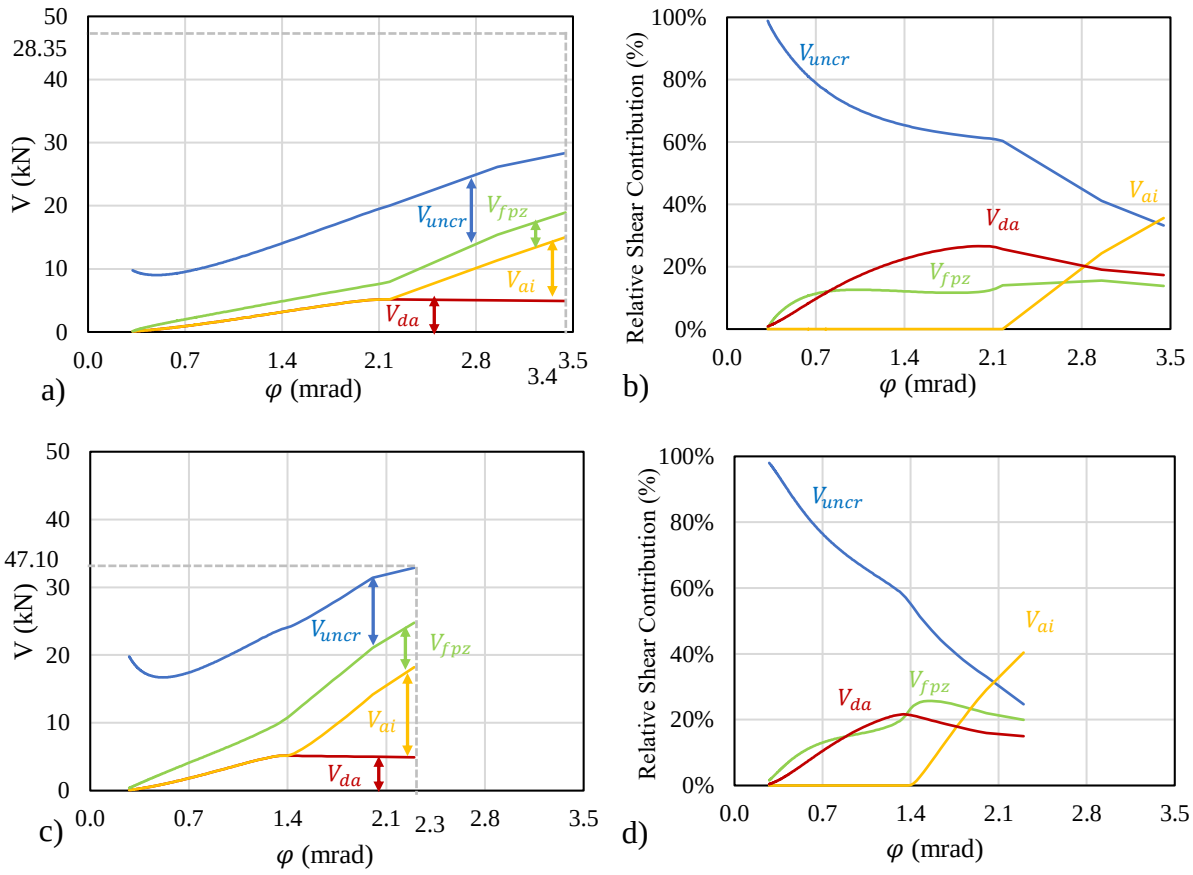

Figure 4-17 The relationship between shear crack rotation and: a) Shear force for GB43, b) Relative shear contribution for GB43, c) Shear force for GB434, d) Relative shear contribution for GB434.

The SCPT analysis results indicate that reducing the shear slenderness leads to an increase in shear capacity and a decrease in crack rotation. Additionally, Figure 4-17 reveals that aggregate interlock play a significant role in bearing the shear failure at both specimens, it contributes to approximately 35-40% of the total shear failure. Furthermore, decreasing the shear slenderness results in reduced contributions from the uncracked compression zone and dowel action. However, it significantly increases the fracture process zone contribution, as depicted in Figure 4-17 and Table 4-12.

Table 4-12 The percentage of various components at shear failure for different modulus of elasticities

V_{uncr}	V_{FPZ}	V_{ai}	V_{da}	Total V
Specimen #1 (4FRP)				
33.2%	13.8%	35.6%	17.3%	100%
Specimen #2 (5FRP)				
24.7%	19.9%	40.4%	15.0%	100%

4.2.8. Experimental Investigation by Kim et al. (2014)

In 2014, Kim et al. asserted that FRP materials exhibit high strength-to-weight ratios, making them a preferable choice for usage in lightweight concrete structures. This recommendation is based on the potential economic and seismic advantages associated with the use of FRP bars.

Their research consisted of two main parts. The first part involved developing an empirical equation to examine how the elastic modulus of FRP, the shear span-to-depth ratio, and the flexural reinforcement ratio affect the shear strength of FRP-RC beams without shear reinforcement. The second part of their study involved conducting 24 tests on FRP-reinforced lightweight concrete beams and comparing the results with the equations derived in the first part. This experimental phase encompassed two types of FRP bars, two concrete compressive strengths, and three different flexural reinforcement ratios.

In this report, one CFRP and one GFRP-RC specimens without shear reinforcement have been selected for verifying our research. Detailed specifications of these two specimens can be found in Table 4-13, while their schematic representations are presented in Figure 4-18.

Table 4-13 Specimen specifications (Kim & Jang, 2014)

Specimen #1 (C-3.5-R3)							
L (mm)	**a (mm)**	**d (mm)**	**b (mm)**	**h (mm)**	d_s **(mm)**	**n**	A_s **(mm²)**
3200	747.25	213.5	150	250	13	2	253.4
f_{cm} **(N/mm²)**	f_{ct} **(N/mm²)**	E_c **(N/mm²)**	E_f **(N/mm²)**	f_u **(N/mm²)**	λ_{cs}	ρ_l	d_{ag} **(mm)**
30	3.07	24648	147900	2023	2.5	0.0079	9.5
Specimen #2 (G-3.5-R3)							
L (mm)	**a (mm)**	**d (mm)**	**b (mm)**	**h (mm)**	d_s **(mm)**	**n**	A_s **(mm²)**
3200	747.25	213.5	150	250	13	2	253.4
f_{cm} **(N/mm²)**	f_{ct} **(N/mm²)**	E_c **(N/mm²)**	E_f **(N/mm²)**	f_u **(N/mm²)**	λ_{cs}	ρ_l	d_{ag} **(mm)**
30	3.07	24648	49100	940.6	2.5	0.0079	9.5

Note: The splitting tensile strength (f_{ct}) and concrete modulus of elasticity (E_c) is calculated based on ACI318-19 (f_{ct} = 0.56$\sqrt{f_{cm}}$= 3.07, and E_c = 4500$\sqrt{f_c'}$= 24648).

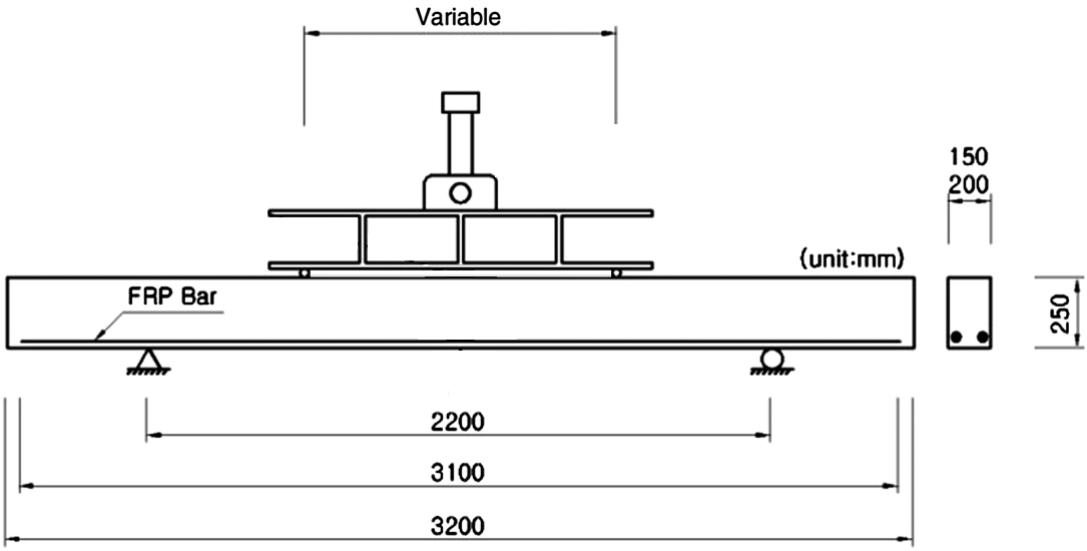

Figure 4-18 Test setup schematic (Kim & Jang, 2014)

4.2.8.1. Results

Using all the input variables outlined in the preceding section, Figure 4-19 displays the results derived from the SCPT analysis of the two chosen specimens. Kim et al. conducted a study to

examine the influence of different types of FRP on shear capacity, as outlined in Table 4-13. The findings indicated that the CFRP-RC beam exhibited failure at 29.0 kN, while the GFRP-RC failed at 18.8 kN. However, when subjected to SCPT analysis, the results appeared to be more conservative, with values of 25.88 kN and 16.88 kN, respectively. This suggests that SCPT analysis yielded results that were approximately 10% lower than the experimental analysis (Table 4-1).

These disparities may be attributed to the absence of data concerning initial assumptions or crack spacing. Additionally, the article did not provide information on the splitting tensile strength and the modulus of elasticity of concrete. Consequently, these two parameters were computed for the SCPT analysis following the code ACI 318-19.

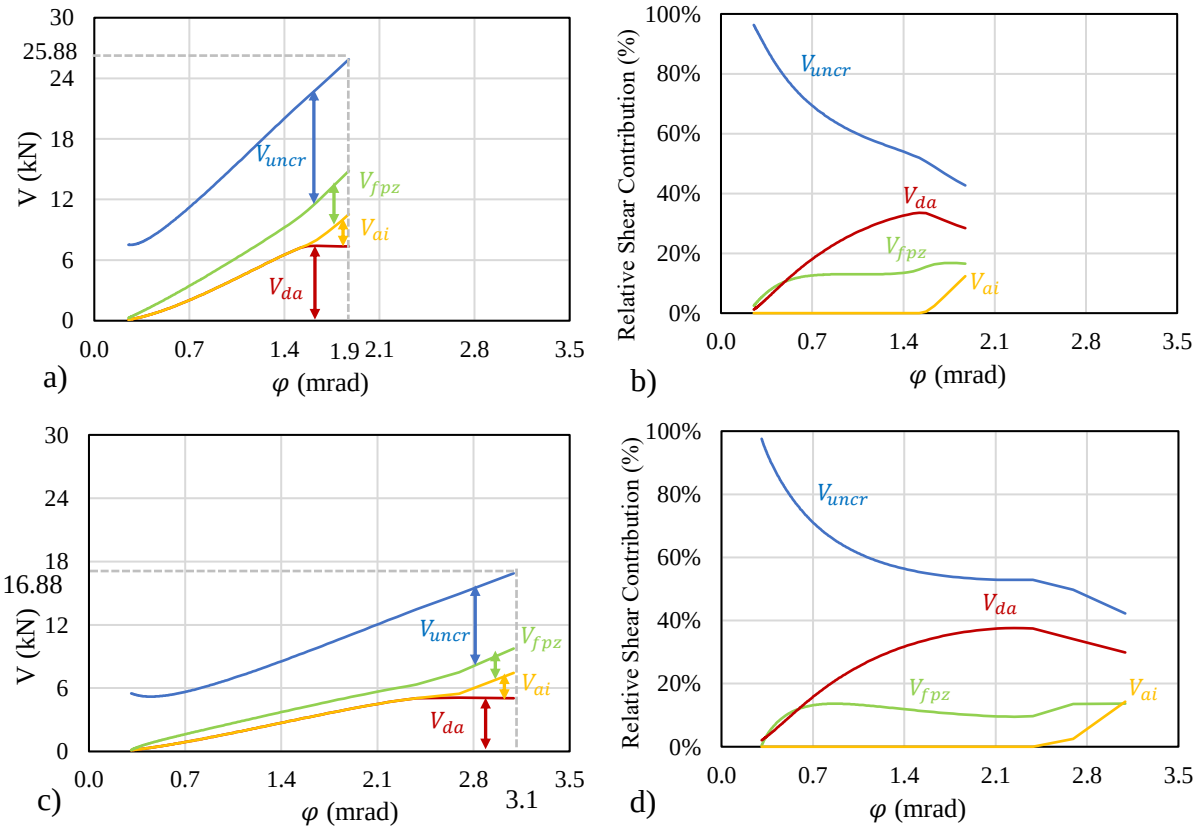

Figure 4-19 The relationship between shear crack rotation and: a) Shear force for C-3.5-R3, b) Relative shear contribution for C-3.5-R3, c) Shear force for G-3.5-R3, d) Relative shear contribution for G-3.5-R3.

Figure 4-19 illustrates that reducing the modulus of elasticity by one-third resulted in a 35% decrease in shear capacity. Furthermore, it is evident from Figures 4-19 and 4-20 that crack rotation at the shear failure point and crack width at the longitudinal reinforcement layer both experienced a significant increase.

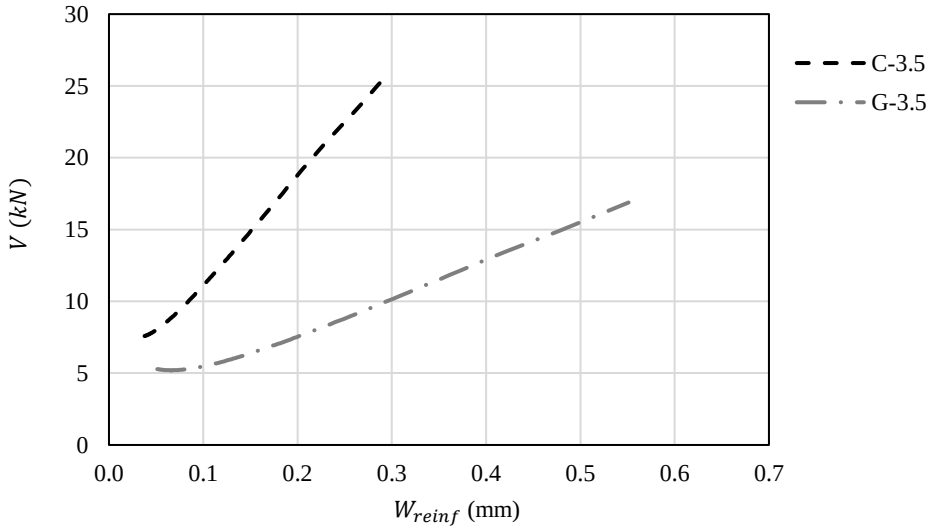

Figure 4-20 The relationship between shear force and the crack width in the longitudinal reinforcement layer, based on SCPT analysis.

4.2.9. Experimental Investigation by Razaqpur et al. (2004)

In 2004, Razaqpur et al. tested seven simply supported CFRP-RC beams without shear reinforcement to investigate the effect of concrete contribution on shear strength by varying the shear span to depth ratio (from 1.82 to 4.5) and the flexural reinforcement ratio (from 1.1 to 3.88). They also compared their results with three various design codes, the American Concrete Institute (ACI 318-02), the Canadian Standard (CSA S806-02), and the Japan Society of Civil Engineers (JSCF 1997).

In this report, two different CFRP-RC specimens have been selected for verification. Detailed specifications of these two specimens can be found in Table 4-14, while their schematic representations are presented in Figure 4-21.

Table 4-14 Specimen specifications (Razaqpur et al., 2004)

Specimen #1 (BR1)							
L (mm)	**a (mm)**	**d (mm)**	**b (mm)**	**h (mm)**	d_s **(mm)**	**n**	A_s **(mm²)**
2262	600.75	225	200	250	8	2	112.50
f_{cm} **(N/mm²)**	f_{ct} **(N/mm²)**	E_c **(N/mm²)**	E_f **(N/mm²)**	f_u **(N/mm²)**	λ_{cs}	ρ_l	d_{ag} **(mm)**
40.5	3.56	28638	145000	2250	1.67	0.0025	20
Specimen #2 (BR4)							
L (mm)	**a (mm)**	**d (mm)**	**b (mm)**	**h (mm)**	d_s **(mm)**	**n**	A_s **(mm²)**
2262	1012.50	225	200	250	8	4	225
f_{cm} **(N/mm²)**	f_{ct} **(N/mm²)**	E_c **(N/mm²)**	E_f **(N/mm²)**	f_u **(N/mm²)**	λ_{cs}	ρ_l	d_{ag} **(mm)**
40.5	3.56	28638	145000	2250	3.50	0.0050	20

Note 1: The maximum aggregate diameter is assumed 20 mm.

Note 2: The splitting tensile strength (f_{ct}) and concrete modulus of elasticity (E_c) is calculated based on ACI318-19 (f_{ct} = 0.56$\sqrt{f_{cm}}$= 3.56, and E_c = 4500$\sqrt{f_c'}$= 26622).

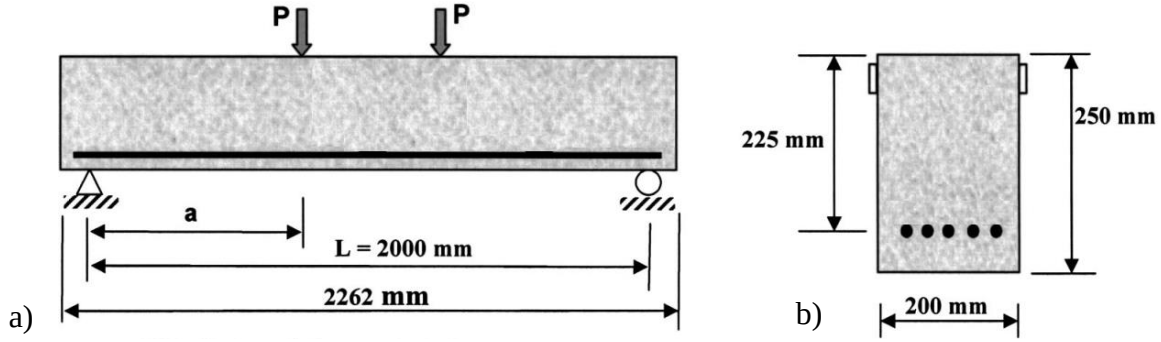

Figure 4-21 a) Test setup schematic, b) Cross-Section (Razaqpur et al., 2004)

4.2.9.1. Results

With the utilization of all the input parameters described in the previous section, Figure 4-22 exhibits the outcomes obtained through the SCPT analysis of the selected pair of specimens. Razaqpur et al. increased the shear slenderness (λ_{cs}) and doubled the longitudinal reinforcement ratio (ρ), resulting in a 10% increase in shear failure (from 36.11 kN to 38.45 kN). In contrast, SCPT analysis demonstrated a similar trend but failed at more conservative results (32.27 kN and 32.17 kN, respectively) (Table 4-1).

These substantial disparities between the experimental and SCPT analyses may be attributed to the absence of data on maximum aggregate interlock, crack spacings, splitting tensile strength, and concrete modulus of elasticity (with the latter parameters being calculated according to ACI-318-19 code).

Figure 4-22 presents the SCPT analysis results, where it is evident that the primary role is played by the aggregate interlock mechanism, accounting for approximately 31.1% of the shear capacity for the first specimen. However, in specimen#2, the uncracked compression zone played this role, accounting for 42.8% of the shear capacity. Besides, in specimen#2, a decrease in the fracture process zone and dowel action mechanisms can be observed compared to the specimen#1.

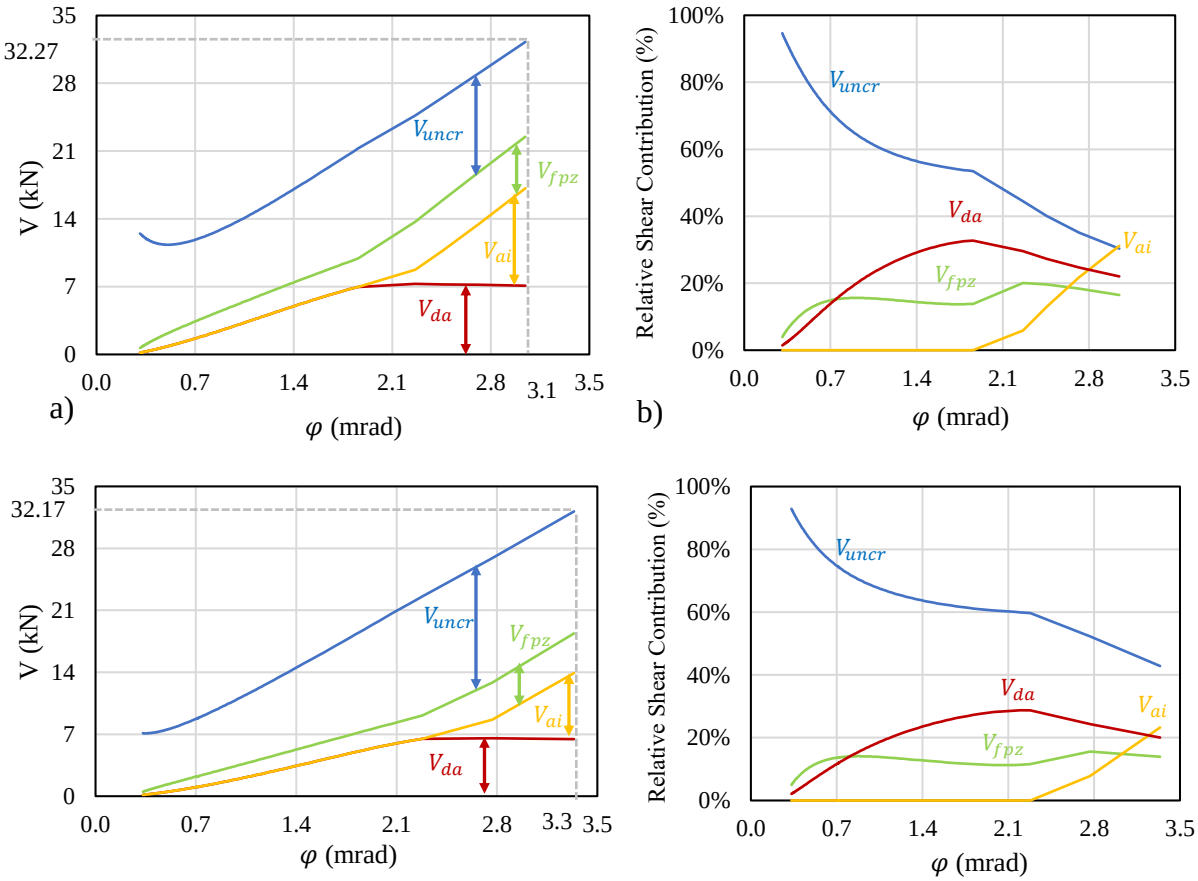

Figure 4-22 The relationship between shear crack rotation and: a) Shear force for BR1, b) Relative shear contribution for BR1, c) Shear force for BR4, d) Relative shear contribution for BR4

Table 4-15 The percentage of various components at shear failure for different modulus of elasticities

V_{uncr}	V_{FPZ}	V_{ai}	V_{da}	Total V
Specimen #1 (BR1)				
30.3%	16.5%	31.1%	22.0%	100%
Specimen #2 (BR4)				
42.8%	13.9%	23.2%	20.0%	100%

4.3 Discussion and Summary

This chapter is dedicated to the validation of the modified SCPT code through a comparative analysis of its results with 20 experimental analyses. The findings of this comparison are presented in Figure 4-23.

Upon thorough examination of these results, it becomes apparent that the SCPT methodology consistently exhibited a conservative trend for the FRP-RC beams considered for this validation. Specifically, the average ratio of shear capacity predicted by SCPT to the actual experimental values was approximately 0.88.

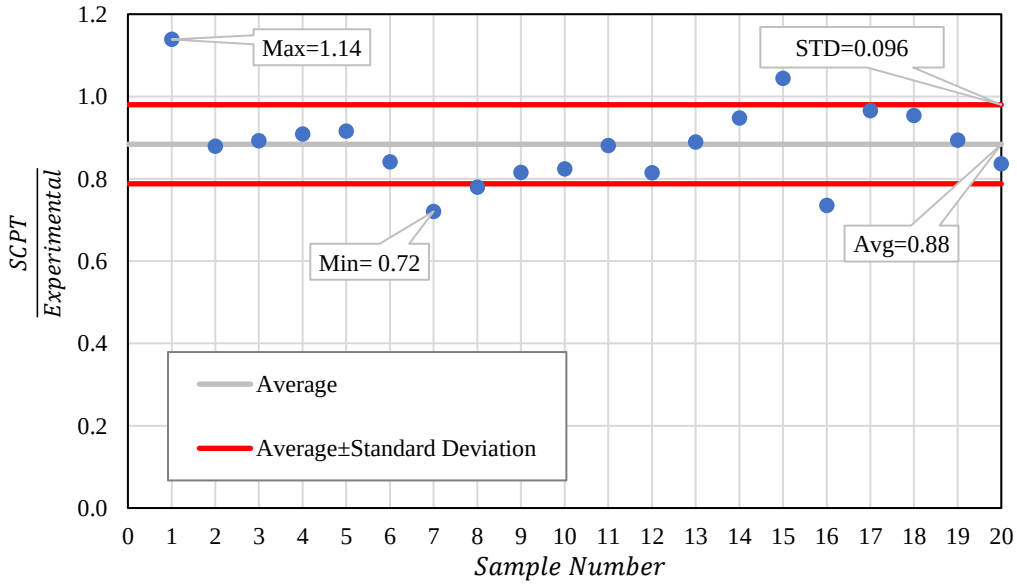

Figure 4-23 The analysis of SCPT validation for FRP-RC beams based on 19 experimental data.

Figure 4-1a presents a comparative analysis between experimental data and results derived from SCPT analysis. The coefficient of determination (R^2) for this analysis is calculated to be 0.9559 (Eq. 4-1), signifying a noteworthy level of concordance between the predicted and experimental analyses despite the conservative tendency. It achieved the second-highest level of accuracy, with CSA S806 performing slightly better but exhibiting a slightly unconservative tendency (Table 4-1). Besides, the standard deviation based on SCPT analysis demonstrates the lowest variation compared to other standards, as shown in Figure 4-1.

$$R^2 = \left(\frac{\sum (x_i - \bar{x})\,(y_i - \bar{y})}{\sqrt{\sum (x_i - \bar{x})^2\,(y_i - \bar{y})^2}} \right)^2 \qquad \text{Eq. 4- 1}$$

Figures 4-24, and 4-25 illustrate that the precision of SCPT predictions exhibits limited sensitivity to variations in the modulus of elasticity and stiffness of FRP.

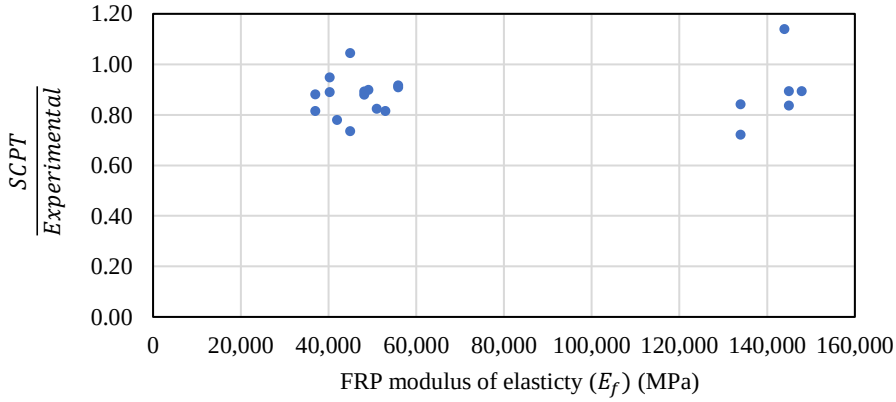

Figure 4-24 The analysis of SCPT to experimental analysis ratio versus FRP modulus of elasticity.

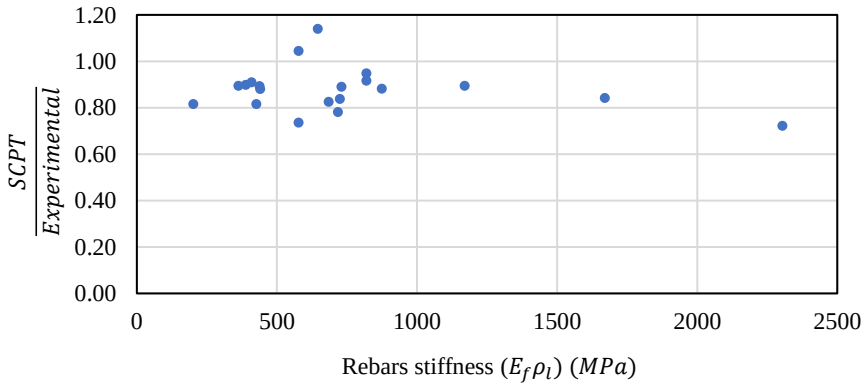

Figure 4-25 The analysis of SCPT to experimental analysis ratio versus rebars' stiffness.

These disparities between the SCPT and experimental outputs may be attributed to several possible reasons, as listed below:

1. Uncertainty in the initial assumptions used in SCPT analysis, such as β, Δy, σ_{z0}, φ.

For instance, by changing the increment of Δy from 0.3 mm to 0.1 mm, the results changed by 0.2%. Although this change was not significant, it is possible that other parameters could also be affective. This study did not cover the effect of other parameters on results, so it would be good to consider them in future work.

2. The insufficiency of reported data pertaining to the splitting tensile strength and the modulus of elasticity of concrete, which in many cases was computed according to the ACI 318-19 code. To address this concern, two various splitting tensile strength values have been considered for one of the experimental analyses to ascertain the code's responsiveness to such variations.

For instance, in the context of Noel's research, the splitting tensile strength of the G1 specimen was determined to be 4.27 MPa according to the calculations based on ACI 318-19 standards, with the SCPT predicted shear failure occurring at 78.50 kN. However, Noel reported a measured value of 3.9 MPa for the splitting tensile strength which corresponds to a predicted shear failure load of 75.50 kN, a difference of 4% (Fig. 4-26). Consequently, it can be inferred that one of the disparities between the experimental analysis and the present study could be the cumulative effects associated with potential uncertainty with respect to material properties and constitutive behaviour. It is noteworthy that, in most of the experimental analyses included in this research, the concrete tensile strength was assessed using the ACI 318-19 equations for validation purposes.

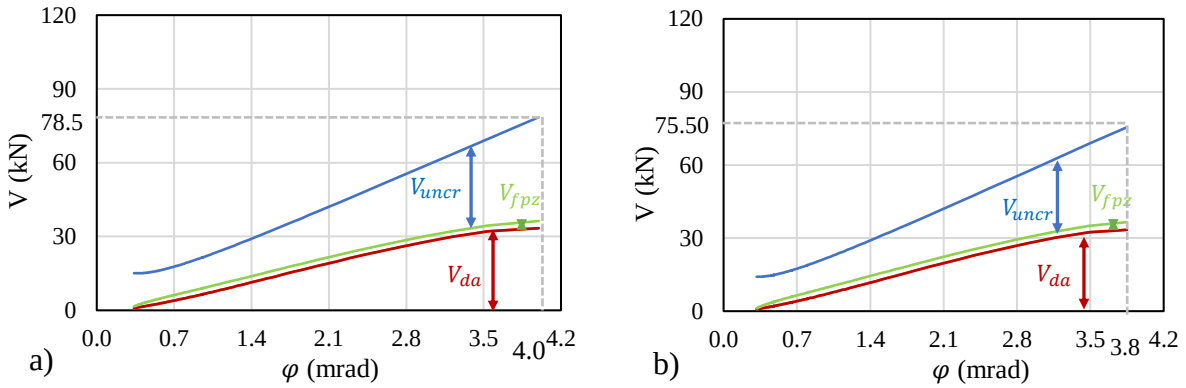

Figure 4-26 The analysis of SCPT for different concrete tension strength based on Noel analysis (Noël, 2013): a) $f_{ct} = 4.27$, b) $f_{ct} = 3.9\ MPa$.

3. Another insufficient information is related to the precise location of the primary crack responsible for inducing shear failure. In all validation analyses conducted, this location has been assumed to be located at the distance of d from the loading point.

To investigate this issue, a specific set of experimental data was selected for further analysis (Bentz et al., 2010).

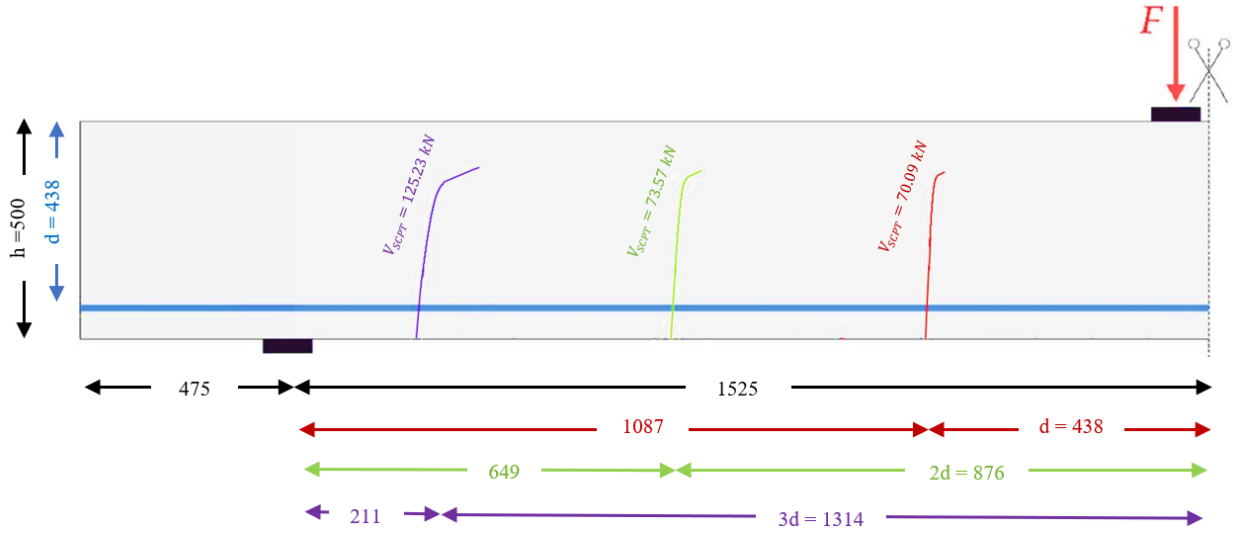

Figure 4-27 The analysis of SCPT for different major crack location based on Bentz data (all dimensions are in mm).

By systematically varying the location of the major crack, we aimed to assess the code's sensitivity to this particular parameter and discern any resultant effects on the obtained outcomes. Figure 4-

27 demonstrates that varying the crack location can lead to variations in shear capacity, with the lowest shear strength occurring at a distance of d from the loading point, as consistently assumed throughout our validation analyses.

4. Lack of data on crack spacing is observed in certain experimental datasets. In accordance with the reference SCPT article, a uniform assumption has been made, wherein crack spacing is considered to be consistently equal to 0.7d.

To investigate the influence of crack spacing on the outcomes, an analysis was conducted on the Schmidt data (Schmidt et al., 2021). Specifically, the crack spacing was varied within the range of 0.7d to 0.5d. The results of this analysis revealed a small enhancement in shear strength, approximately amounting to a 6% increase, when using a smaller crack spacing. The shear strength values exhibited this effect by transitioning from 103.47 kN to 109.72 kN, as illustrated in Figure 4-28.

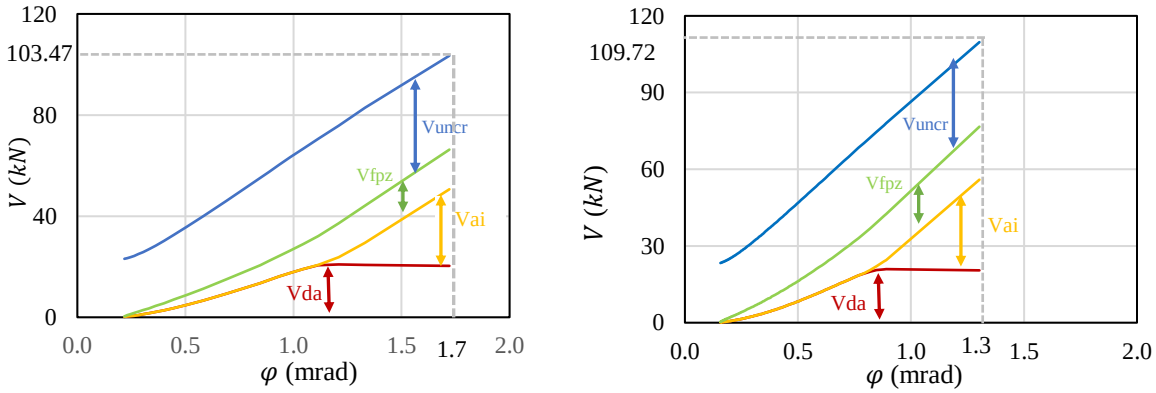

Figure 4-28 The analysis of SCPT for different crack spacing based on Schmidt analysis (Schmidt et al., 2021): a) $S_{cr} = 0.7d$, b) $S_{cr} = 0.5d$.

5. The lack of information on the maximum aggregate size in some cases.

To investigate the influence of maximum aggregate size within the context of the SCPT model, a specific experimental analysis (Issa et al., 2016) was chosen and subsequently examined for two discrete values: 10 mm and 20 mm.

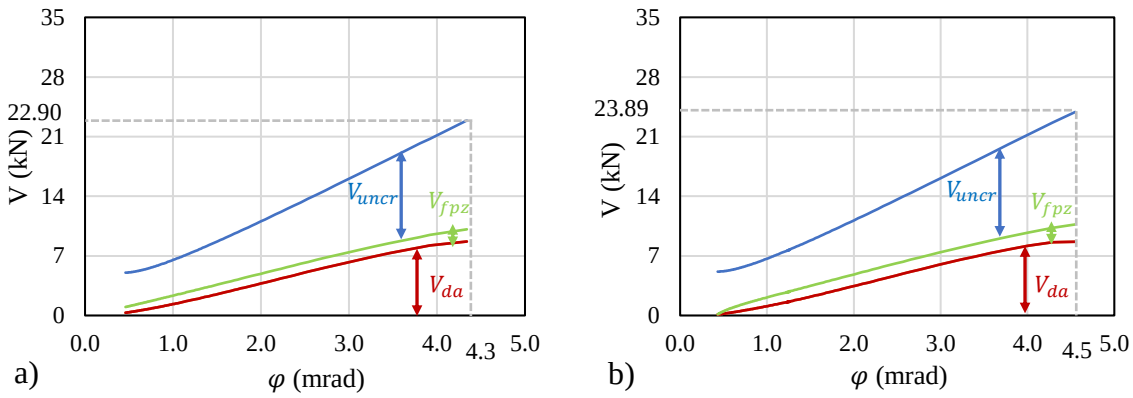

Figure 4-29 The analysis of SCPT for different maximum aggregate size based on Issa analysis (Issa et al., 2016): a) $d_{ag} = 10\ mm$, b) $d_{ag} = 20\ mm$.

This scrutiny was undertaken with the primary objective of elucidating the impact of this parameter on the shear strength, as depicted in Figure 4-30. The results indicated that increasing this parameter from 10 to 20 mm has led to an approximately 5% increase in shear strength.

6. The inclusion of certain parameters provided by manufacturers may not accurately reflect values obtained through laboratory testing. Indeed, the material specifications presented by manufacturers often differ from the results obtained through laboratory experiments since they provide more conservative values for design purposes. For a more precise analysis, it is essential to rely on laboratory data. Therefore, one of the primary reasons for the disparity between experimental and SCPT results can be attributed to the absence of laboratory data in some of the referenced articles (the data provided by the manufacturers are detailed in Table 4-1).

Chapter 5

Conclusions

5.1 Introduction

In this research, an extensive review of the previous shear strength methods was conducted, and influential parameters and gaps of the previous studies have been identified. A recently developed theory named SCPT was used to analyze a beam without shear reinforcement by observing every stage of crack propagation during the loading process. This comprehensive analysis enables us to gain a deeper understanding of how cracks initiate, propagate, and interact with the surrounding material in the absence of shear reinforcement. In addition, the SCPT method is able to evaluate the contributions of various shear transfer mechanisms at all stages of loading.

Then, its application has been expanded to beams reinforced with FRP bars. FRP bars are increasingly being used as a corrosion-resistant alternative to steel reinforcement to design longer lasting structures. The use of FRP reinforcement is known to significantly influence shear behaviour of RC beams because of their lower elastic moduli, dowel capacity, and different bond characteristics compared to steel bars.

The SCPT allows the contributions of different shear transfer mechanisms to be evaluated at all stages of loading. Based on the results of this study, the following preliminary conclusions can be drawn:

- Effect of modulus of elasticity: It is demonstrated that as the modulus decreases, the shear capacity also decreases significantly. Lowering the modulus from 200 GPa to 150 GPa resulted in only a modest reduction in ultimate strength for the beam geometry and reinforcement ratio evaluated, while a modulus of 50 GPa led to a substantial 61% decrease in shear capacity compared to the reference beam. Different mechanisms, such as dowel action, uncracked compression zone, fracture process zone, and aggregate interlock contribute differently to shear resistance, and these contributions vary with the modulus. Aggregate interlock is particularly sensitive to changes in reinforcement stiffness. Lower modulus values also lead to increased crack opening at the height of reinforcement layer. It is also indicated that the relative contributions of these mechanisms evolve throughout the loading process, with dowel action initially dominant and aggregate interlock becoming significant at higher angles of inclination for certain reinforcement moduli. However, aggregate interlock does not play a role in shear resistance for beams with the lowest reinforcement stiffness.
- Effect of dowel action: By modifying dowel action for FRP-RC beams using the $(E_f/E_s)^{1/3}$ ratio, the primary mechanism that undergoes significant changes was dowel action. This contrasted with the previous section, where dowel action remained relatively consistent across various modulus values. The reduction in dowel action also led to a decrease in crack rotation at failure and an earlier engagement of aggregate interlock. Even in beams

for reinforcement moduli of 50 GPa, there was a modest contribution from aggregate interlock at the point of failure.

- Effect of tension stiffening: The impact of tension stiffening on FRP-RC structures (by keeping dowel action and other variables constant) showed that it had minimal influence on shear strength outcomes, showing nearly identical results to cases without tension stiffening. These findings offer insights into the role of tension stiffening in FRP-RC structures, indicating that it may not significantly impact shear strength within the studied parameter range.
- Effect of concrete tension strength: The absence of data on concrete's splitting tensile strength in many reported studies led us to investigate how the SCPT predictions respond to variations in this parameter. It showed that when the concrete tensile strength was reduced by 10%, the shear strength decreased by approximately 4%.
- Effect of major crack location: It is challenging to accurately predict the location of the primary crack location responsible for instigating shear failure in structural elements. To address this issue systematically, a series of adjustments to the crack location were made at three distinct positions, spanning from a distance of d from the point load to a region near the support area. The outcomes of this investigation consistently demonstrated that the lowest shear strength was predicted when the crack was positioned at a distance of d away from the point load.
- Effect of crack spacing: Classen (2020) established the assumption that crack spacing is equivalent to 0.7 times the crack depth (0.7d). To assess the influence of crack spacing on the SCPT code, an analysis was conducted using the dataset from Schmidt et al. (2021). This analysis involved varying the crack spacing within the range of 0.7d to 0.5d. The

results indicated a marginal enhancement in shear strength, constituting an approximate 6% increase. Consequently, for the validation section, it was assumed that the crack spacing for all specimens adhered to the 0.7d assumption unless explicitly specified otherwise in the corresponding experimental data.

- Effect of maximum aggregate size: To explore the influence of maximum aggregate size in the SCPT model, a particular experimental analysis was selected and evaluated for two distinct values: 10 mm and 20 mm. The findings indicated a notable enhancement in shear strength as the maximum aggregate size increased. This underscores the significance of aggregate size in shear strength, specifically in relation to the aggregate interlock mechanism.

In conclusion, after a comprehensive analysis of 20 experimental datasets, and by comparing with three different codes (ACI Code 440.11-22; CSA S6:19; CSA S806-12), it is evident that the SCPT methodology consistently demonstrates a conservative tendency. More precisely, the average ratio between the shear capacity predicted by SCPT and the actual experimental values stands at approximately 0.88. Compared to existing code equations, only the CSA S806 provisions were more accurate (albeit slightly unconservative), and the SCPT was the most consistent (i.e., had the lowest standard deviation for the predicted-experimental ratio).

5.2 Future Work

Several parameters lay outside the scope of the current investigation, despite their potential to yield deeper insights into certain observations presented in this study. It is recommended that future research endeavours encompass the following considerations:

- In this study, we have explored the implications of the tension stiffening effect on FRP-RC members. However, it is worth noting that the bond effect, specifically pertaining to the absence of lugs and ribs in FRP bars, presents an additional dimension for investigation. Incorporating an analysis of the bond effect could provide valuable insights into the structural behaviour of FRP-RC elements, further enhancing our understanding of their mechanical properties and behaviour under different loading conditions. Future research endeavours in this domain could consider integrating an examination of the bond effect alongside the tension stiffening effect to comprehensively assess the performance of FRP-RC members.
- Within the context of this study, our investigation has predominantly focused on the application of concentrated loads to simply supported beams. However, it is imperative to acknowledge the broader spectrum of loading conditions that can influence the behaviour of such beams. In future research endeavours, it is advisable to incorporate a more comprehensive range of loading scenarios. These may encompass distributed loads for both simply and fixed supports, as well as the combinations of concentrated and distributed loads.
- In this study, the validation of the SCPT model has been undertaken within the context of FRP-RC beams. However, it is essential to recognize that the model's applicability extends beyond this scope and can be extended to encompass corroded steel-RC beams as well. Future research endeavours may consider the validation of the SCPT model within the context of deteriorated or corroded structural elements. This expansion of validation parameters would not only enhance the model's reliability and adaptability but also

contribute significantly to our understanding of its effectiveness in predicting the behaviour of reinforced concrete structures under deterioration.

- While the present study has provided a certain level of coverage regarding the impact of beam depth, shear span, and reinforcement ratio within the validation chapter, it is important to note that there remains an opportunity for more comprehensive exploration of these parameters in future research endeavours.
- The SCPT code was initially developed for beams without shear reinforcement. Nevertheless, its applicability can be extended to encompass beams with shear reinforcement, with subsequent validation against experimental data.
- In bridge design, prestressed beams represent a prevalent structural component. The incorporation of prestressed beams into the SCPT framework can be explored to examine their influence on structural behaviour. Additionally, the validation of this extension can be conducted through comparative analysis with existing beams.
- The investigation of various beam sections, including circular beams, constitutes another pertinent parameter for analysis. By incorporating this parameter and considering other potential areas for future research, such as the inclusion of fixed support conditions and stirrups, the SCPT model's scope can be expanded to encompass the analysis of columns as well. This extension of the model would facilitate a more comprehensive evaluation of structural elements beyond beams.

References

ACI 440.11-22. (2022). Building Code Requirements for Structural Concrete Reinforced with Glass Fiber-Reinforced Polymer (GFRP) Bars: Code and Commentary. American Concrete Institute.

ACI318-19. (2019). Building Code Requirements for Structural Concrete (ACI 318-19) and Commentary. American Concrete Institute.

Adam, V., Schmidt, M., & Hegger, J. (2022). One-way flexural shear tests on wide reinforced concrete slab segments with simple and intermediate supports. Structural Concrete.

Aiello, M. A., Leone, M., & Pecce, M. (2007). Bond Performances of FRP Rebars-Reinforced Concrete. Journal Of Materials in Civil Engineering, 19(3), 205–213.

Alam, M. S., & Hussein, A. (2013). Size Effect on Shear Strength of FRP Reinforced Concrete Beams without Stirrups. Journal of Composites for Construction, 17(4), 507–516.

Alguhi, H., & Tomlinson, D. (2021). One-Way Shear Strength of FRP–Reinforced Concrete Members Without Stirrups: Design Provision Review. Journal of Composites for Construction, 25(3).

Bazant, Z., & Chen, E.-P. (1997). Scaling of structural failure*. American Society of Mechanical Engineers, 50(10), 593–627.

Bazant, Z. P., & Kazemi, M. T. (1991). Size Effect on Diagonal Shear Failure of Beams without Stirrups. ACI Structural Journal, 88(3), 268–276.

Bazant, Z. P., & Kim, J.-K. (1984). Size Effect in Shear Failure of Longitudinally Reinforced Beams.

Bentur, A., Diamond, S., & Berke, N. S. (1997). Steel corrosion in concrete. E & FN Spon.

Bentz, E. C. (2005). Explaining the Riddle of Tension Stiffening Models for Shear Panel Experiments. Journal Of Structural Engineering, 131(9), 1422–1425.

Bentz, E. C., Massam, L., & Collins, M. P. (2010). Shear Strength of Large Concrete Members with FRP Reinforcement. Journal of Composites for Construction, 14(6), 637–646.

Bentz, E. C., Vecchio, F. J., & Collins, M. P. (2006). Simplified Modified Compression Field Theory for Calculating Shear Strength of Reinforced Concrete Elements. ACI Structural Journal, 103(4).

Bernard, S. (2013). Finite Element Modelling of Reinforced Concrete Beams with Corroded Shear Reinforcement. University of Ottawa.

Berto, L., Simioni, P., & Saetta, A. (2008). Numerical modelling of bond behaviour in RC structures affected by reinforcement corrosion. Engineering Structures, 30(5), 1375–1385.

Bielak, J. (2023). On the role of dowel action in shear transfer of CFRP textile-reinforced concrete slabs. Composite Structures, 311(116812).

Bischoff, P. H., & Paixao, R. (2004). Tension stiffening and cracking of concrete reinforced with glass fiber reinforced polymer (GFRP) bars. Canadian Journal of Civil Engineering, 31(4), 579–588.

Bonić, Z., Ćurčć, G. T., Trivunić, M., Davidović, N., & Vatin, N. (2015). Some methods of protection of concrete and reinforcment of reinforced-concrete foundations exposed to environmental impacts. Procedia Engineering, 117(1), 419–430.

Bresler, B., & Scordelis, A. C. (1963). Shear Strength of Reinforced Concrete Beams. ACI Journal, 60(1), 51–74.

Broomfield, J. P. (2007). Corrosion of steel in concrete: Understanding, investigation and repair (2nd Edition). Taylor & Francis.

Canada, I. (2008). Prestressing Concrete Structures with Fibre-Reinforced Polymers. Design Manual No. 5.

Choi, K.-K., Park, H.-G., & Wight, J. K. (2007). Unified shear strength model for reinforced concrete beams-Part I: Development. ACI Structural Journal, 105, 142–152.

Cladera, A., Marí, A., Bairán, J.-M., Oller, E., & Ribas, C. (2017). One-Way Shear Design Method Based on a Multi-Action Model A compromise between simplicity and accuracy (pp. 40–46). Concrete International.

Cladera, A., Marí, A., Ribas, C., Bairán, J., & Oller, E. (2015). Predicting the shear-flexural strength of slender reinforced concrete T and I shaped beams. Engineering Structures, 101, 386–398.

Clark, A. P. (1951). Diagonal Tension in Reinforced Concrete Beams. ACI Journal Proceedings, 48(10), 145–156.

Classen, M. (2020). Shear Crack Propagation Theory (SCPT) – The mechanical solution to the riddle of shear in RC members without shear reinforcement. Engineering Structures, 210.

Code 440.11, A. C. I. (2022). Building Code Requirements for Structural Concrete Reinforced with Glass Fiber-Reinforced Polymer (GFRP) Bars: Code and Commentary. American Concrete Institute.

Collins, M. P., Bentz, E. C., & Sherwood, E. G. (2008). Where is Shear Reinforcement Required? Review of Research Results and Design Procedures. ACI Structural Journal, 105(5), 590–600.

Collins, M. P., Bentz, E. C., Sherwood, E. G., & Xie, L. (2008). An adequate theory for the shear strength of reinforced concrete structures. Magazine of Concrete Research, 60(9), 635–650.

CSA A23.3:19, C. (2019). Design of concrete structures. Standards Council of Canada.

CSA S6:19. (2019). Canadian Highway Bridge Design Code (CHBDC).

CSA S806-12. (2012). Design And Construction of Building Structures with Fibre-Reinforced Polymers.

Darmawan, M. S. (2010). Pitting corrosion model for reinforced concrete structures in a chloride environment. Magazine of Concrete Research, 62(2), 91–101.

Dhahir, M. K. (2017). Shear strength of FRP reinforced deep beams without web reinforcement. Composite Structures, 165, 223–232.

El-Sayed, A., El-Salakawy, E., & Benmokrane, B. (2005). Shear Strength of One-Way Concrete Slabs Reinforced with Fiber-Reinforced Polymer Composite Bars. Journal of Composites for Construction, 9(2), 147–157.

El-Sayed, A., El-Salakawy, E. F., & Benmokrane, B. (2006a). Shear Capacity of High-Strength Concrete Beams Reinforced with FRP Bars. ACI Structural Journal, 103(3), 383–389.

El-Sayed, A., El-Salakawy, E. F., & Benmokrane, B. (2006b). Shear Strength of FRP-Reinforced Concrete Beams without Transverse Reinforcement. ACI Structural Journal, 103(2), 235–243.

Esfandiari, A. (1997). Shear Strength Of Structural Concrete Members Using A Uniform Shear Element Approach.

Fico, R., Galati, N., Prota, A., & Nanni, A. (2005). Design and Construction of a Bridge Deck using Mild and Post-Tensioned FRP Bars. ACI SP-230, 1121–1138.

Fisker, J., & Hagsten, L. G. (2016). Mechanical model for the shear capacity of R/C beams without stirrups: A proposal based on limit analysis. Engineering Structures, 115, 220–231.

Grandić, D., Šćulac, P., & Grandić, I. Š. (2015). Shear resistance of reinforced concrete beams in dependence on concrete strength in compressive struts. Tehnicki Vjesnik, 22(4), 925–934.

Guadagnini, M., Pilakoutas, K., & Waldron, P. (2006). Shear Resistance of FRP RC Beams: Experimental Study. Journal Of Composites For Construction, 464(473), 10–16.

Herbrand, M. (2017). Shear Strength Models for Reinforced and Prestressed Concrete Members. RWTH Aachen University.

Huber, P., Huber, T., & Kollegger, J. (2016). Investigation of the shear behavior of RC beams on the basis of measured crack kinematics. Engineering Structures, 113, 41–58.

Issa, M. A., Ovitigala, T., & Ibrahim, M. (2016). Shear Behavior of Basalt Fiber Reinforced Concrete Beams with and without Basalt FRP Stirrups. Journal of Composites for Construction, 20(4), 04015083.

Jang, H., Kim, M., Cho, J., & Kim, C. (2009). Concrete shear strength of beams reinforced with FRP bars according to flexural reinforcement ratio and shear span to depth ratio. In Oehlers, Griffith, & Seracino (Eds.), Proc., 9th Int. Symp. On Fiber Reinforced Polymer Reinforcement for Concrete Structures (FRPRCS-9).

Jin, M. H., Jan, H. S., Kim, C. H., & Baek, D. I. (2009). Concrete shear strength of lightweight concrete beam reinforced with FRP bar. In Sim (Ed.), Asia-Pacific Conf. On FRP in Structures (APFIS 2009) (pp. 203–207).

Kani, N. J. (1964). The Riddle of Shear Failure and Its Solution. Journal of the American Concrete Institute, 61(4), 441–467.

Kesler, C. E. (1954). Statistical relation between cylinder, modified cube, and beam strength of plain concrete. ASTM Proceedings, 54, 1178–1187.

Kim, C. H., & Jang, H. S. (2014). Concrete Shear Strength of Normal and Lightweight Concrete Beams Reinforced with FRP Bars. Journal of Composites for Construction, 18(2).

Kotsovos, M. D. (1983). Mechanisms of “shear” failure. Magazine of Concrete Research, 35(123), 99–106.

Kupfer, H., & Hilsdorf, H. K. (1969). Behavior of Concrete Under Biaxial Stresses. ACI Journal, 66(8), 656–666.

Marí, A., Cladera, A., Oller, E., & Bairán, J. (2014). Shear design of FRP reinforced concrete beams without transverse reinforcement. Composites Part B: Engineering, 57, 228–241.

Michaluk, C. R., Rizkalla, S. H., Tadros, G., & Benmokrane, B. (1998). Flexural Behavior of One-Way Concrete Slabs Reinforced by Fiber Reinforced Plastic Reinforcements. ACI Structural Journal, 95(3), 353–364.

Mitchell, D., & Collins, M. P. (1974). Diagonal Compression Field Theory-A Rational Model for Structural Concrete in Pure Torsion. ACI Jorunal, 71(8), 396–408.

Moody, K. G., Viest, M., Elstner, R. C., & Hognestad, E. (1954). Shear Strength of Reinforced Concrete beams, Part 1-Tests of Simple Beams. ACI Journal, 51(12), 317–332.

Moretto, O. (1945). Investigation of the Strength of Welded Stirrups in Reinforced Concrete Beams. ACI Journal Proceedings, 42(11), 141–164.

Morrow, J., & Viest, I. M. (1957). Shear Strength of Reinforced Concrete Frame Members Without Web Reinforcement. ACI Journal Proceedings, 53(3), 833–869.

Muttoni, A., & Ruiz, M. F. (2008). Shear Strength of Members without Transverse Reinforcement as Function of Critical Shear Crack Width. ACI Structural Journal, 105(2), 163–172.

Nanni, A. (1993). Flexural behavior and design of RC Members using FRP Reinforcement. J. Struct. Engrg., ASCE, 119(11), 3344–3359.

Nielsen, M. P., Braestrup, M. W., & Bach, F. (1978). Rational analysis of shear in reinforced concrete beams. International Association for Bridge and Structural Engineers, 15(78).

Noël, M. (2013). Behaviour of Post-Tensioned Slab Bridges with FRP Reinforcement under Monotonic and Fatigue Loading. University of Waterloo.

Nouri, A., Hamrat, M., Boulekbache, B., Nouri, S., Bouziadi, F., Labed, A., Haddi, A., & Djelal, C. (2021). Quantification of shear strength in reinforced concrete beams using digital image correlation: Experimental and analytical study. Advances in Structural Engineering, 24(1), 147–164.

NSERC, (2010). Bridging the Gap – Composites Extend Infrastructure Life.

Okelo, R., & Yuan, R. L. (2005). Bond Strength of Fiber Reinforced Polymer Rebars in Normal Strength Concrete. Journal of Composites for Construction, 9(3), 203–213.

Oller, E., Marí, A., Bairán, J. M., & Cladera, A. (2015). Shear design of reinforced concrete beams with FRP longitudinal and transverse reinforcement. Composites Part B: Engineering, 74, 104–122.

Placas, A., Regan, P. E., & Baker, L. L. (1971). Shear Failure of Reinforced Concrete Beams. ACI Journal Proceedings, 68(10), 763–773.

Razaqpur, A. G., Isgor, B. O., Greenaway, S., & Selley, A. (2004). Concrete Contribution to the Shear Resistance of Fiber Reinforced Polymer Reinforced Concrete Members. Journal of Composites for Construction, 8(5), 452–460.

Reineck, K. H. (1990). Mechanical model for the behaviour of reinforced concrete members in shear. University of Stuttgart.

Reineck, K.-H. (1991). Ultimate Shear Force of Structural Concrete Members without Transverse Reinforcement Derived from a Mechanical Model. ACI Structural Journal, 88(5), 592–602.

Rombach, G. A., & Kohl, M. (2016b). Fatigue strength of reinforced concrete beams without links under shear loads. ACI Structural Journal, 113(5), 941–950.

Rombach, G. A., Kohl, M., & Nghiep, V. H. (2011). Shear design of concrete members without shear reinforcement—A solved problem? Procedia Engineering, 14, 134–140.

Roshan, A. (2017). Different Approaches to Model Cover-Cracking of RC Structures due to Corrosion. University of Ottawa.

Sadeghian, V., & Vecchio, F. (2018). The Modified Compression Field Theory: Then and Now. ACI Specification Publication.

Sagaseta, J., & Vollum, R. L. (2011). Influence of beam cross-section, loading arrangement and aggregate type on shear strength. Magazine of Concrete Research, 63(2), 139–155.

Schmidt, M., Schmidt, P., Wanka, S., & Classen, M. (2021). Shear response of members without shear reinforcement- experiments and analysis using shear crack propagation theory (SCPT). Applied Sciences (Switzerland), 11(7).

Sherwood, E. G., & Bentz, E. (2008). The prediction of compressive strength of concrete block masonry View project The Shear Capacity of Short Span Beams Using Sectional Analysis View project.

Sherwood, E. G., Bentz, E. C., & Collins, M. P. (2007). Effect of Aggregate Size on Beam-Shear Strength of Thick Slabs. ACI Structural Journal, 104(2), 180–190.

Talbot, A. N. (1909). Tests of Reinforced Concrete Beams: Resistance to Web Stresses—Series of 1907 and 1908. Bulletin 29, University of Illinois Engineering Experiment Station.

Tastani, S. P., Pantazopoulou, S. J., & Karvounis, P. (2005). Local Bond-Slip Characteristics of G-FRP Bars. ACI SP-230, 1481–1496.

Taylor, H. P. J. (1974). The Fundamental Behavior of Reinforced Concrete Beams In Bending And Shear (pp. 285–303). American Concrete Institute.

Tilly, G. (2007). The Durability of Repaired Concrete Structures (pp. 1–8). International Association for Bridge and Structural Engineering.

Tottori, S., & Wakui, H. (1993). Shear Capacity of RC and PC Beams Using FRP Reinforcement (pp. 615–632).

Tran, N. L. (2020). A mechanical model for the shear capacity of slender reinforced concrete members without shear reinforcement. Engineering Structures, 219.

Tung, N. D., & Tue, N. V. (2016). A new approach to shear design of slender reinforced concrete members without transverse reinforcement. Engineering Structures, 107, 180–194.

Tureyen, A. K., & Frosch, R. J. (2002). Shear tests of FRP-reinforced beams without stirrups. ACI Structural Journal, 99(4), 427–434.

Vecchio, F. J., & Collins, M. P. (1986). The Modified Compression-Field Theory for Reinforced Concrete Elements Subjected to Shear. ACI Journal, 83, 219–231.

Vecchio, F. J., & Lorenzi, M. D. (2009). Mechanics of Reinforced Concrete Course Notes.

Walraven, J. C., & Reinhardt, H. W. (1981). Theory and Experiments on the Mechanical Behaviour of Cracks in Plain and Reinforced Concrete Subjected to Shear Loading. 26(1a).

Wang, H. (2002). Reinforced Concrete Beam Design for Shear [University of Calgary].

Wu, Y.-F., & Hu, B. (2017). Shear Strength Components in Reinforced Concrete Members. Journal of Structural Engineering, 143(9).

Xu, S., & Reinhardt, H. W. (2005). Shear Fracture on the Basis of Fracture Mechanics. In Shear fracture on the basis of fracture mechanics Otto-Graf-Journal (Vol. 16, pp. 21–78).

Yang, Y. (2014). Shear Behavior of Reinforced Concrete Members without Shear Reinforcement—A new Look at an old Problem. TU Delft.

Yoo, M. (2022). Experimental Study on the Shear Strength of Reinforced Concrete Beams with Various Integrated Shear Reinforcements. Materials, 15(9).

Yost, J. R., P, G. S., & Dinehart, D. W. (2001). Shear Strength of Normal Strength Concrete Beams Reinforced with Deformed GFRP Bars (pp. 268–275).

Zararis, P. D., & Papadakis, G. C. (2001). Diagonal Shear Failure and Size Effect In RC Beams Without Web Reinforcement. Journal Of Structural Engineering, 127(7), 733–742.

Zhou, Y., Zheng, Y., Pan, J., Sui, L., Xing, F., Sun, H., & Li, P. (2019). Experimental investigations on corrosion resistance of innovative steel-FRP composite bars using X-ray microcomputed tomography. Composites Part B: Engineering, 161, 272–284.

Zhu, W., François, R., Coronelli, D., & Cleland, D. (2013). Effect of corrosion of reinforcement on the mechanical behaviour of highly corroded RC beams. Engineering Structures, 56, 544–

Zsutty, T. C. (1968). Beam Shear Strength Prediction by Analysis of Existing Data. ACI Journal Proceedings, 65(11), 943–951.

Appendix

$$\sigma_{fpz}(w) = f_{ct} \cdot exp\,(-\frac{w}{w_1}) \quad and \quad w_1 = \frac{G_f}{f_{ct}} \qquad \textit{Eq. A. 1}$$

Where G_f is concrete fracture energy.

$$G_f = 0.028 \cdot f_{cm}^{0.18} \cdot d_{ag}^{0.32} \qquad \textit{Eq. A. 2}$$

$$F_{fpz} = b \cdot \frac{y_1}{\sin\beta_1} \cdot \int_0^1 \sigma_{fpz}\left(w_{top}(\xi)\right) \cdot d\xi = b \cdot \frac{y_1}{\sin\beta_a} \cdot \int_0^1 \sigma_{fpz}\left(w_{fpz} \cdot \xi\right) \cdot d\xi \qquad \textit{Eq. A. 3}$$

$$F_{fpz} = \; b \cdot \frac{y_1}{\sin\beta_1} \cdot f_{ct} \cdot \frac{w_1}{w_{fpz}} \cdot \left(1 - exp\left(-\frac{w_{fpz}}{w_1}\right)\right) \qquad \textit{Eq. A. 4}$$

$$V_{fpz} = \cos\beta_1 \cdot F_{fpz} \qquad \textit{Eq. A. 5}$$

$$Z_{fpz,1} = \frac{y_1}{\sin\beta_1} \cdot \left(1 - \frac{w_1}{w_{fpz}} \cdot \frac{\left(1 - \left(1 + \frac{w_{fpz}}{w_1}\right) \cdot exp\left(-\frac{w_{fpz}}{w_1}\right)\right)}{\left(1 - exp\left(-\frac{w_{fpz}}{w_1}\right)\right)}\right) \qquad \textit{Eq. A. 6}$$

$$Z_{fpz} = Z_{fpz,1} + \frac{y_2}{\sin\beta_2} \cdot \cos(\beta_2 - \beta_1) \qquad \textit{Eq. A. 7}$$

$$\tau_{ai}(w;\delta) = -\frac{f_c}{30} + [1.8 \cdot w^{-0.8} + (0.234 \cdot w^{-0.707} - 0.2) \cdot f_c] \cdot \delta \geq 0 \qquad \textit{Eq. A. 8}$$

$$\sigma_{ai}(w;\delta) = -\frac{f_c}{20} + [1.35 \cdot w^{-0.63} + (0.191 \cdot w^{-0.552} - 0.15) \cdot f_c] \cdot \delta \geq 0 \qquad \textit{Eq. A. 9}$$

$$F_{ai,\parallel} = b \cdot \frac{y_2}{\sin\beta_2} \cdot \int_0^1 \tau_{ai}(w_{bot}(\xi);\delta_{bot}(\xi))d\xi \qquad \textit{Eq. A. 10}$$

$$F_{ai,\perp} = b \cdot \frac{y_2}{\sin\beta_2} \cdot \int_0^1 \sigma_{ai}(w_{bot}(\xi);\delta_{bot}(\xi))d\xi \qquad \textit{Eq. A. 11}$$

$$Z_{ai} = \frac{b \cdot \left(\frac{y_2}{\sin\beta_2}\right)^2}{N_{ai}} \cdot \int_0^1 \sigma_{ai}(w_{bot}(\xi);\delta_{bot}(\xi)) \cdot (1-\xi)d\xi \qquad \textit{Eq. A. 12}$$

$$V_{ai} = F_{ai,\parallel} \cdot \sin\beta_2 - F_{ai,\perp} \cdot \cos\beta_2$$ *Eq. A. 13*

$$V_{da,0} = 1.64 \cdot b_n \cdot \phi_s \cdot f_c^{\,1/3}$$ *Eq. A. 14*

$$b_n = b_w - \phi_s \cdot n_s$$ *Eq. A. 15*

$$V_{da} = \begin{Bmatrix} \delta_k \le 0.05mm: & V_{da,0} \cdot \frac{\delta_k}{0.05} \cdot (2 - \frac{\delta_k}{0.05}) \\ \delta_k > 0.05mm: & V_{da,0} \cdot \frac{2.55 - \delta_k}{2.5} \ge 0 \end{Bmatrix}$$ *Eq. A. 16*

$$s_{r,delam} = y_1 \cdot \cot(\beta_1) + y_2 \cdot \cot(\beta_2) = h_3$$ *Eq. A. 17*

$$\varepsilon_{s,delam} = \frac{\sigma_s}{E_s} = \frac{F_s}{A_s \cdot E_s} \quad for \quad \sigma_s < f_y$$ *Eq. A. 18*

$$\varepsilon_{s,delam} = \frac{f_y}{E_s} = \frac{\sigma_s - f_y}{\frac{f_u - f_y}{\varepsilon_u - \varepsilon_y}} < \varepsilon_u \quad \text{for} \quad f_y \le \sigma_s < f_u$$ *Eq. A. 19*

$$\sigma_s(\varepsilon_{s,ts}) = \frac{F_s}{A_s} = \varepsilon_{s,ts} \cdot E_s + \frac{f_{ct}}{1 + \sqrt{3.6 \cdot M \cdot \varepsilon_{s,ts}}}$$

$$M = \frac{A_{c,eff}}{\sum d_s \cdot \pi}$$ *Eq. A. 20*

$$A_{c,eff} = h_{c,eff} \cdot b_w$$

$$h_{c,eff} = min\left(2.5 \cdot d_1; \frac{h - x_0}{3}\right)$$

$$\varepsilon_s = \frac{\varepsilon_{s,ts} \cdot (s_{cr} - s_{cr,delam}) + \varepsilon_{s,delam} \cdot s_{cr,delam}}{s_{cr}} \quad and \quad s_{cr,delam} \le s_{cr}$$ *Eq. A. 21*

$$\varphi = \frac{\varepsilon_s \cdot s_{cr}}{d - x_0}$$ *Eq. A. 22*